

Characteristic responses of a COTS
CCD to α , β^- , and neutron-induced
triton radiations and strategies to
reduce noise

Rosie Marie Newton

MPhys (Hons) Physics



This thesis is submitted in accordance with the requirements for the degree
of Doctor of Philosophy

December 2019

Declaration

I declare this thesis is my own work and has not been submitted for a higher degree elsewhere. The work presented here was carried out between January 2016 and October 2019.

Rosie Marie Newton

Acknowledgements

There are many people who have supported me throughout my PhD. First and foremost, my supervisor Prof. Malcolm Joyce, whose excellent guidance and knowledge has made this research possible. Thanks also go to Mike Scott of BIC Technology Ltd. for his support throughout. I would like to acknowledge the funding from the Engineering and Physical Sciences Research Council and the Lloyds Register Foundation, and all of the additional resources made available through the Next Generation Nuclear Centre for Doctoral Training.

Thanks go to the rest of my research group, and everyone who came to lunches, for discussions on many varied and interesting subjects. Some of these resulted in useful suggestions and insights, whilst others provided a fun diversion.

My Mum and my sister have always been and continue to be encouraging and supportive with everything I do, and have largely contributed to me reaching this point, for which I will always be grateful. And thanks to Simon for his love and understanding, and making me many cups of tea. You have made this process easier in so many ways.

And finally, thanks to Tiki and Elodin, for always making me smile.

Abstract

The potential of commercially available CCDs to perform *in-situ* detection and spectroscopy of α radiation has been investigated. The CCDs used are Sony ICX825AL as part of an Ultrastar camera from Starlight Xpress, modified by BIC Technology Ltd.. The glass covering is removed and the CCD is covered with a thin, aluminised Mylar film to prevent light interacting with the device. Vertical streaks seen in images produced when exposed to a ^{210}Po source provide a unique identifier for the presence of α radiation. The sizes of the clusters produced and intensities of the brightest pixel in each cluster have been used among other properties to distinguish between α and β^- radiation, and noise caused by radiation damage in the CCD. It was found that the CCDs used are mostly insensitive to γ radiation. It is possible to detect neutrons using this device by covering the CCD with ^6Li -enriched crystals and detecting the α particles and tritons produced by the interactions of neutrons with the ^6Li . The properties of clusters produced by this method were also analysed and compared with the previous types of radiation. Distinguishing features were found for each type of radiation analysed. Simulations suggest that the cluster sizes will vary depending on the energy of the incoming radiation, but it was found that the cluster sizes from the two β^- sources used could not be significantly separated, due to the small energy difference between

them of 197 keV. Discrimination should still be possible for β^- particles with a larger energy difference. Cluster sizes and streak lengths for α radiation should also vary depending on the energy of the incident α radiation. Annealing, cooling, and image processing techniques have been determined to mitigate the effects of radiation damage in these devices.

Table of contents

DECLARATION.....	II
ACKNOWLEDGEMENTS.....	III
ABSTRACT	IV
TABLE OF CONTENTS.....	VI
LIST OF TABLES	IX
LIST OF FIGURES	XI
GLOSSARY.....	XXI
List of acronyms.....	xxi
List of symbols.....	xxii
1 INTRODUCTION.....	1
1.1 The challenge of <i>in-situ</i> α -radiation detection	1
1.2 Research objectives	2
1.3 Novelties of this research	3
1.4 References	5
2 BACKGROUND	7
2.1 Radiation properties and assay	8
2.1.1 <i>Alpha radiation</i>	8

2.1.2 Beta radiation	8
2.1.3 Gamma radiation.....	9
2.1.4 Neutron radiation	10
2.1.5 Radiation detection.....	10
2.2 Charge-coupled devices	17
2.2.1 CCD history.....	17
2.2.2 CCD operation	18
2.2.3 Radiation detection with CCDs	25
2.2.4 Radiation damage in CCDs	29
2.2.5 Comparison with CMOS.....	31
2.3 References	32
3 METHODS	42
3.1 Equipment	43
3.1.1 Radioactive sources	43
3.1.2 Detector information	47
3.1.3 CCD software	52
3.1.4 Post-processing software.....	54
3.2 Modelling methods.....	55
3.2.1 CCD structure.....	55
3.2.2 SRIM: α radiation.....	57
3.2.3 CASINO: β^- radiation	58
3.3 Experimental methods.....	59
3.3.1 Standard experimental setup	60
3.3.2 Post-processing techniques	61
3.3.3 Experiments with β^- radiation.....	63
3.3.4 Experiments with α radiation	65
3.3.5 Experiments with neutron radiation	66
3.3.6 Noise investigation.....	68
3.4 References	73
4 RESULTS	78
4.1 CCDs for radiation detection	79
4.1.1 SRIM simulations.....	79
4.1.2 CASINO simulations.....	83
4.1.3 Initial images	86
4.2 Detecting β^- radiation	89
4.2.1 Cluster sizes for different energy β^- particles.....	89
4.2.2 Blocking β^- radiation	91
4.3 Detecting α radiation	95
4.3.1 Cluster sizes.....	95
4.3.2 Streak lengths.....	97
4.3.3 Pixel intensities.....	98
4.4 Detecting neutron radiation.....	100
4.5 Noise investigations	105
4.5.1 Identifying radiation damage	108
4.5.2 Damage repair and mitigation	113
4.6 References	119
5 DISCUSSION	120

5.1 The potential of CCDs for radiation detection and spectroscopy	121
5.1.1 <i>SRIM simulations</i>	121
5.1.2 <i>CASINO simulations</i>	123
5.1.3 <i>Experimental comparison with models</i>	126
5.2 Identification of radiation type.....	131
5.2.1 <i>Proof of the correlation between cluster shape and radiation type</i>	131
5.2.2 <i>Comparison of different radiation types</i>	134
5.3 Noise and radiation damage	143
5.3.1 <i>Noise increase</i>	143
5.3.2 <i>Radiation damage</i>	143
5.3.3 <i>Mitigation of radiation damage effects</i>	145
5.4 Comparison with existing technologies	149
5.5 References	151
6 CONCLUSION.....	154
6.1 CCDs for α radiation detection and spectroscopy.....	154
6.2 CCDs for detecting β^- and neutron radiation	155
6.3 Recommendations for future work.....	156
6.4 Final conclusion	156
APPENDIX A	158
A.1 Fill gaps in streaks.....	158
A.2 Remove noise	159
A.3 Highlight images	161
A.4 Cluster analysis	162
A.5 Streak analysis.....	163
A.6 Intensity analysis.....	164

List of Tables

Table 3.1 Estimated and measured layers of the total source-to-CCD distance for the ^{210}Po source. The two values for each layer in the gate structure represent the thick (left) and thin (right) structures used.....	57
Table 3.2 Linear mass attenuation coefficients for the γ rays produced by the two sources used, using data from [24], and the distance into aluminium at which they will be at 90% of their original intensities.	65
Table 3.3 The oven temperatures and respective lengths of time tested for annealing. .	70
Table 4.1 Average energy remaining to be detected in the active region and range of the α particles into the active region for different α -particle energies, using conservative gate thickness estimates.	83
Table 4.2 Parameters for the lognormal fits in Figure 4.5, of simulated cluster sizes for 317 keV and 514 keV electrons.	86
Table 4.3 Parameters for the lognormal fits in Figure 4.9, of the cluster sizes produced by exposures to ^{60}Co and ^{137}Cs	91

Table 4.4 Parameters for the Gaussian fit in Figure 4.14, for cluster sizes from α particles produced by ^{210}Po .	97
Table 4.5 Average energy loss prior to the active region and total range of 2.05 MeV α particles and 2.75 MeV T^+ particles produced from neutron interactions with ^6Li in contact with the Mylar film.	102
Table 4.6 Parameters for the Gaussian fit in Figure 4.20, of the cluster sizes from particles produced in neutron interactions with ^6Li .	104
Table 4.7 Power-law fit parameters for the cluster sizes produced by noise within the CCD, in Figure 4.23.	107
Table 5.1 Peak centres and standard deviations for clusters produced by radiation from the four different sources considered.	139
Table 5.2 Properties to identify different types of radiation and noise within the CCD. The CCD is not sensitive to γ radiation and so this cannot be identified.	142

List of Figures

Figure 2.1 Generalised example of the energy spectrum for β particles produced by an isotope susceptible to β decay. The maximum energy in the spectrum is denoted by E_{\max}	9
Figure 2.2 A schematic illustration of the interaction properties of three different types of radiation and the materials that will stop them.....	11
Figure 2.3 Charge carrier production, collection, and transfer in a CCD pixel. The black and white circles represent negative and positive charge carriers, respectively.....	19
Figure 2.4 Top: Three-phase CCD gate structure. Below: Potentials across the gates at four different times, T_{1-4} , showing how the charge is transferred.....	20
Figure 2.5 Diagrams showing the effect of the surface channel (left) vs the buried channel (right) on the location of charge carriers (black dots) within the CCD.....	22
Figure 2.6 Front- and back-illuminated CCD structures.....	22
Figure 2.7 Comparison of interline (left) and frame (right) transfer structures, showing the movement of the charge carriers into and along the output register.....	23
Characteristic responses of a COTS CCD to α , β -, and neutron-induced triton radiations and strategies to reduce noise	

Figure 2.8 Three examples of blooming occurring in images taken of stars with a CCD. Image from [36].	24
Figure 2.9 Example tracks formed by interactions of different radiation types from an exposure of the DECam CCD to cosmic rays. Image taken from [42]......	26
Figure 2.10 The response of heavy ions with decreasing LET, demonstrating the reduction in the length of the streaks. Image taken from [51].	28
Figure 2.11 Examples of an α -particle cluster (left) and streak (right) from interactions within a DAMIC CCD. Images taken from [41].	29
Figure 3.1 Decay scheme showing the decay of ^{210}Po to ^{206}Pb through α emission. The data are from [2]......	44
Figure 3.2 Diagram showing the dimensions of the ^{210}Po α -particle source.	44
Figure 3.3 Decay scheme showing the decay of ^{60}Co to ^{60}Ni through β^- and γ emission. The data are from [3].	46
Figure 3.4 Decay scheme showing the decay of ^{137}Cs to ^{137}Ba through β^- and γ emission. The data are from [3].	46
Figure 3.5 Left: CCD imaging area, with the CCD attached to the backing board. Right: The radiation detection device, with the board attached to the PCB and the imaging area covered with the Mylar film.	48
Figure 3.6 Simplified diagram showing the CCD connections through the backing board.....	48
Figure 3.7 Original device configuration with long wires connecting the CCD to the electronics.	50
Characteristic responses of a COTS CCD to α , β^- , and neutron-induced triton radiations and strategies to reduce noise	

- Figure 3.8 Temporary device configuration intended to reduce noise, with a plastic box coated in a copper film, and the long wires replaced with shorter, sturdier wires.. 50
- Figure 3.9 Final device configuration used in this research..... 51
- Figure 3.10 Diagram detailing the operation of a heat pipe, with the heat source indicated by the red colouring on the left, where evaporation occurs, and the cooler side indicated by the blue colouring, where the condensation occurs. 51
- Figure 3.11 Left: The fan and the heat pipe developed in and used in this research. Right: The fan and the heat pipe in the primary positions used on the device. 52
- Figure 3.12 Graphical user interface (GUI) for the QubiX Radiation Detector software used with the CCD in this work. 53
- Figure 3.13 Example of a 30-s background measurement taken with one of the CCDs in this work. The pixels have been highlighted to have the maximum intensity of 255 ADU (Analogue-to-Digital Units). 54
- Figure 3.14 The regions used in the CASINO simulation to represent 100 CCD pixels (multi-coloured) and a section of the substrate beneath (blue). Both materials are silicon. 59
- Figure 3.15 The most-commonly used experimental setup, showing the CCD in use with the ^{210}Po source. 60
- Figure 3.16 Typical examples of a streak and a cluster caused by α radiation, and a track caused by β radiation. Each has been surrounded with a bounding box (in green) used to obtain information about the shapes of these signals. The pixels have been highlighted to the maximum intensity. 62

- Figure 3.17 Image section showing a split α -induced streak before and after processing. The software threshold is marked in red on the scale. 63
- Figure 3.18 Experimental setup in the neutron lab., with the CCD held in place facing the neutron tank. 68
- Figure 3.19 Different setups used for cooling. Top left: no cooling. Top right: the heat pipe alone. Bottom left: the heat pipe being cooled by the fan. Bottom right: the fan directly cooling the CCD without the heat pipe. 72
- Figure 4.1 SRIM simulation results for the interactions of 10,000 α particles with an incident energy of 5.304 MeV through the total source-to-CCD distance. Left: α -particle tracks showing their range and spread. Right: Energy loss to ionisation as a function of depth. 80
- Figure 4.2 SRIM simulation sections focusing on the CCD layers. Left: Tracks showing the range of the α particles within the CCD. Only 200 tracks are shown for clarity. Right: Energy loss to ionisation for all 10,000 α particles simulated as a function of depth. 81
- Figure 4.3 SRIM simulation showing the collisions of 10,000 α particles with an incident energy of 5.304 MeV through the total source-to-CCD distance. The displacements per ion, replacement collisions, and resultant number of vacancies are shown. The detail of what is happening in the CCD can be seen in Figure 4.2. 82
- Figure 4.4 CASINO simulations showing 30 of the 10,000 tracks for β particles with an energy of (a) 317 keV and (b) 514 keV to represent ^{60}Co and ^{137}Cs , respectively. 10×10 binned pixels are simulated. These are 60 μm deep on top of a 60 μm

substrate layer. All regions are silicon. Different colours represent different regions each electron has passed through.	84
Figure 4.5 CASINO simulation data showing the cluster sizes for 10,000 electrons at two energies, 317 keV and 514 keV, passing through the active layer and substrate of the CCD.	85
Figure 4.6 Typical example of a 6-minute exposure to a ^{210}Po α -particle source with an activity of 43 Bq. Clusters are highlighted to have the maximum intensity of 255 ADU.	87
Figure 4.7 Typical example of a 1-s exposure to a ^{137}Cs β/γ source with an activity of 330 kBq. Clusters are highlighted to have the maximum intensity of 255 ADU. ..	88
Figure 4.8 Typical example of a 5-s exposure to a ^{60}Co β/γ source with an activity of 8.84 kBq. Clusters are highlighted to have the maximum intensity of 255 ADU. .	89
Figure 4.9 Cluster sizes for clusters produced by ^{60}Co and ^{137}Cs interactions in the CCD. The number of clusters has been normalised; the original number of counts used are 1043 for ^{60}Co and 1168 for ^{137}Cs	90
Figure 4.10 The average number of clusters produced in 55-s exposures to ^{60}Co and 10-s exposures to ^{137}Cs , both with and without a 4 mm aluminium covering. Each average is over 10 images.	92
Figure 4.11 Example 10-s exposures to a ^{137}Cs source of activity 312 keV uncovered (top) and covered with a 4 mm piece of aluminium (bottom). Clusters are highlighted to have the maximum intensity (255 ADU).	93
Figure 4.12 Example 130×100 pixel sections of the exposures in Figure 4.11, demonstrating the original intensities of the clusters.	94
Characteristic responses of a COTS CCD to α , β -, and neutron-induced triton radiations and strategies to reduce noise	

- Figure 4.13 The intensities of the brightest pixels in clusters produced in exposures to ^{60}Co (left) and ^{137}Cs (right), both uncovered (top) and with a 4mm aluminium covering to block the β radiation (bottom). Each graph uses data from 10 exposures. The CCD software removes pixels below a threshold intensity of 54 ADU.....95
- Figure 4.14 Cluster sizes for α particles produced by ^{210}Po . Clusters of 1 pixel were not included, with a value of 54,700.96
- Figure 4.15 Streak lengths for the ^{210}Po source. Cluster heights of 1-3 are excluded from the graph as these do not constitute streaks, to allow the relevant streak data to be seen more clearly.98
- Figure 4.16 Example 110×78 pixel section of a typical exposure to the ^{210}Po source. The clusters have their original intensities.....99
- Figure 4.17 The intensities of the brightest pixels in clusters identified as being created from α particle interactions in the CCD. The software threshold automatically removed any pixels below 50 ADU..... 100
- Figure 4.18 Full 10-minute exposure to the ^{252}Cf neutron source with an activity of 17.5 MBq, with a covering of ^6Li -enriched crystals over the CCD. The clusters have been highlighted to the maximum intensity (255 ADU)..... 101
- Figure 4.19 SRIM simulations showing the ionisation of 2.05 MeV α particles (left) and 2.75 MeV T^+ particles (right) in the CCD, with the particles produced in contact with the Mylar film. 102
- Figure 4.20 Cluster sizes for particles produced by experimental neutron interactions with ^6Li . 157 clusters were analysed over 4 images. 103

- Figure 4.21 The intensity of the brightest pixel in each cluster from particles produced by the interaction of the neutron source with ${}^6\text{Li}$. The software threshold automatically removed any pixels below 50 ADU. 105
- Figure 4.22 Example exposure with no source present, taken over 60-s with the CCD. Pixels have been highlighted to their maximum intensity (255 ADU). 106
- Figure 4.23 Sizes of clusters produced by noise within the CCD during exposures with no source present. 143,622 clusters were analysed over 97 images. 107
- Figure 4.24 The intensities of the brightest pixels in clusters produced by noise in the CCD. The software threshold automatically removed any pixels below 50 ADU. 108
- Figure 4.25 The number of bright pixels in a 30-s background measurement for equivalent sized sections on the covered and uncovered side of the CCD after each additional exposure to a ${}^{210}\text{Po}$ source. 109
- Figure 4.26 Example images of the 30-s background before irradiation (top) and after 5 hours exposure to the ${}^{210}\text{Po}$ source (bottom), with the right half of the CCD covered in card. 110
- Figure 4.27 The number of bright pixels in a 30-s background measurement for the whole CCD imaging area over exposures to the ${}^{137}\text{Cs}$ source. 111
- Figure 4.28 Example images of the 30-s background before irradiation (top) and after 19 hours exposure to the ${}^{137}\text{Cs}$ source (bottom). 112
- Figure 4.29 Examples of 5-minute exposures with no source present before (top) and after (bottom) a 24 hour anneal at 100°C . Pixels are highlighted to have the maximum intensity (255 ADU). 114
- Characteristic responses of a COTS CCD to α , β -, and neutron-induced triton radiations and strategies to reduce noise

- Figure 4.30 Average number of bright pixels (noise) in images produced by the CCD in 5-minute exposures with no source present at four levels of cooling: No cooling, just the heat pipe, both the heat pipe and the fan, and just the fan..... 115
- Figure 4.31 Example 348×260 pixel sections of 3-minute exposures with no source present for with different methods of cooling..... 116
- Figure 4.32 Example 110×80 pixel sections of exposures to (a) no source, showing just noise, and (b) the ^{210}Po source with both clusters and streaks from α particles. These images show the relative intensities of the pixels on a scale from 0 (black) to 255 (white). The software threshold is marked in red on the scale..... 117
- Figure 4.33 Example images of a 15-minute exposure to the ^{210}Po source with an activity of 19 Bq before and after image processing to remove the noise. The clusters have been highlighted to have the maximum intensity of 255 ADU for clarity. 118
- Figure 5.1 CASINO simulation data showing the cluster sizes for 10,000 electrons at two energies, 317 keV and 514 keV, passing through the active layer and substrate of the CCD. Reproduced from Figure 4.5..... 125
- Figure 5.2 Highlighted 165×142 pixel section of a 2.5-hour exposure to the ^{210}Po source with an activity of 11 Bq, demonstrating overlapping clusters. 127
- Figure 5.3 Cluster sizes for α particles produced by ^{210}Po . Clusters of 1 pixel were not included, with a value of 54,700. Reproduced from Figure 4.14. 128
- Figure 5.4 A comparison of the cluster sizes produced by experimental data for ^{60}Co and ^{137}Cs , and CASINO simulations of energies representing the β^- particles produced by these sources..... 130

- Figure 5.5 A highlighted 246×165 pixel section of a typical 60-s exposure to the ^{210}Po source. 135
- Figure 5.6 Highlighted 146×114 pixel sections of typical exposures to the ^{60}Co (left, 5-s exposure) and ^{137}Cs (right, 1-s exposure) sources. 136
- Figure 5.7 A comparison of the cluster sizes produced for each of the radiation types studied in this research and for noise when no radiation is present. The ^{210}Po data continued the trend up to a cluster size of 55 pixels, but have not been included so the peaks can be seen more clearly. Where error bars cannot be seen they are smaller than the symbols used for the data points. 138
- Figure 5.8 Cluster sizes up to size 25 for exposures to the ^{210}Po source. A power law fit has been applied to the first three data points, and a Gaussian fit to the remaining data points. 139
- Figure 5.9 A comparison of the intensities of the brightest pixel in each cluster produced by noise and by particles produced in the interactions of neutrons from ^{252}Cf with ^6Li . The total number of clusters has been normalised for each source. 140
- Figure 5.10 A comparison of the intensities of the brightest pixel in each cluster for ^{137}Cs and noise. The noise data have been normalised to the height of the first peak in the ^{137}Cs data. 141
- Figure 5.11 The number of bright pixels in a 30-s background measurement for equivalent sized sections on the covered and uncovered side of the CCD after each additional exposure to a ^{210}Po source. Reproduced from Figure 4.25 for clarity. 144
- Figure 5.12 Average number of bright pixels (noise) in images produced by the CCD in 5-minute exposures with no source present at four levels of cooling, from warmest

to coolest: No cooling, just the heat pipe, both the heat pipe and the fan, and just the fan. Reproduced from Figure 4.30.	147
Figure 5.13 Representative 250×150 section of a highlighted CCD image produced under a 30-s exposure to a ^{210}Po source (a) before and (b) after post-processing to remove noise.	148

Glossary

List of acronyms

ADU	Analog to digital units
ALARP	As low as reasonably practicable
CASINO	Monte Carlo simulation of electron trajectory in solids
CCD	Charge-coupled device
CMOS	Complementary metal-oxide-semiconductor
COTS	Commercial-off-the-shelf
CTE	Charge transfer efficiency
FWHM	Full width at half maximum
GUI	Graphical user interface
LET	Linear energy transfer
PCB	Printed circuit board
SRIM	Stopping and range of ions in matter
TLD	Thermoluminescent dosimeter
USB	Universal serial bus

List of symbols

*	An excited state of an isotope
A	Isotope mass number
a, b	Power law fit coefficients
A'	Area
A₀	Original activity
A_t	Activity at a time, <i>t</i> , after the original activity
dE/dx	Stopping power
E	Energy of a particle
E_{max}	Maximum energy in an energy spectrum
GND	Ground
H₁₋₂	CCD horizontal clocks
I	Mean energy required for ionisation in a material
I₀	Incident radiation intensity
I_x	Radiation intensity at a distance <i>x</i> into a material
m	Electron mass
n	Neutron
N	Atomic density of a material
N_A	Avogadro's constant, $6.022140857 \times 10^{23} \text{ mol}^{-1}$
O/P	CCD output
R	Range of a particle into a material
r	Distance from radioactive source
R_G	CCD reset gate clock
SUB	CCD substrate clock
T	Kinetic energy
t	Time
T⁺	Triton, a ³ H nucleus

$T_{1/2}$	Half-life
v	Particle velocity
V_{1-4}	CCD vertical clocks
V_{dd}	CCD supply voltage
w	Width of a peak at one standard deviation
X	Generic parent nucleus in a reaction
x	Distance into a material
xc	Peak centre
Y	Generic daughter nucleus in a reaction
y_0	Offset of a distribution
Z	Isotope atomic number
Ze	Particle electric charge
α	α particle, a ${}^4\text{He}$ nucleus
$\beta^{+/-}$	β particle, an electron (-) or positron (+)
γ	γ ray photon
λ	Radioactive decay constant
μ	Mean value of the data
μ_L	Linear attenuation coefficient
$\bar{\nu}$	Antineutrino
ρ	Material density
σ	Standard deviation
σ_i	Interaction cross section per atom
σ_l	Log standard deviation

1 Introduction

1 INTRODUCTION.....	1
1.1 The challenge of <i>in-situ</i> α -radiation detection	1
1.2 Research objectives	2
1.3 Novelties of this research	3
1.4 References	5

1.1 The challenge of *in-situ* α -radiation detection

The detection and identification of radioactive contamination is essential in the nuclear industry but can be difficult to achieve *in-situ* for α radiation, owing to its short range in air. Because α -emitting radioactivity is particularly hazardous if inhaled or ingested, identifying α contamination is critical to managing this risk. Usually, α -particle spectroscopy is performed in a laboratory environment. The sample is first processed to isolate the radioisotope, and typically a semiconductor detector is used in a vacuum to ensure no loss of energy from interaction in the air in between the sample and the detector. There are various types of portable detectors which can identify the presence of α radiation, but these often cannot discriminate between different radiation types. Other detectors can provide good discrimination and provide energy spectra but are less

portable, and cannot easily be used as a hand-held monitor. However, there are many applications for a potential *in-situ* α radiation detector.

There are many areas where α -contamination may arise. Isotopes emitting α -radiation are used in medical physics, for example in targeted alpha therapy for cancer treatment [1], [2]. The nuclear power industry uses uranium in its fuel, which produces α radiation. The fission process itself also generates long-lived α -emitting isotopes. This means α -contamination may occur at any stage in the nuclear fuel cycle. There are also legacy sites left over from the radium and plutonium industries from the last century which may still contain contamination that needs identifying [3]. This shows a multitude of situations where quick and accurate identification of α radiation *in-situ* may be important. These α -emitting isotopes will often also emit or occur alongside other isotopes emitting β^- or γ radiation. Due to the different shielding requirements and health hazards, it is important to be able to identify if α radiation is present in these mixed environments which can often mask the presence of α radiation. This is particularly significant in environments where the contaminated material is at risk of being dispersed in the air through the action of people or machines, due to the hazards associated with inhalation and ingestion of α radiation.

1.2 Research objectives

The primary aim of the research described in this thesis was to investigate the potential to use commercially-available charge-coupled devices (CCDs) to perform *in-situ* detection and spectroscopy of α radiation. The device should be able to discriminate between different types of radiation and provide useful information about the sources present, with which to benefit action plans to deal with such material. Throughout the research, additional aims were determined, including investigating the potential of using

the α -particle detection abilities to identify neutron radiation, and to mitigate damage caused by the radiation in the CCDs in order to optimise their potential use.

The research objectives were therefore to assess the ability of commercially-available CCDs to perform the following tasks whilst maintaining their small, hand-held size:

- identify the presence of α radiation;
- perform discrimination between different radiation types;
- determine the energy of the radiation;
- identify neutron radiation;
- and mitigate the effects of radiation damage.

1.3 Novelities of this research

Several authors have noted that different radiation types produce clusters of different shapes when interacting in CCDs and have discussed the mechanisms behind this [4]–[7]. Vertical streaks, or blooming, have been observed in CCDs exposed to α radiation and charged particles [8], [9], but the extent of this to be characteristic of a particular radiation was poorly understood and blooming had not previously been observed with a ^{210}Po source, as has been explored comprehensively in this research.

Aguilar-Arevalo, *et al.*, have provided methods of distinguishing between the clusters from α and β^- radiation by comparing their symmetry [5]. Smith, *et al.*, have investigated discriminating signals from muons from those produced by β^- radiation by their linearity [6]. Saad Saoud, *et al.*, have compared the sizes of clusters produced from uranium and thorium sources [7]. These analyses on the shapes of the clusters produced have been taken further in this research by analysing the shapes of the clusters produced by α particles, tritons and β^- particles from four different sources, and by comparing their sizes, with different distributions identified for each of the different types of

radiation studied. This cluster size comparison has also been applied to the noise produced by radiation damage within the CCD during operation. Analysis of the intensities of the pixel clusters produced has also been performed as an additional property with the potential to discriminate between different radiation types and noise.

There has been some exploration using CCDs to detect neutron radiation, however these typically include the use of a scintillator, with the CCD detecting the light produced [10], [11]. This thesis considers, instead, the potential of detecting the α particles and tritons produced by the neutrons interacting with ${}^6\text{Li}$, using the properties described previously. This utilises the lack of sensitivity of the CCD to γ radiation to ensure that only signals produced from the neutron interactions are detected and is particularly suited to thermal neutrons given the prominent cross-section dependence of ${}^6\text{Li}$ in this energy region.

Therefore, the key novel achievements of this research are:

- Blooming produced by ${}^{210}\text{Po}$ -derived α -particle interactions in CCDs has been investigated comprehensively;
- A comparison of the cluster sizes produced by different types of radiation, including α , β^- and neutron radiation has been made;
- Each of the contrasting trends in cluster-size distributions produced by different types of radiation and by noise produced by radiation damage has been identified;
- A comparison of the intensities of the brightest pixels in clusters produced by the previous four sources and for noise has been made;
- The feasibility of commercial-off-the-shelf CCDs to be used to detect the α particles and tritons produced by interactions of neutrons with a lithium converter layer has been demonstrated.

1.4 References

- [1] A. Morgenstern, C. Apostolidis, C. Kratochwil, M. Sathekge, L. Krolicki, and F. Bruchertseifer, “ An Overview of Targeted Alpha Therapy with ^{225}Ac and ^{213}Bi ,” *Curr. Radiopharm.*, vol. 11, no. 3, pp. 200–208, 2018.
- [2] “Radioisotopes in Medicine,” *World Nuclear Association*. [Online]. Available: <https://www.world-nuclear.org/information-library/non-power-nuclear-applications/radioisotopes-research/radioisotopes-in-medicine.aspx>. [Accessed: 28-Nov-2019].
- [3] A. Varley, A. Tyler, L. Smith, P. Dale, and M. Davies, “Remediating radium contaminated legacy sites: Advances made through machine learning in routine monitoring of ‘hot’ particles,” *Sci. Total Environ.*, vol. 521–522, pp. 270–279, 2015.
- [4] J. Estrada, J. Molina, J. J. Blostein, and G. Fernández, “Plasma effect in silicon charge coupled devices (CCDs),” *Nucl. Instruments Methods Phys. Res. Sect. A Accel. Spectrometers, Detect. Assoc. Equip.*, vol. 665, pp. 90–93, 2011.
- [5] A. Aguilar-Arevalo *et al.*, “Measurement of radioactive contamination in the CCD’s of the DAMIC experiment,” *J. Phys. Conf. Ser.*, vol. 718, p. 042057, May 2016.
- [6] A. R. Smith *et al.*, “Radiation events in astronomical {CCD} images,” *Proc. SPIE*, vol. 4669, pp. 172–183, Apr. 2002.
- [7] T. Saad Saoud *et al.*, “Use of CCD to Detect Terrestrial Cosmic Rays at Ground Level: Altitude vs. Underground Experiments, Modeling and Numerical Monte Carlo Simulation,” *IEEE Trans. Nucl. Sci.*, vol. 61, no. 6, pp. 3380–3388, Dec.

2014.

- [8] T. S. Lomheim *et al.*, “Imaging charge-coupled device (ccd) transient response,” pp. 1876–1885, 1990.
- [9] A. Aguilar-Arevalo *et al.*, “Measurement of radioactive contamination in the high-resistivity silicon CCDs of the DAMIC experiment,” *J. Instrum.*, vol. 10, no. 08, pp. P08014–P08014, Aug. 2015.
- [10] J. J. Blostein, J. Estrada, A. Tartaglione, M. S. Haro, G. F. Moroni, and G. Cancelo, “Development of a novel neutron detection technique by using a boron layer coating a Charge Coupled Device,” *J. Instrum.*, vol. 10, no. 01, pp. P01006–P01006, Jan. 2015.
- [11] O. Bourrion *et al.*, “C2D8: An eight channel CCD readout electronics dedicated to low energy neutron detection,” *Nucl. Instruments Methods Phys. Res. Sect. A Accel. Spectrometers, Detect. Assoc. Equip.*, vol. 880, pp. 28–34, Feb. 2018.

2 Background

2 BACKGROUND	7
2.1 Radiation properties and assay	8
2.1.1 <i>Alpha radiation</i>	8
2.1.2 <i>Beta radiation</i>	8
2.1.3 <i>Gamma radiation</i>	9
2.1.4 <i>Neutron radiation</i>	10
2.1.5 <i>Radiation detection</i>	10
2.2 Charge-coupled devices	17
2.2.1 <i>CCD history</i>	17
2.2.2 <i>CCD operation</i>	18
2.2.3 <i>Radiation detection with CCDs</i>	25
2.2.4 <i>Radiation damage in CCDs</i>	29
2.2.5 <i>Comparison with CMOS</i>	31
2.3 References	32

This chapter describes the background information and theory relevant to the research described in this thesis. It consists of two main sections. The first describes different types of ionising radiation, the way they interact with matter and how they have been detected generically. The second part describes the history and operation of CCDs, and how they are currently used with radiation.

2.1 Radiation properties and assay

Radioactive decay is a process that occurs in unstable isotopes to achieve a greater stability. The decay involves the emission of ionising radiation, such as: α particles, β particles, γ rays and neutrons. The first section of this chapter will introduce the ionising radiations considered in this research. Their interactions with matter, properties relevant to this research and current methods of detection will then be described.

2.1.1 Alpha radiation

Some unstable nuclei may decay by emitting an α particle, reducing the mass of the nucleus by 4, thereby increasing the stability; this is a mode of decay typical for heavier isotopes. The α -particle is a helium nucleus, and its emission is energetically favoured as it is a particularly stable structure. This decay is described by the general equation:



where X represents the parent nucleus, A is its mass number, Z is its atomic number, and Y is the daughter nucleus. Alpha particles are produced with an energy related to the difference in binding energies of the parent nucleus and the combined daughter products and the mass defects of the daughter products [1].

2.1.2 Beta radiation

Alternatively, an unstable nucleus can decay through emission of a β particle, to effect a more equitable balance between the number of neutrons and protons in nuclei that comprise either too many neutrons or protons. In the case of there being too many neutrons, a negatively-charged electron, or β^- particle, will be emitted. For too many protons a positron, or β^+ particle, will be emitted. The equation generally describing β^- decay is given by:



The emission of a β^- particle is accompanied by the emission of an antineutrino, $\bar{\nu}$. Similarly, a β^+ particle is emitted with a neutrino, ν . For this reaction the product Y has an atomic number of $Z - 1$. The energy produced in the reaction is spread between the β -particle and neutrino, characterised by a continuous energy spectrum, such as in the generalised example shown in Figure 2.1 [2].

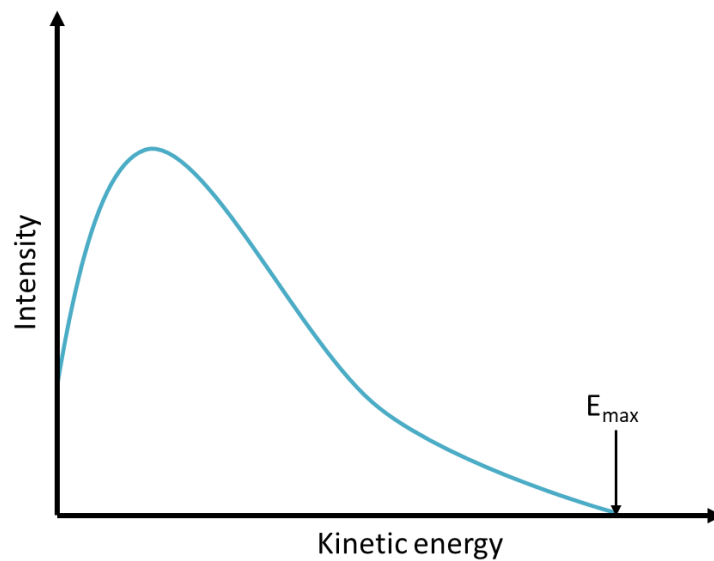


Figure 2.1 Generalised example of the energy spectrum for β particles produced by an isotope susceptible to β decay. The maximum energy in the spectrum is denoted by E_{\max} .

2.1.3 Gamma radiation

Gamma radiation often occurs alongside other radioactive emissions, which commonly leave the resultant nuclei in an excited state. The excited nucleus will then emit a γ -ray to de-excite. The equation describing γ -ray emission is:



where the * represents an excited state. Due to the energy transitions of the excited states, γ radiation will be emitted at discrete energies depending on the excited state of parent nucleus [1].

2.1.4 Neutron radiation

The most common sources of neutron radiation are those based on fission processes (either spontaneous fission such as ^{252}Cf or induced fission via a nuclear reactor) or as a result of a nuclear reaction, such as (α, n) or (γ, n) reactions. One source which is commonly used to produce neutrons by the latter method is an americium-beryllium source, which produces neutrons through the interaction of the α particles emitted by the americium source with beryllium, in the following reaction:



The general equation for neutron emission from a parent nucleus is:



where, for the example given in Equation (2.4), ${}^A\text{X}$ would be the unstable ${}^{13}\text{C}$ formed by the interaction of ${}^9\text{Be}$ with the α -particle. The energy spectrum of the emitted neutrons depends on the specific source combination used [1].

2.1.5 Radiation detection

Radiation detection utilises the various interactions of radiation with matter. As α and β radiations are directly ionising, creating electron-hole pairs in the materials they pass through, they can be detected through these ionisations. Neutrons and γ rays are indirectly ionising, so must be detected through secondary interactions. There are three different interaction processes associated with the interaction of γ rays in materials: the photoelectric effect, the Compton effect, and pair production. The dominant interaction

is dependent on the energy of the incident γ ray, but all cause ionisation which can be detected. Finally, neutrons can be absorbed by atoms to put them in an unstable state, so they will emit a subsequent type of ionising radiation which can be detected. They may also be detected through elastic scattering interactions [1]–[3].

2.1.5.1 Interactions of radiation with matter

Different types of ionising radiation have different interaction properties. The most strongly ionising in the context of this research is α radiation, which can be stopped by a piece of paper or the dead layer of skin (epidermis). A relatively thin layer of aluminium is required to stop β radiation, which is slightly less interacting. The most-weakly ionising of these radiations, and hence the radiation with the furthest range, is γ radiation. This requires a thick layer of lead to be stopped completely [1]. These interactions are illustrated schematically in Figure 2.2.

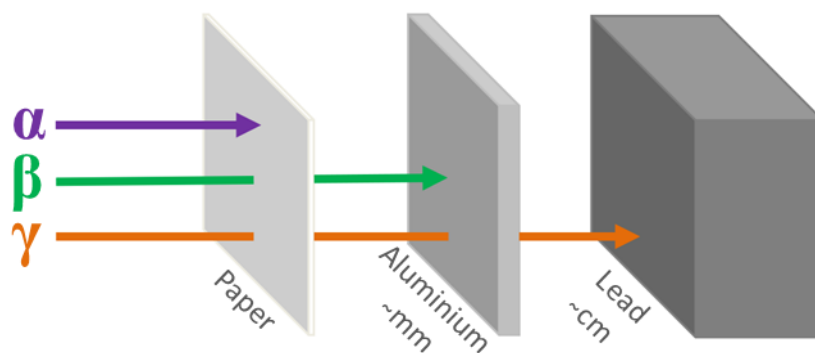


Figure 2.2 A schematic illustration of the interaction properties of three different types of radiation and the materials that will stop them.

Neutron radiation interacts slightly differently to the other radiations. Whereas γ radiation is attenuated most effectively by materials with a high atomic number (Z), neutrons are instead slowed most effectively by materials with a low atomic number [4]. Therefore, materials with a high hydrogen content, such as water and plastics, are particularly effective at moderating neutrons, i.e., reducing their energy.

The interaction and energy loss of a charged particle passing through matter can be described with the Bethe-Bloch equation [2],

$$-\frac{dE}{dx} = \left(\frac{Ze^2}{4\pi\epsilon_0}\right)^2 \frac{4\pi Z\rho N_A}{Amv^2} \left[\ln\left(\frac{2mv^2}{I}\right) - \ln(1 - \beta^2) - \beta^2 \right], \quad (2.6)$$

where $-\frac{dE}{dx}$ is the stopping power, or the change in energy of the particle (E) per unit distance into the material (x). The velocity of the particle is $v = \beta c$, the electric charge is given by Ze , Z is the atomic number, A is the atomic weight, and ρ is the density of the material the particle is passing through. Avogadro's number is N_A , m is the mass of the electron, and I is the mean energy required for ionisation per atom of the material.

From the Bethe-Bloch equation, the range, R , of a particle with kinetic energy T in the material can be calculated by [5]:

$$R = \int_T^0 \left(-\frac{dE}{dx}\right)^{-1} dE. \quad (2.7)$$

2.1.5.2 Dosimetry

For all types of radiation, the key principles to minimise exposure are distance, shielding and time. Radiation intensity associated with a point source reduces according to a $\frac{1}{r^2}$ relationship, where r is the distance from the source [6]. Therefore, keeping the maximum distance possible from a source is a good way to minimise exposure, in addition to shielding as much of the radiation as possible using the materials described earlier and also minimising the length of time exposed to the source. Dose can be monitored using dosimeters, typically thermoluminescent dosimeters (TLDs) which release light when heated in quantities proportional to the ionising dose absorbed. This is to ensure that exposures are well below the allowed limit for radiation workers, which consists of a 20 mSv effective dose annually [7]. Lancaster University has more

conservative limits of 6 mSv annually for staff and 1 mSv annually for students, with investigations to be carried out if a dose of 0.4 mSv is received in a 3-month period. In the UK, all activities should be ALARP – keeping the radiation exposure As Low As Reasonably Practicable - by determining the necessity of the activity and applying the above principles to minimise the dose.

2.1.5.3 Commonly used radiation detectors

There are a wide variety of devices for detecting radiation available, appropriate for different situations and purposes. A few common examples have been chosen to be discussed in the rest of this section, with some additional examples which are being considered specifically for the detection of α radiation and neutrons.

Gas-filled detectors are commonly used for radiation detection. The first of these to be considered is the ionisation chamber. As radiation passes through the chamber, ionisation occurs. The chamber is held under a voltage so that the resultant charge carriers produced can be collected without recombination occurring, resulting in a current proportional to the activity of the source [8]. If only a thin covering is placed over an ionization chamber, i.e., constituting as little impediment to the radiation entering the chamber as possible, α particles may be detected with this device. This is the method used for detecting α radiation in smoke detectors. Alternatively, if a thicker window is used α particles will be prevented from entering, allowing just β^- and γ radiation to be detected. These detectors are also commonly used in handheld survey meters to determine the dose rate, in particular for γ radiation as they are good at detecting high dose rates [9].

A proportional counter is similar to an ionisation chamber but operates at a much higher voltage. The higher voltage causes the electrons produced to generate secondary ionisations, amplifying the signal proportionally to the energy of the radiation. This

allows for discrimination between different types of radiation. They are commonly used for detecting environmental β^- radiation due to their low background and high stability, though they may also be used for detecting α and γ radiation [9].

Geiger counters are one of the most commonly-used detectors in laboratories to check for surface contamination, and in surveying areas to find hotspots of radiation due to their robustness, low cost, portability and fast response [10]. These are also gas-filled detectors which operate typically at higher voltages than proportional counters. The secondary ionisations will produce further ionisations, so that the chamber is saturated. Therefore, a Geiger counter will indicate when ionisation occurs within the Geiger-Müller tube, but not provide any energy information. This allows them to be used to identify that a radiation source is present and provide count rate information, but the type or energy of the radiation is not known and so Geiger counters cannot be used for characterisation [5].

Another type of detector use scintillator materials which produce light upon interaction with radiation, coupled with a photomultiplier tube (PMT) to collect and amplify the signal. The number of photons collected can provide information about the type of radiation being detected. A wide variety of scintillators are available, which are suitable for different applications. For example, organic scintillators are useful for detecting β^- radiation, but inorganic scintillators are better at detecting γ radiation due to their larger atomic numbers [1]. Liquid scintillators are also commonly used in the detection of α and β^- radiation, where the source is dissolved in the liquid scintillant. These are especially useful for low-energy detection [9].

The final type of detector to be discussed here is the semiconductor detector. These are typically used in laboratory environments and are particularly useful in the detection of α radiation. They consist of a semiconductor, usually a reverse-biased silicon or

germanium diode, to which a voltage is applied, behaving similarly to a solid ionisation chamber. The energy required for ionisation is approximately ten times less in these materials than for the gases used in ionisation chambers, allowing many more charge carriers to be produced. Silicon semiconductor detectors were created in 1951 to detect α particles and have seen much development since that time. They are now able to achieve high levels of energy resolution at room temperature [11]. Due to the higher atomic number of germanium, these types of semiconductor detector are more commonly used for detecting γ radiation.

2.1.5.4 Detectors for α radiation

The short range of α radiation can make it particularly difficult to detect. The detectors described in the previous section can be used to detect α radiation, but these are often not suitable for *in-situ* use or do not provide enough information about the source. In these situations, more specialist detectors are required. This has led to research for α detectors for use in specific environments.

A good example of an *in-situ* α -particle detector was reported by Morishita, *et al.*, which consists of a narrow detector on a flexible arm to navigate small areas [12]. The detector consists of a scintillator with a silicon photomultiplier which is capable of obtaining an energy spectrum. The detector is well designed for fitting in small spaces to look for contamination, but a relatively large data acquisition unit was required in addition to a laptop for analysing the data. As the arm is only 30 cm in length, this suggests the equipment needs to be set up to perform detection in a specific area at a time.

Pöllänen, *et al.*, have also developed a device for *in-situ* α -particle detection on flat surfaces, including air filters [13], [14]. The detector itself is a handheld silicon semiconductor detector, requiring additional equipment such as a multi-channel

analyser to be carried in a backpack. This takes energy spectra which can be used for particle identification. It uses a collimator to extract more accurate energy information, but this reduces the efficiency so that longer acquisition times are required.

New scintillator materials are also being developed with improved efficiency for detecting α radiation. An example of this is cerium-doped $\text{Gd}_3(\text{Ga},\text{Al})_5\text{O}_{12}$ (GAGG). This scintillator has a high efficiency and is sensitive to α , β and γ radiation. Discrimination between α and γ radiation can be performed by analysing the shapes of the pulses produced [15]. For detecting α radiation specifically, a thin crystal may be used to minimise the efficiency of detecting β and γ radiation, providing a high α -particle energy resolution [16].

Detection at a distance is particularly difficult for α radiation, though there are methods being considered. Two examples are to use the luminescence of nitrogen in the air and water [17]–[20]. Though these methods have been shown to be effective at measuring α radiation from a distance, they require complete darkness to ensure only the emitted photons are detected. There is also some research looking at the UVC range of emission, which is not emitted by artificial lights and is stopped in the atmosphere in light from the sun. This allows the distance detection of α radiation in the light [21]. However, the intensity of light produced in these wavelengths is very low, allowing this technique to only be successfully used to detect very high activity sources.

2.1.5.5 Neutron detection

The strong penetration and activation properties of neutron radiation cause it to be a particular health concern. As neutrons are not ionising, detection of these relies on nuclear interactions such as (n, p) , (n, α) or (n, γ) reactions where the produced radiation can be detected, or through detecting recoiling ions from neutron scattering in moderators [5]. The first technique is typically performed for detecting low-energy

neutrons by using a material such as BF_3 or ^3He gas in a proportional counter, where the ions produced in these reactions can be detected.

Higher-energy neutrons have lower interaction cross-sections for these reactions, reducing the detection efficiency. However, their greater energy will generate more energetic recoils in scattering events. These scattering events are more likely to occur in plastics and organic scintillators as described in Section 2.1.4. The high hydrogen content in these materials means recoiling protons can be produced, which will be detected in the usual way within the scintillator using a PMT [1], [2].

2.2 Charge-coupled devices

This section will introduce charge-coupled devices (CCDs), starting with a brief history. Their general operation will be described, along with some different structures which are used. The prior art relevant to this research, relating to the interactions of radiations with CCDs, will then be visited, including the effects of radiation damage in CCDs. Finally, a brief comparison with the competing CMOS (complementary metal-oxide-semiconductor) technology will be given.

2.2.1 CCD history

Charge-coupled devices were initially created at Bell Laboratories by Willard Boyle and George Smith in 1969 [22], [23]. The purpose of these was to act as a memory device, competing with other technologies such as magnetic bubble memory and silicon diode arrays. They were designed initially for use in improving AT&T's Picturephone, a video-phone device that was ultimately unsuccessful, but they rapidly saw use in many imaging technologies. Over time, CCDs have seen vast improvements allowing for a greater range of pixel sizes and numbers. This has increased the range of their imaging

applications further, for example they are commonly used in medical imaging and astronomy, both land-based and in space.

2.2.2 CCD operation

The basic structure of a CCD consists of three layers: a gate structure, containing the electrodes used to control the charge transfer; the active area of depleted silicon where the charge carriers that constitute the evolved signal are produced; and a substrate layer of undepleted silicon. As light passes through a pixel in a CCD, ionisation occurs in the active area. When the CCD is in operation a bias is applied to the gate electrodes, allowing the generated charge to be collected and transferred through the adjacent pixels in a line to a readout register [24]. A simplified diagram of a cross-section of these layers demonstrating the processes of ionisation, charge collection, and charge transfer is shown in Figure 2.3. The read out is then used to produce a pixel image based on the location of the created charge on the imaging area. The intensity of each pixel is determined by the amount of charge carriers collected, converted to a value typically between 0 and 255 ADU (Analog to Digital Units). For a typical camera, this is how a photograph is produced.

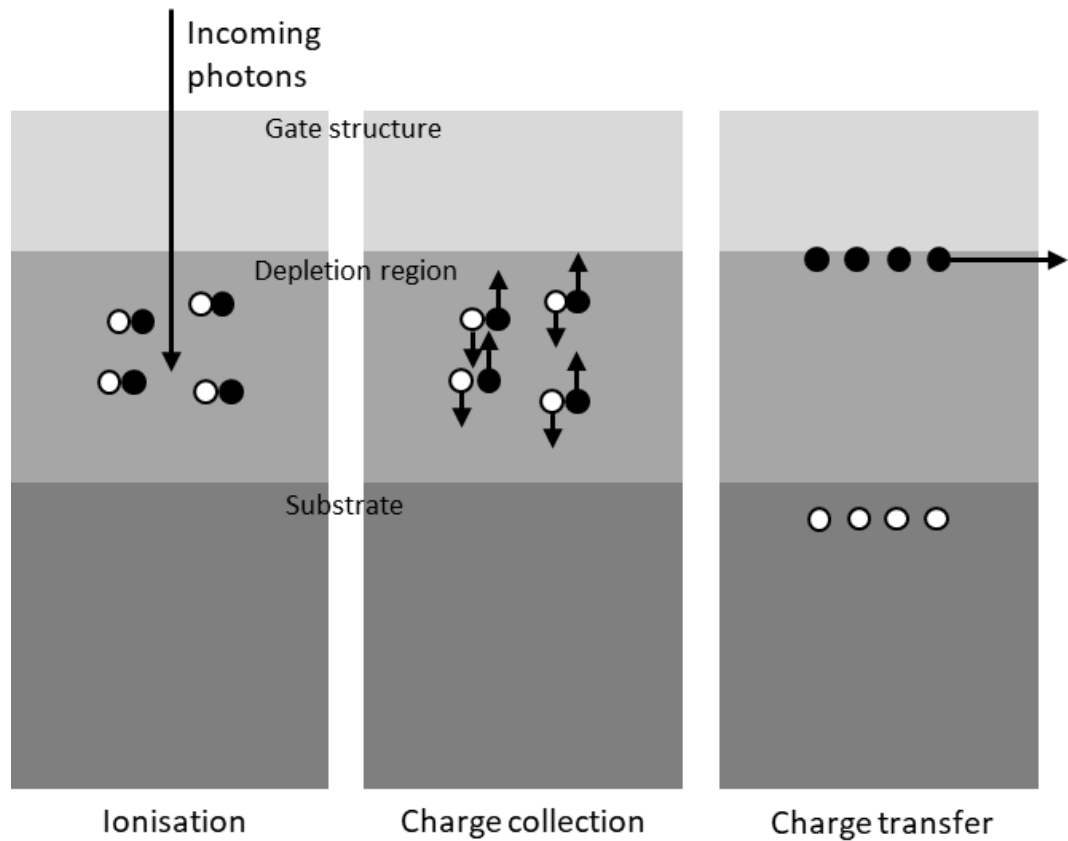


Figure 2.3 Charge carrier production, collection, and transfer in a CCD pixel. The black and white circles represent negative and positive charge carriers, respectively.

The charge carriers, typically electrons, are transferred through the use of silicon electrodes in the gate structure. These are encased in an insulator, typically silicon dioxide, to separate the electrodes from each other and the depleted silicon region. The electrodes are used in a multi-phase structure where the potential is increased and decreased to make the charge move across pixels. It is then collected at a readout register and processed to reconstruct a pixel image of the frame taken.

One of the most commonly used CCD structures, created shortly after the initial concept of the device, is the three-phase CCD. This has three electrodes in the gate structure per pixel, which can each have their potential adjusted separately [25]. The charge is collected initially below one electrode. The potential is then lowered in the adjacent

electrode, allowing the charge to move across. This is repeated, moving the charge carriers along the entire register to be read out at the end [22], [26]. A demonstration of this can be seen in Figure 2.4, where the three different electrodes per pixel are shown in orange, red and green, with the insulator shown in yellow. Below are representations of the potentials passing through the electrodes at different times, showing how the charge carriers pass through the pixels. 2- or 4-phase devices may also be used, operating in a similar manner to the 3-phase device to transfer charge [24].

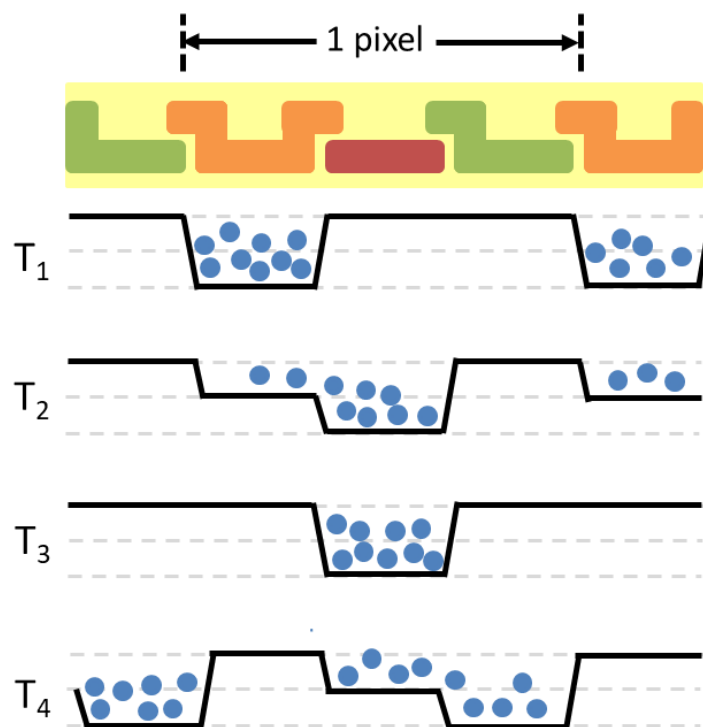


Figure 2.4 Top: Three-phase CCD gate structure. Below: Potentials across the gates at four different times, T_{1-4} , showing how the charge is transferred.

2.2.2.1 Buried-channel CCDs

Many CCDs use a buried channel for storing the charge away from the interface between the depleted silicon of the active region and the oxide layer of the gate structure. This is to avoid trapping which commonly occurs at this boundary. Charge carriers collected by traps can be held for a time, but later be re-emitted. The time the

charge is held for decreases with increasing temperature, so the traps become less significant at higher temperatures as the charge is more likely to be re-emitted quickly into the same charge packet [27]. The traps cause a decrease in charge transfer efficiency (CTE) and an increase in dark current [27][28]. The CTE is defined as the fraction of charge successfully transferred per pixel, and so becomes more important with larger devices, where the charge must be transferred over a greater number of pixels [29], [30].

Dark current is noise produced by thermal fluctuations in the CCD. Charge carriers may be produced due to areas of high temperature within the CCD. These are read out in the same manner as charge carriers produced by photon interaction, and so are visible on the resultant images as singular, bright pixels. All CCDs have some dark current, but this can be increased by operating at higher temperatures, or through radiation damage as will be discussed in Section 2.2.4. In situations where a high sensitivity is required, for example many scientific applications, the CCDs used are operated with cooling to minimise the dark current [31]. Therefore, at these cooler temperatures, the traps at the oxide interface become more significant and it is important to reduce them through the use of a buried channel.

The buried channel is formed by including a lightly n-doped region at the boundary, varying the potential and allowing the charge carriers to be held away from the oxide interface, as shown in Figure 2.5 [23], [26], [32]. This keeps the CTE high and dark current low.

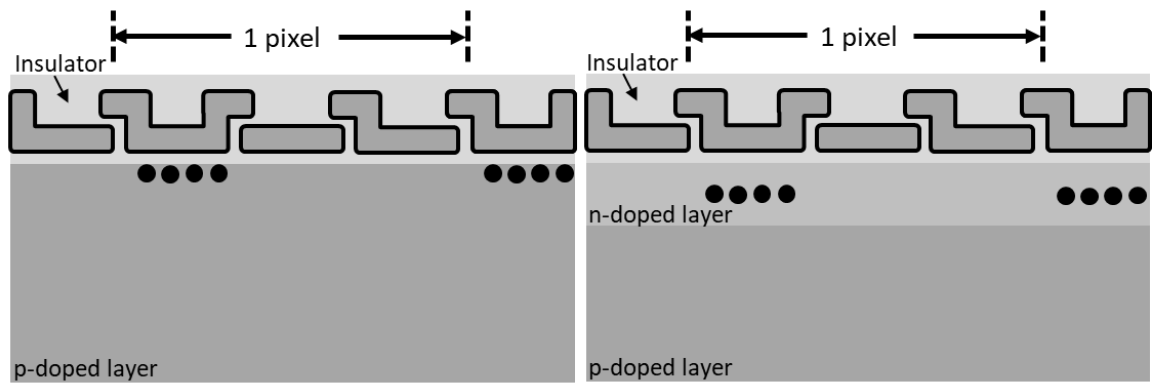


Figure 2.5 Diagrams showing the effect of the surface channel (left) vs the buried channel (right) on the location of charge carriers (black dots) within the CCD.

2.2.2.2 Illumination

Originally, CCDs were front illuminated, with light incident on the gate structure, above the depletion region and substrate as previously described. For sensitive applications, a back-illuminated CCD was developed where the light is instead incident on the substrate side [33]. For this, the substrate is thinned to be only a few μm thick. This means that there is no loss of intensity in the gate structure of the CCD. A comparison of the different structures can be seen in Figure 2.6.

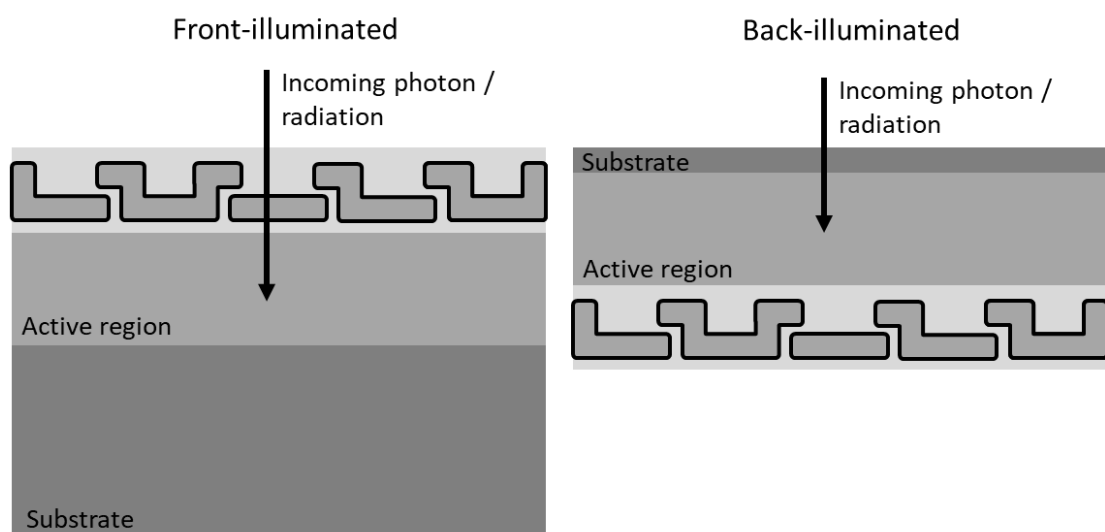


Figure 2.6 Front- and back-illuminated CCD structures.

Front-illuminated devices are still commonly used as they are easier to manufacture than back-illuminated devices, and hence are more readily available at lower costs. However, for applications where a high sensitivity is required a back-illuminated device is a significantly better option [34].

2.2.2.3 Charge transfer

There are different structures in place to take the image and transfer the charge. The two most common architectures are interline transfer and frame transfer. The basic structure of these are shown in Figure 2.7.

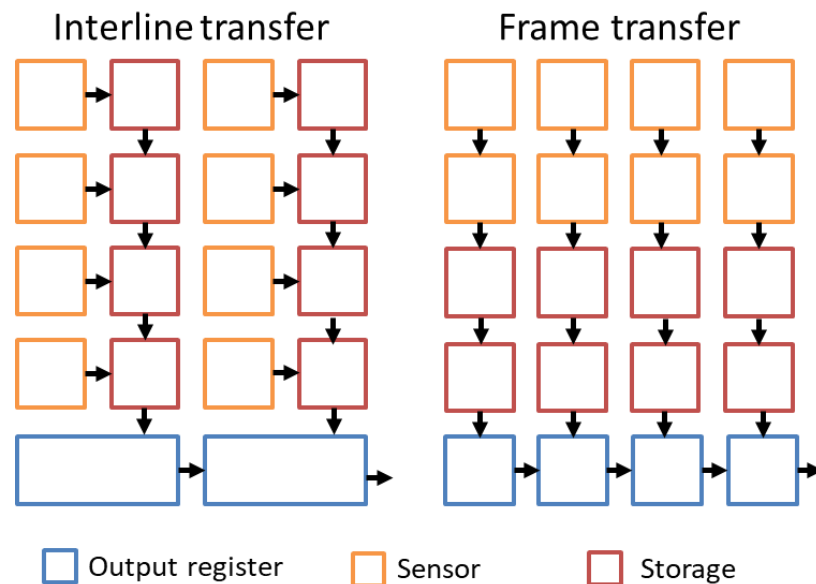


Figure 2.7 Comparison of interline (left) and frame (right) transfer structures, showing the movement of the charge carriers into and along the output register.

For interline CCDs, half of the imaging area consists of storage. Charge carriers are transferred from the sensors directly into these neighbouring storage pixels, where they are then passed down into the output register. This allows continuous exposure to occur.

Frame transfer CCDs expose the entire imaging area, then transfer through the imaging pixels into the storage pixels away from the imaging area. This means a shutter is required to prevent smeared images as the charge is transferred through. The benefit of

the frame transfer device over interline transfer is that they are more sensitive, as more of the pixel area can be used for imaging. By comparison, interline CCD pixels must have some area devoted to storage [26], [31].

2.2.2.4 Blooming and anti-blooming

Blooming is a common problem in CCDs when exposed to high intensity light. This is commonly seen in photographs, such as when a photo is taken of a bright light source. It results in straight lines emanating from the source of the light, such as a bright star as in Figure 2.8. It occurs when enough charge carriers are produced that a pixel reaches its capacity, and excess charge carriers overflow into subsequent readout cycles, creating a streak [35]. This can occur in either horizontal or vertical directions, depending on the CCD, though is most commonly seen as a vertical streak emanating both above and below the bright object.

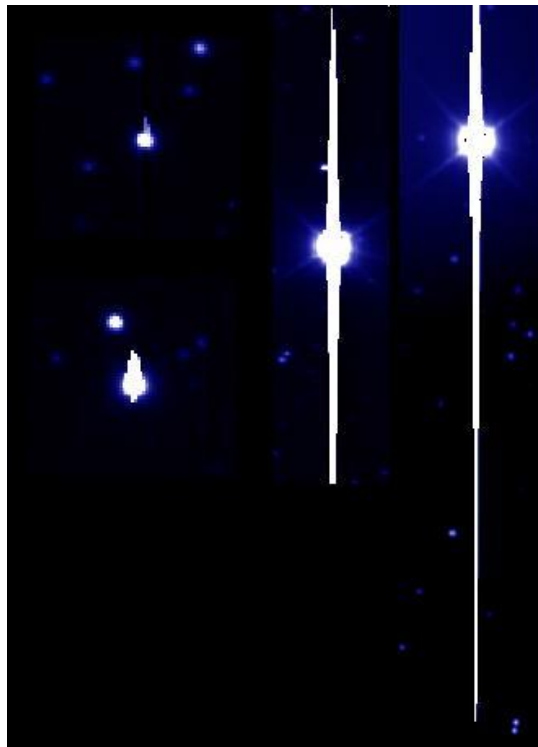


Figure 2.8 Three examples of blooming occurring in images taken of stars with a CCD. Image from [36].

Some CCDs have anti-blooming structures to try and reduce this problem. This consists of a drain located between pixels in the direction of overflow. This drain has its own electrode, so that the potential can be set such that any excess charge carriers will preferentially overflow into this drain, which is not part of the readout process, instead of overflowing into an adjacent pixel [35].

2.2.2.5 Pixel binning

A common technique to reduce read noise in CCDs is to ‘bin’ pixels. Read noise is separate from the noise produced by dark current, and instead occurs during the readout phase of operation. Binning is the process of reading out multiple pixels together, either vertically, horizontally, or in both directions. As the binning is performed on-chip and multiple pixels are collected together, the read noise is only added once per bin, reducing the total by a factor of the number of pixels in the bin. For example, in a 2×2 pixel bin, the read noise is reduced by 4. This improves the signal to noise ratio and readout rate, but reduces the resolution of the image [31], [37].

2.2.3 Radiation detection with CCDs

Ionising radiation interacts with a CCD in a similar manner to light. If a CCD is covered so that light cannot interact and the CCD is instead exposed to ionising radiation, the image produced shows where the radiation interacted in the device. As with light, the radiation will cause ionisation in the pixels it passes through. Each particle or ray will interact separately, leaving individual trails or clusters of pixels indicating where the interactions occur.

There has been a lot of research into the interactions of radiation with CCDs, most commonly investigating at the interactions of γ -rays, x-rays, and muons from cosmic radiation through their use in astronomy [38], [39]. Much of this research considers interactions from radiation to be an unwanted phenomenon and considers methods to

isolate and minimise the tracks seen from both cosmic radiation and local sources, including contamination within the CCDs themselves [40], [41].

Multiple works have shown that different types of radiation give different responses in CCDs. Due to their low rates of interaction, γ radiation and x-rays leave small clusters or single pixel signals. Scattering will occur with β particles, ionising the material as it passes through multiple pixels, leaving curved trails [39]–[41]. Though more strongly interacting, α particles are diverted less due to their much larger mass, whilst depositing considerably more energy. This causes some pixels to reach their capacity and overflow, leading to larger, symmetrical clusters and in some cases vertical streaks from blooming [41]–[43]. Examples of some of these different signals can be seen in Figure 2.9.

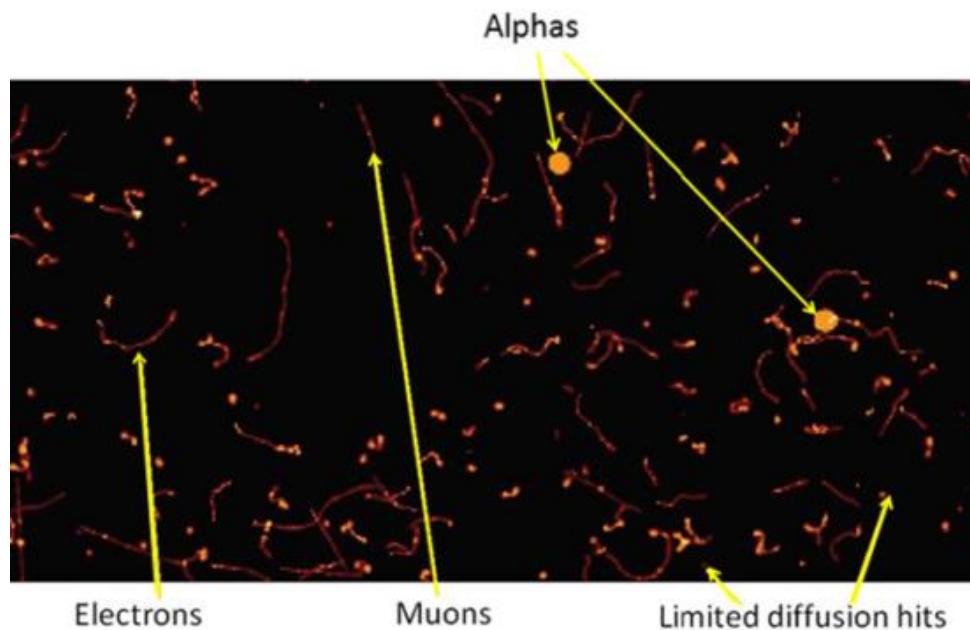


Figure 2.9 Example tracks formed by interactions of different radiation types from an exposure of the DECam CCD to cosmic rays. Image taken from [42].

Neutron detection has also been considered using CCDs. Though they will not interact directly with the CCD, a scintillator may be placed over the CCD and the light that is produced by the interactions with neutrons can subsequently be detected [44], [45].

2.2.3.1 Interactions of α radiation with CCDs

Relatively little research has been performed with the specific intention to perform α radiation detection and spectroscopy with CCDs. One of the earliest instances of detecting α particles in CCDs was in 1980 by Ko [46]. This was an analysis of α particles produced by impurities in the materials used to make these CCDs. Similar studies of impurities producing α -particles have also been performed recently [39], [47]. Another more common situation for investigating α -particle interactions in CCDs are to consider the damage caused by charged particles in CCDs designed for use in space environments, as will be discussed more in Section 2.2.4 [27], [48].

There are some examples from the 1990s considering the use of these devices to detect charged particles such as α particles and protons with both front- and back-illuminated CCDs [43], [49]. It was suggested that these might be used for charged particle diagnostics for inertial confinement fusion. More recently in 2011, Chabot *et al.* considered the use of a back-illuminated CCD for detecting charged particles at accelerator facilities [50]. Large round clusters were observed, but no blooming occurred.

Heavy ions were investigated by Lomheim, *et al.*, who observed straight line trails in the direction of charge transport, or blooming [51]. Over the four ions used, it was seen that an increased linear energy transfer (LET) yielded a wider cluster and longer trail, demonstrated in Figure 2.10. These are very similar to the patterns seen for CCD blooming when exposed to bright stars, as in Figure 2.8.

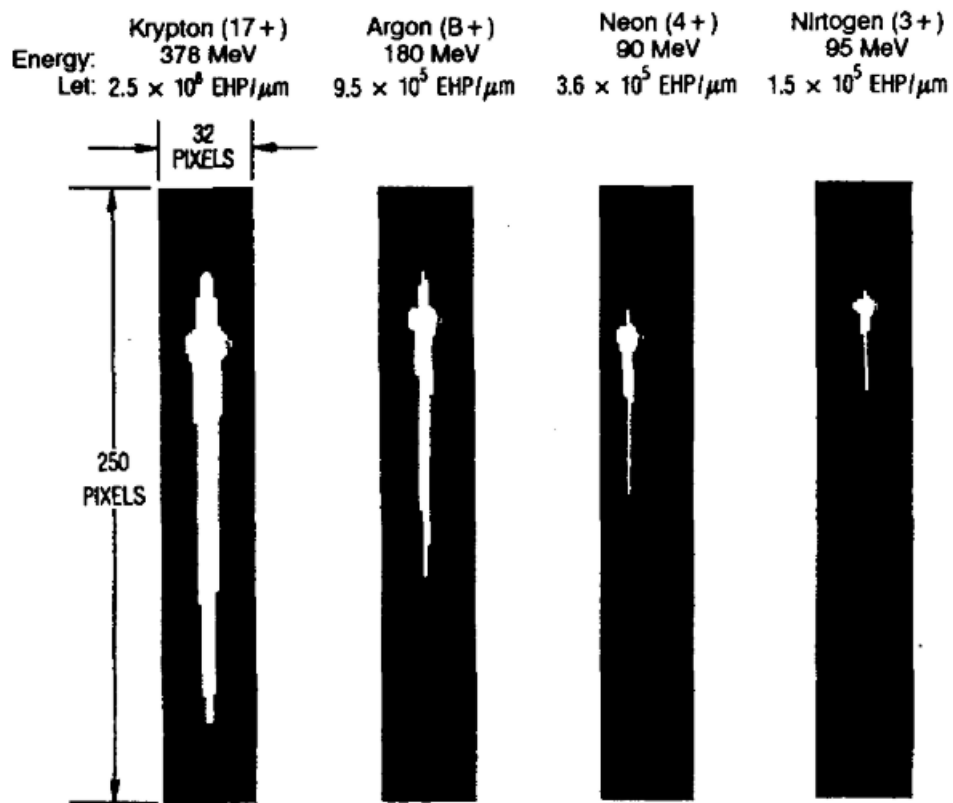


Figure 2.10 The response of heavy ions with decreasing LET, demonstrating the reduction in the length of the streaks. Image taken from [51].

These streaks caused by blooming have also been seen rarely with α -particle interactions, in addition to the larger round clusters. Examples of these can be seen in Figure 2.11. Aguilar-Arevalo, *et al.*, who produced these images also determined some techniques to discriminate between these clusters produced by α particles and the curved tracks seen by β^- radiation based on analysis of the shapes produced [41]. This was also for the purpose of identifying contaminants within the CCD itself. When considering the interactions of radiation with CCDs, blooming is unique to α particles due to their high energies and strong interactions. This process is therefore potentially a key identifier for the presence of α radiation although this had not been explored conclusively until this study.

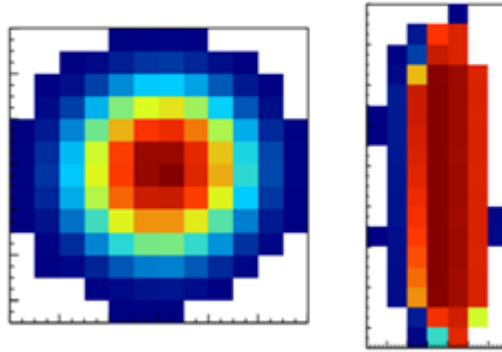


Figure 2.11 Examples of an α -particle cluster (left) and streak (right) from interactions within a DAMIC CCD. Images taken from [41].

Blooming with α radiation is more likely to occur in a front-illuminated CCD due to the α particles stopping a shorter distance in the pixel and leaking over the vertical barriers. This will not occur in a back-illuminated CCD as they are further from the depletion region and more likely to spread solely by the plasma effect [49], [50], [52], [53]. The plasma effect is a diffusion of the charge carriers into the surrounding pixels through the substrate, typically creating large, round clusters [42]. This will occur in both types of CCD.

2.2.4 Radiation damage in CCDs

Many CCDs are used in environments where they are exposed to radiation. Therefore, there have been studies looking at the effects of radiation damage on CCDs. Though different CCDs will exhibit different responses, there are some common features. In general, there are two types of damage that may be caused by radiation. The first is damage caused from ionisation, and the second is displacement damage from neutrons and charged particles [48], [54]–[57].

2.2.4.1 Ionisation damage

Ionisation is the mechanism by which radiation is detected in CCDs, as the electron-hole pairs produced are collected and measured. However, ionisation is not desired in

the oxide layers as this leads to trapped charges at the interface between the insulator and the active area and in the insulator itself, causing a change in the gate potential [58]–[60]. This leads to reduced CTE by reducing the amount of charge that can be transferred, and an increase in the dark current. The degradation of CTE occurs linearly with total ionising dose [54]. Changes in the gate potential occur more readily when the CCD is biased during exposure [28], [58].

2.2.4.2 Displacement damage

Neutrons and charged particles can interact elastically with atoms in the CCD, displacing them. Some of these displaced atoms will recombine with the vacancies left behind, however others will persist or join with a dopant atom, forming a defect acting as a trap in the active area and buried channel of the CCD [29], [61]. Whether exposure occurs biased or unbiased has a less significant impact on displacement damage [62]. Of the radiations considered in this research, α radiation will be the most likely to cause displacement damage in CCDs, due to their relatively large mass and momentum [63], [64].

These traps act similarly to those at the interface which are avoided through use of the buried channel, to increase the dark current and decrease the CTE of the device. However, as these occur where the ionisations are taking place, they are not as easy to circumvent. The effects of traps may be reduced by injecting charge to fill the traps before signals occur, though this may cause a variation in gain over the CCD [27], [30], [65], [66].

2.2.4.3 Damage mitigation

To repair the damage caused by radiation, a commonly applied technique is to anneal the CCDs. This is a process by which the CCDs are heated up for a period of time to allow the traps to dissipate. The heat gives kinetic energy to the displaced atoms so they

migrate and potentially re-join with the vacancies, removing the traps. As CCDs are often operated cooled, annealing may be done by raising the CCD to still very cool temperatures (-30°C) or room temperature [30], [67], [68]. For CCDs that operate at room temperature a higher annealing temperature is required. This can vary from 30-350 degrees, depending on the materials and severity of the radiation damage [28], [46], [58], [63]. Different traps which may be produced by the radiation damage will require different temperatures to anneal out [69]. In each instance the time of annealing can also vary, from 30 mins to weeks between operations.

As discussed previously, the temperature of the CCD has a strong effect on the dark current and CTE [27], [58]. Therefore, operating a lower temperature will reduce these issues. Cooling will also reduce the effects of radiation damage, by reducing the noise produced by the traps, making the damage less noticeable. However, cooler temperatures also make the CCD more susceptible to radiation damage [68].

P-channel CCDs have been shown to be more tolerant to radiation damage than n-channel CCDs [70], [71]. This is because they are not subject to the same electron trapping in the phosphorous vacancy, one of the main defects caused by displacement damage in n-channel CCDs, as a boron dopant is used instead of the phosphorous commonly used. However, p-channel CCDs are not commonly commercially available.

2.2.5 Comparison with CMOS

CMOS (complementary metal-oxide-semiconductor) sensors are a competitor for CCDs in many modern devices. These devices detect light by the same methods, but the readout is done per-pixel, without the need to transfer the charge between pixels to a readout register. Though these technologies were originally developed around the same time, the CCD became the dominant device used in cameras, with superior overall performance. However, more recently, CMOS technology has been increasing in

popularity due to lowering costs and increases in efficiency as the technology has matured, with CMOS becoming dominant in digital cameras and seeing increasing use in scientific applications [72].

In many cases, CMOS can be preferable as the readout method is quicker, without smear or charge transfer inefficiency, and less dark current [64]. Another benefit of CMOS is a lower power requirement, allowing for a longer battery life when used in portable devices. However, more of the photosensitive area is taken up by the readout electronics [73]. The additional electronics required on-pixel for CMOS means that for a similar photosensitivity, larger pixel sizes are required than for CCDs [72]. Therefore, for comparable pixel sizes CCDs have a better sensitivity to both photons and ionising radiation.

CMOS devices can exhibit a greater amount of noise due to the additional circuitry per pixel [74]. However, they have also been shown to be more tolerant of ionising radiation, with a less significant increase in noise with total ionising dose [75]. CMOS sensors do show potential for detecting ionising radiation, producing similar images as with CCDs [76], [77]. The primary reason CCDs are being considered for this research, rather than CMOS devices is the unique interaction of α particles with CCDs characterised by the vertical streaks from blooming described earlier. This is due to the readout process of a CCD, and as such would not be seen on a CMOS device.

2.3 References

- [1] G. F. Knoll, *Radiation Detection and Measurement*. John Wiley & Sons, 1989.
- [2] J. S. Lilley, *Nuclear Physics: Principles and Applications*. John Wiley & Sons, 2001.
- [3] C. Leroy and P.-G. Rancoita, *Principles of Radiation Interaction in Matter and*
Characteristic responses of a COTS CCD to α , β -, and neutron-induced triton radiations and strategies to reduce noise

Detection. World Scientific, 2009.

- [4] M. Licata, M. J. Joyce, I. Tsitsimpelis, D. Clark, and B. A. Shippen, “The potential of real-time, fast neutron and γ radiography for the characterization of low-mass, solid-phase media,” *Nucl. Instruments Methods Phys. Res. Sect. A Accel. Spectrometers, Detect. Assoc. Equip.*, no. July, pp. 10–13, 2018.
- [5] K. S. Krane, *Introductory Nuclear Physics*. John Wiley & Sons, 1988.
- [6] J. E. Martin, *Physics for Radiation Protection*. John Wiley & Sons, 2013.
- [7] “The Ionising Radiations Regulations 2017.” SI 2017/1075, 2017.
- [8] L. Cerrito, *Radiation and Detectors: Introduction to the Physics of Radiation and Detection Devices*. Springer, 2017.
- [9] J. R. Cooper, K. Randle, and R. S. Sokhi, *Radioactive Releases in the Environment: Impact and Assessment*. John Wiley & Sons, 2003.
- [10] A. J. Crompton, K. A. A. Gamage, A. Jenkins, and C. J. Taylor, “Alpha particle detection using alpha-induced air radioluminescence: A review and future prospects for preliminary radiological characterisation for nuclear facilities decommissioning,” *Sensors (Switzerland)*, vol. 18, no. 4, 2018.
- [11] C.-D. Lee, T. Hartnett, and R. Tustison, “Development of radiation detection materials,” *Micro- Nanotechnol. Sensors, Syst. Appl. IV*, vol. 8373, no. May 2012, p. 83730X, 2012.
- [12] Y. Morishita, S. Yamamoto, K. Izaki, J. H. Kaneko, and N. Nemoto, “Flexible alpha camera for detecting plutonium contamination,” *Radiat. Meas.*, vol. 103, pp. 33–38, Aug. 2017.

- [13] R. Pöllänen, K. Peräjärvi, T. Siiskonen, and J. Turunen, “In-situ alpha spectrometry from air filters at ambient air pressure,” *Radiat. Meas.*, vol. 53–54, pp. 65–70, 2013.
- [14] R. Pöllänen *et al.*, “Novel Equipment for In Situ Alpha Spectrometry with Good Energy Resolution,” *Health Phys.*, vol. 109, no. 6, pp. 601–605, 2015.
- [15] M. Kobayashi, Y. Tamagawa, S. Tomita, A. Yamamoto, I. Ogawa, and Y. Usuki, “Significantly different pulse shapes for γ - and α -rays in $\text{Gd}_3\text{Al}_2\text{Ga}_3\text{O}_{12}:\text{Ce}^{3+}$ scintillating crystals,” *Nucl. Instruments Methods Phys. Res. Sect. A Accel. Spectrometers, Detect. Assoc. Equip.*, vol. 694, pp. 91–94, Dec. 2012.
- [16] Y. Morishita, S. Yamamoto, K. Izaki, J. H. Kaneko, K. Hoshi, and T. Torii, “Optimization of thickness of GAGG scintillator for detecting an alpha particle emitter in a field of high beta and gamma background,” *Radiat. Meas.*, vol. 112, pp. 1–5, May 2018.
- [17] S. M. Baschenko, “Remote optical detection of alpha particle sources,” *J. Radiol. Prot.*, vol. 24, no. 1, pp. 75–82, Mar. 2004.
- [18] J. Sand *et al.*, “Imaging of alpha emitters in a field environment,” *Nucl. Instruments Methods Phys. Res. Sect. A Accel. Spectrometers, Detect. Assoc. Equip.*, vol. 782, pp. 13–19, May 2015.
- [19] F. Lamadie, F. Delmas, C. Mahe, P. Girones, C. Le Goaller, and J. R. Costes, “Remote alpha imaging in nuclear installations: new results and prospects,” *IEEE Trans. Nucl. Sci.*, vol. 52, no. 6, pp. 3035–3039, Dec. 2005.
- [20] S. Yamamoto, M. Komori, S. Koyama, and T. Toshito, “Luminescence imaging of water during alpha particle irradiation,” *Nucl. Instruments Methods Phys. Res.*

- Sect. A Accel. Spectrometers, Detect. Assoc. Equip.*, vol. 819, pp. 6–13, May 2016.
- [21] A. J. Crompton, K. A. A. Gamage, S. Bell, A. P. Wilson, A. W. Jenkins, and D. Trivedi, “Gas flow to enhance the detection of alpha-induced air radioluminescence based on a UVTron flame sensor,” *Sensors (Switzerland)*, vol. 18, no. 6, pp. 1–11, 2018.
- [22] W. S. Boyle and G. E. Smith, “Charge Coupled Semiconductor Devices,” *Bell Syst. Tech. J.*, vol. 49, no. 4, pp. 587–593, Apr. 1970.
- [23] G. E. Smith and W. S. Boyle, “The invention and early history of the CCD,” *J. Appl. Phys. Rev. Sci. Instrum. Proc. J. Phys. J. Bell Syst. Tech. J.*, vol. 109, no. 49, pp. 102421–83907, 2011.
- [24] J. R. Janesick, *Scientific Charge-coupled Devices*. SPIE Press, 2001.
- [25] C. H. Sequin, F. J. Morris, T. A. Shankoff, M. F. Tompsett, and E. J. Zimany, “Charge-coupled area image sensor using three levels of polysilicon,” *IEEE Trans. Electron Devices*, vol. 21, no. 11, pp. 712–720, Nov. 1974.
- [26] S. M. Sze and K. K. Ng, *Physics of Semiconductor Devices*, 3rd ed. Hoboken: John Wiley & Sons, 2006.
- [27] N. Meidinger, B. Schmalhofer, and L. Strüder, “Particle and X-ray damage in pn-CCDs,” *Nucl. Instruments Methods Phys. Res. Sect. A Accel. Spectrometers, Detect. Assoc. Equip.*, vol. 439, no. 2–3, pp. 319–336, Jan. 2000.
- [28] G. R. Hopkinson, “Cobalt60 and Proto Radiation Effects on Large Format, 2-D, CCD Arrays for an Earth Imaging Application,” *IEEE Trans. Nucl. Sci.*, vol. 39, no. 6, 1992.

- [29] G. R. Hopkinson, C. J. Dale, and P. W. Marshall, "Proton effects in charge-coupled devices," *IEEE Trans. Nucl. Sci.*, vol. 43, no. 2 PART 1, pp. 614–627, 1996.
- [30] S. M. Baggett *et al.*, "HST/WFC3: understanding and mitigating radiation damage effects in the CCD detectors," no. July 2016, p. 99045D, 2016.
- [31] S. B. Howell, *Handbook of CCD Astronomy*. Cambridge University Press, 2006.
- [32] J. Killiany, "Radiation Effects on Silicon Charge-Coupled Devices," *IEEE Trans. Components, Hybrids, Manuf. Technol.*, vol. 1, no. 4, pp. 353–365, Dec. 1978.
- [33] D. G. Rabus, *Optofluidics Systems Technology*. De Gruyter, 2014.
- [34] M. Lesser, "A Summary of Charge-Coupled Devices for Astronomy," *Publ. Astron. Soc. Pacific*, vol. 127, no. 957, pp. 1097–1104, Nov. 2015.
- [35] A. Theuwissen, *Solid-state Imaging with Charge-Coupled Devices*. 1995.
- [36] O. Hainaut, "CCD Artifacts," 1996. [Online]. Available: https://www.eso.org/~ohainaut/ccd/CCD_artifacts.html. [Accessed: 03-Nov-2019].
- [37] G. C. Holst, *CCD Arrays Cameras and Displays*. 1998.
- [38] G. R. Hopkinson, "Charge diffusion effects in CCD X-ray detectors," *Nucl. Instruments Methods Phys. Res.*, vol. 216, no. 3, pp. 423–429, Nov. 1983.
- [39] T. Saad Saoud *et al.*, "Use of CCD to Detect Terrestrial Cosmic Rays at Ground Level: Altitude vs. Underground Experiments, Modeling and Numerical Monte Carlo Simulation," *IEEE Trans. Nucl. Sci.*, vol. 61, no. 6, pp. 3380–3388, Dec. 2014.

- [40] A. R. Smith *et al.*, “Radiation events in astronomical {CCD} images,” *Proc. SPIE*, vol. 4669, pp. 172–183, Apr. 2002.
- [41] A. Aguilar-Arevalo *et al.*, “Measurement of radioactive contamination in the high-resistivity silicon CCDs of the DAMIC experiment,” *J. Instrum.*, vol. 10, no. 08, pp. P08014–P08014, Aug. 2015.
- [42] J. Estrada, J. Molina, J. J. Blostein, and G. Fernández, “Plasma effect in silicon charge coupled devices (CCDs),” *Nucl. Instruments Methods Phys. Res. Sect. A Accel. Spectrometers, Detect. Assoc. Equip.*, vol. 665, pp. 90–93, 2011.
- [43] B. E. Burke, R. D. Petrosso, C. K. Li, and T. C. Hotaling, “Use of charge-coupled device imagers for charged-particle spectroscopy,” *Rev. Sci. Instrum.*, vol. 68, no. 1 pt 2, pp. 599–602, 1997.
- [44] J. J. Blostein, J. Estrada, A. Tartaglione, M. S. Haro, G. F. Moroni, and G. Cancelo, “Development of a novel neutron detection technique by using a boron layer coating a Charge Coupled Device,” *J. Instrum.*, vol. 10, no. 01, pp. P01006–P01006, Jan. 2015.
- [45] O. Bourrion *et al.*, “C2D8: An eight channel CCD readout electronics dedicated to low energy neutron detection,” *Nucl. Instruments Methods Phys. Res. Sect. A Accel. Spectrometers, Detect. Assoc. Equip.*, vol. 880, pp. 28–34, Feb. 2018.
- [46] S.-B. Ko, “Observation of Alpha Particle Effects in the Charge-Coupled Image Sensor,” *IEEE Trans. Nucl. Sci.*, vol. 27, no. 6, pp. 1500–1505, 1980.
- [47] A. Aguilar-Arevalo *et al.*, “Measurement of radioactive contamination in the CCD’s of the DAMIC experiment,” *J. Phys. Conf. Ser.*, vol. 718, p. 042057, May 2016.

- [48] G. R. Hopkinson and A. Mohammadzadeh, "CCD Radiation Testing at Low Temperatures Using a Laboratory Alpha Particle Source," *IEEE Trans. Nucl. Sci.*, vol. 53, no. 6, pp. 3758–3763, Dec. 2006.
- [49] C. K. Li *et al.*, "Charged-coupled devices for charged-particle spectroscopy on OMEGA and NOVA," *Cit. Rev. Sci. Instruments Rev. Sci. Instrum.*, vol. 68, no. 68, 1997.
- [50] M. Chabot *et al.*, "Detection of atomic and molecular mega-electron-volt projectiles using an x-ray charged coupled device camera.," *Rev. Sci. Instrum.*, vol. 82, no. 10, p. 103301, Oct. 2011.
- [51] T. S. Lomheim *et al.*, "Imaging charge-coupled device (ccd) transient response," pp. 1876–1885, 1990.
- [52] M. Campbell, E. Heijne, C. Lebel, C. Leroy, X. Llopart, and L. Tlustos, "Study of the charge sharing in silicon pixel detector by means of alpha particles interacting with a Medipix2 device," *Nucl. Instruments Methods Phys. Res. A*, vol. 591, pp. 1–34, 2007.
- [53] D. G. Hicks *et al.*, "Design of an electronic charged particle spectrometer to measure $\langle \rho R \rangle$ on inertial fusion experiments," *Rev. Sci. Instrum.*, vol. 68, no. 1, p. 589, 1997.
- [54] R. A. Williams and R. D. Nelson, "Radiation effects in charge coupled devices," *IEEE Trans. Nucl. Sci.*, vol. 22, no. 6, pp. 2639–2644, 1975.
- [55] Z. Wang *et al.*, "Displacement damage induce degradation of COTS array CCDs irradiated by neutron beams from a nuclear reactor," *Nucl. Instruments Methods Phys. Res. Sect. A Accel. Spectrometers, Detect. Assoc. Equip.*, vol. 771, pp. 49–

54, 2015.

- [56] F. Li and A. Nathan, *CCD Image Sensors in Deep-Ultraviolet: Degradation Behavior and Damage Mechanisms*. Springer Science & Business Media, 2006.
- [57] J. Schott, “Charge coupled devices (CCDs) — A detector system for particles with time resolution and local assignment with particle trajectories,” *Int. J. Radiat. Appl. Instrumentation. Part D. Nucl. Tracks Radiat. Meas.*, vol. 15, no. 1–4, pp. 81–89, Jan. 1988.
- [58] J. Janesick, T. Elliott, and F. Pool, “Radiation damage in scientific charge-coupled devices,” *IEEE Trans. Nucl. Sci.*, vol. 36, no. 1, pp. 572–578, 1989.
- [59] Z. Wang *et al.*, “Radiation damage evaluation of the CCD detector induced by high energy protons,” *Nucl. Instruments Methods Phys. Res. Sect. A Accel. Spectrometers, Detect. Assoc. Equip.*, no. June, pp. 5–10, 2018.
- [60] D. Burt *et al.*, “Improving radiation tolerance in e2v CCD sensors,” *Astron. Sp. Opt. Syst.*, vol. 7439, no. August 2009, p. 743902, 2009.
- [61] R. Germanicus *et al.*, “Evaluation and prediction of the degradation of a COTS CCD induced by displacement damage,” *IEEE Trans. Nucl. Sci.*, vol. 49 I, no. 6, pp. 2830–2835, 2002.
- [62] G. R. Hopkinson, “Proton-induced changes in CTE for N-channel CCDs and the effect on star tracker performance,” *IEEE Trans. Nucl. Sci.*, vol. 47, no. 6 III, pp. 2460–2465, 2000.
- [63] N. Meidinger, B. Schmalhofer, and L. Struder, “Alpha particle, proton and X-ray damage in fully depleted pn-junction CCD detectors for X-ray imaging and spectroscopy,” *IEEE Trans. Nucl. Sci.*, vol. 45, no. 6, pp. 2849–2856, 1998.

- [64] A. Holmes-Siedle and S. J. Watts, “Radiation effects in space, nuclear power, and accelerators: impact on optics and light sensors,” *Adv. Photonics Sp. A Crit. Rev.*, vol. 10288, no. July 1997, p. 1028803, 1997.
- [65] K. Mori *et al.*, “Proton radiation damage experiment on P-Channel CCD for an X-ray CCD camera onboard the ASTRO-H satellite,” *Nucl. Instruments Methods Phys. Res. Sect. A Accel. Spectrometers, Detect. Assoc. Equip.*, vol. 731, pp. 160–165, 2013.
- [66] K. K. Nobukawa *et al.*, “Use of a charge-injection technique to improve performance of the Soft X-ray Imager aboard ASTRO-H,” *Nucl. Instruments Methods Phys. Res. Sect. A Accel. Spectrometers, Detect. Assoc. Equip.*, vol. 765, pp. 269–274, Nov. 2014.
- [67] L. K. Harding *et al.*, “Technology advancement of the CCD201-20 EMCCD for the WFIRST coronagraph instrument: sensor characterization and radiation damage,” *J. Astron. Telesc. Instruments, Syst.*, vol. 2, no. 1, p. 011007, Dec. 2015.
- [68] G. R. Hopkinson and A. Mohammadzadeh, “CCD Radiation Testing at Low Temperatures Using a Laboratory Alpha Particle Source,” *IEEE Trans. Nucl. Sci.*, vol. 53, no. 6, pp. 3758–3763, Dec. 2006.
- [69] C. Tivarus and W. C. McColgin, “Dark Current Spectroscopy of Irradiated CCD Image Sensors,” *IEEE Trans. Nucl. Sci.*, vol. 55, no. 3, pp. 1719–1724, Jun. 2008.
- [70] J. Gow, N. J. Murray, A. D. Holland, D. Burt, and P. Pool, “A comparative study of proton radiation damage in p- and n-channel CCDs,” *Proc. SPIE*, no.

September 2009, pp. 74350F-74350F, 2009.

- [71] G. R. Hopkinson, “Proton damage effects on p-channel CCDs,” *IEEE Trans. Nucl. Sci.*, vol. 46, no. 6 PART 1, pp. 1790–1796, 1999.
- [72] J. Ohta, *Smart CMOS Image Sensors and Applications*. CRC Press, 2017.
- [73] J. Manin, S. A. Skeen, and L. M. Pickett, “Performance comparison of state-of-the-art high-speed video cameras for scientific applications,” *Opt. Eng.*, vol. 57, no. 12, p. 1, 2018.
- [74] L. Zhang, Y. Jin, L. Lin, J. Li, and Y. Du, “The comparison of CCD and CMOS image sensors,” *2008 Int. Conf. Opt. Instruments Technol.*, 2008.
- [75] X. Shou-long, Z. Shu-liang, and H. You-jun, “ γ -ray Detection Using Commercial Off-The-Shelf CMOS and CCD Image Sensors,” *IEEE Sens. J.*, pp. 1–1, 2017.
- [76] E. Cruz-Zaragoza and I. P. López, “CMOS sensor as charged particles and ionizing radiation detector,” *J. Phys. Conf. Ser.*, vol. 582, no. 1, p. 012047, Jan. 2015.
- [77] F. A. Bessia *et al.*, “COTS CMOS active pixel sensors damage after alpha, thermal neutron, and gamma irradiation,” in *2016 Argentine Conference of Micro-Nanoelectronics, Technology and Applications (CAMTA)*, 2016, pp. 22–26.

3 Methods

3 METHODS	42
3.1 Equipment.....	43
3.1.1 <i>Radioactive sources</i>	43
3.1.2 <i>Detector information</i>	47
3.1.3 <i>CCD software</i>	52
3.1.4 <i>Post-processing software</i>	54
3.2 Modelling methods	55
3.2.1 <i>CCD structure</i>	55
3.2.2 <i>SRIM: α radiation</i>	57
3.2.3 <i>CASINO: β^- radiation</i>	58
3.3 Experimental methods	59
3.3.1 <i>Standard experimental setup</i>	60
3.3.2 <i>Post-processing techniques</i>	61
3.3.3 <i>Experiments with β^- radiation</i>	63
3.3.4 <i>Experiments with α radiation</i>	65
3.3.5 <i>Experiments with neutron radiation</i>	66
3.3.6 <i>Noise investigation</i>	68
3.4 References.....	73

This chapter consists of three main sections. The first describes the equipment and software used for detecting radiation with CCDs, including descriptions of the radioactive sources used. The second part details the modelling methods, introducing the Monte Carlo software used and outlining the dimensions and materials used in the models. The final part of this chapter describes the basic

experimental setup and lists the specific setups and methods for each experiment performed.

3.1 Equipment

3.1.1 Radioactive sources

A variety of sources of radiation were used over the course of this research. This consisted of a ^{210}Po α -particle source, ^{60}Co and ^{137}Cs β -/ γ sources, and a ^{252}Cf neutron source. These sources are described in sections 3.1.1.1 - 3.1.1.3.

3.1.1.1 Alpha-particle source

A ^{210}Po source was used for the experiments involving α radiation. This source was chosen as it is almost a pure α -particle emitter, with nearly 100% production of α particles. Gamma radiation with an energy of 803 keV is produced at a rate of 0.001% [1]. This is beneficial as there is minimal interference from other types of radiation. The α particles produced have a single energy of 5.304 MeV. Therefore, any energy information which can be obtained is from a known, single energy. This isotope decays to ^{206}Pb which is stable, so there are no further decays. The decay scheme is shown in Figure 3.1.

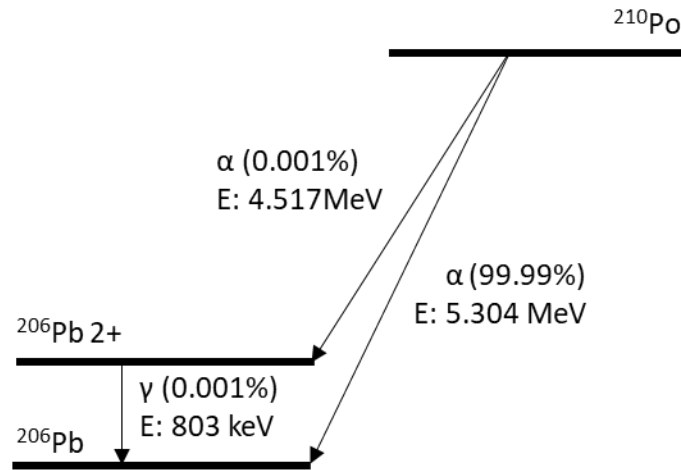


Figure 3.1 Decay scheme showing the decay of ^{210}Po to ^{206}Pb through α emission. The data are from [2].

The polonium source used in this research was supplied on a silver disk, placed inset within a plastic holder at a depth of 3.18 mm, as shown in Figure 3.2. The active diameter is 5 mm. The polonium is covered with a thin layer of acrylic consisting of $100 \mu\text{g cm}^{-2}$, equating to a thickness of $0.45 \mu\text{m}$. The disk is held in place with a plastic retaining ring.

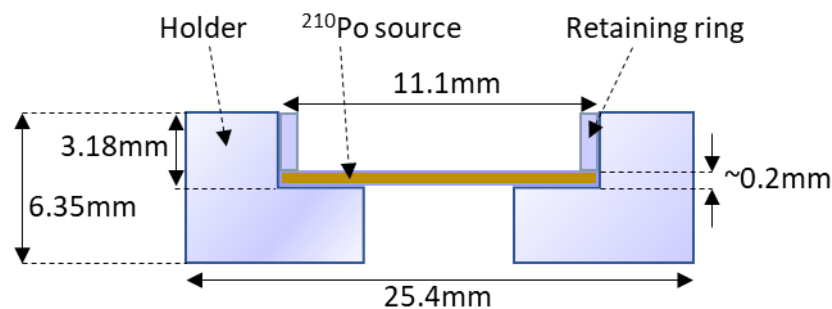


Figure 3.2 Diagram showing the dimensions of the ^{210}Po α -particle source.

When purchased, the activity of the source was stated as 0.4207 kBq on 15/12/2016. However, as ^{210}Po has a half-life ($T_{\frac{1}{2}}$) of 138 days, the activity of the source will have changed significantly over the course of this research. The calculated activity of the source on the date of each measurement taken will be

stated with the relevant experiment. The activities are calculated using Equation (3.1):

$$A_t = A_0 e^{(-\lambda t)} \quad (3.1)$$

where A_0 is the original activity at a given time, A_t is the activity at a time t after the original activity, and λ is the decay constant given by:

$$\lambda = \frac{\ln(2)}{T_{\frac{1}{2}}} \quad (3.2)$$

3.1.1.2 Beta-particle sources

Two β/γ sealed sources have been used to investigate the response of CCDs to β radiation. These are ^{60}Co and ^{137}Cs , and both are supplied on flat, plastic disks. The decay schemes for each of these sources are shown in Figure 3.3 and Figure 3.4. The activity of the ^{60}Co source was 37.95 kBq on 20/04/2006, and the activity of the ^{137}Cs source was 397 kBq on 01/04/2009. Activities are calculated for each experiment using a half-life for ^{60}Co of 5.26 years and for ^{137}Cs of 30.17 years.

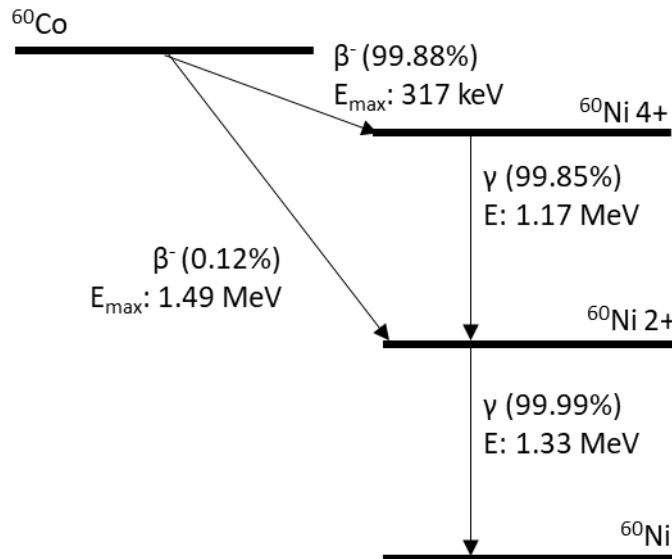


Figure 3.3 Decay scheme showing the decay of ^{60}Co to ^{60}Ni through β^- and γ emission. The data are from [3].

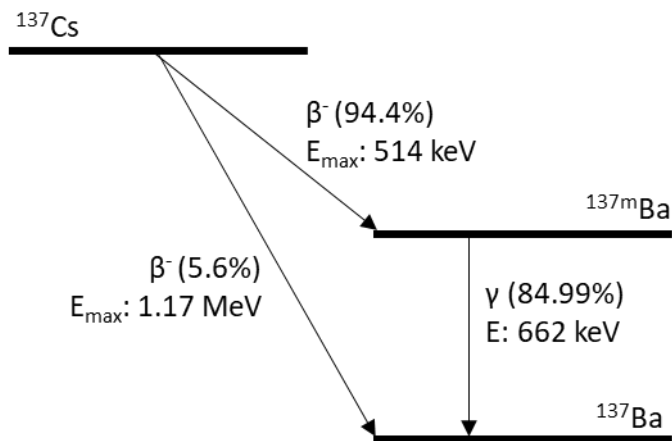


Figure 3.4 Decay scheme showing the decay of ^{137}Cs to ^{137}Ba through β^- and γ emission. The data are from [3].

3.1.1.3 Neutron source

For the neutron experiments, a ^{252}Cf source was used. Primarily, ^{252}Cf decays by α -emission, however 3.092% of its decay is through spontaneous fission. This spontaneous fission produces an average of 3.75 neutrons per fission [4], each with an average energy of 2.1 MeV [5].

The source is encapsulated in a double layer of stainless steel. This is fitted to the end of a 45 cm stainless steel rod, housed inside a stainless steel tank which is filled with water to moderate the neutrons. The source may be positioned centrally within the tank for maximum moderation (the source is secured), or it may be moved towards one side of the tank to reduce moderation for measurements (the source is exposed). The container will prevent any α -particle interactions, so only the neutrons and γ rays from the spontaneous fission will be detectable.

The activity of the source was 74.84 MBq on 19/02/2014. The half-life of the source is 2.65 years and as all of the neutron research was performed mid-late 2019, the activity can be calculated to be approximately 17.50 MBq for this research, using a date of 10/09/2019 for which the most important dataset was collected.

3.1.2 Detector information

3.1.2.1 CCD details

The CCD devices used in this research are modified UltraStar cameras from Starlight Xpress [6], modified by BIC Technology Ltd. They consist of the CCD on a backing board, attached to a PCB (printed circuit board) containing the associated electronics. The glass covering is removed, and a double layer of aluminised Mylar film is added to prevent light from interacting within the CCD. A single layer of film was found to be insufficient at completely blocking the light. A Sony ICX825AL interline, front-illuminated CCD is used consisting of 1392×1040 pixels with a pixel size of $6.45 \times 6.45 \mu\text{m}$. This gives a total imaging area of $6.71 \times 8.98 \text{ mm}$. One pixel has a capacity of 16,000 electrons and the gain of the device is 0.3 electrons/ADU. The CCD and the entire device are shown in Figure 3.5.

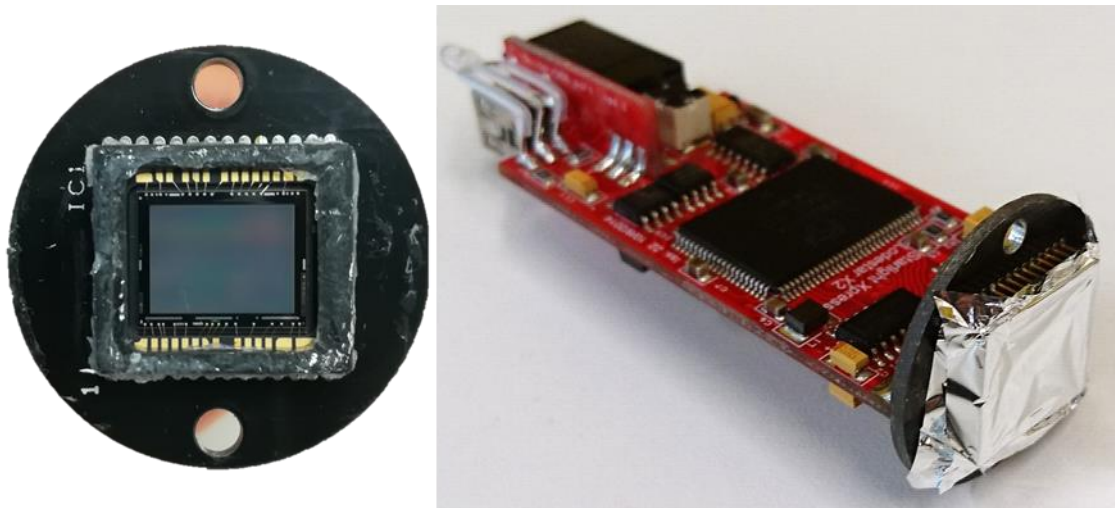


Figure 3.5 Left: CCD imaging area, with the CCD attached to the backing board. Right: The radiation detection device, with the board attached to the PCB and the imaging area covered with the Mylar film.

There are 12 pins connecting the electronics to the CCD. These can be seen diagrammatically in Figure 3.6. There are four vertical register transfer clocks, V_{1-4} ; two horizontal register transfer clocks, H_{1-2} ; a substrate clock, SUB; an output, O/P; a reset gate clock, R_G ; a supply voltage, V_{dd} ; and two ground pins, GND.

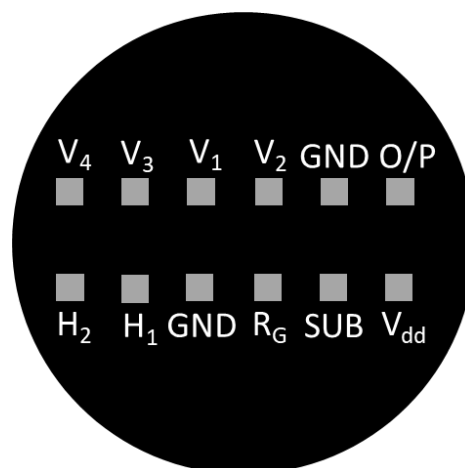


Figure 3.6 Simplified diagram showing the CCD connections through the backing board.

For this research, a front-illuminated device was chosen. In part, this is due to the cost and availability of these devices. More significantly, back-illuminated devices

are commonly thinned to values of 10-15 μm [7], [8]. This is thinner than the range of the α particles in these devices as will be seen in Section 4.1.1, and so not all the radiation from the α -particle would be detected. The trade-off for losing some of the energy in the gate structure is worthwhile to ensure all of the remaining energy is detected in the CCD. In addition to this, blooming will only occur in front-illuminated devices as described in Section 2.2.3.1, and this was an important phenomenon to be investigated during this research.

The CCD software instructs the CCDs to 'bin' the pixels in a 2×2 area, giving the readout of four pixels summed together as one. Hereafter, "one pixel" will refer to one of these 2×2 pixel bins, such that the total image size is 694×520 pixels and one pixel is $12.9 \times 12.9 \mu\text{m}$. The capacity of the bin is $>23,000$ electrons.

This CCD comes with anti-blooming capabilities; however, this is set to a minimum in this research so that blooms are able to occur. Pixel binning also increases the likelihood of blooming as the charge carriers from multiple pixels are summed, increasing the chances of exceeding the capacity and overflowing [9].

3.1.2.2 Device configuration

Different methods of mounting the CCD onto the electronics were tested. Initially, the CCD was connected to the electronics by long, flexible wires. However, it was found that the wires were very sensitive to touch or motion and caused an unstable increase in image noise. Shorter, sturdier wires were considered for the next iteration, including a casing designed to minimise external electrical noise which may have been having an impact on the amount of noise produced in the images. The wire replacement reduced the fluctuations in the noise, though it did not completely stabilise it. However, the casing was found to have no effect, most likely

because it did not encase the CCD itself which would be the part most likely to be affected by electrical interference. After this, new CCDs of the same type were used, modified to remove the wires altogether such that the backing board for the CCD was soldered directly to the PCB. This removed the instabilities caused by the wires and made the device smaller in size. The iterations of the device can be seen in Figure 3.7-Figure 3.9.

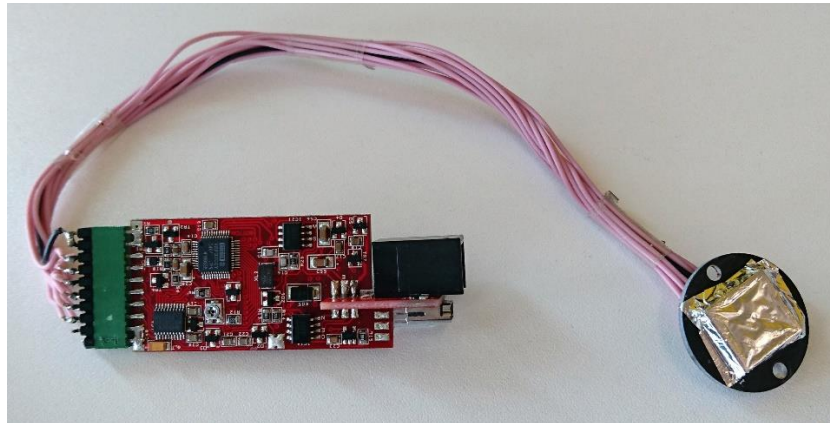


Figure 3.7 Original device configuration with long wires connecting the CCD to the electronics.

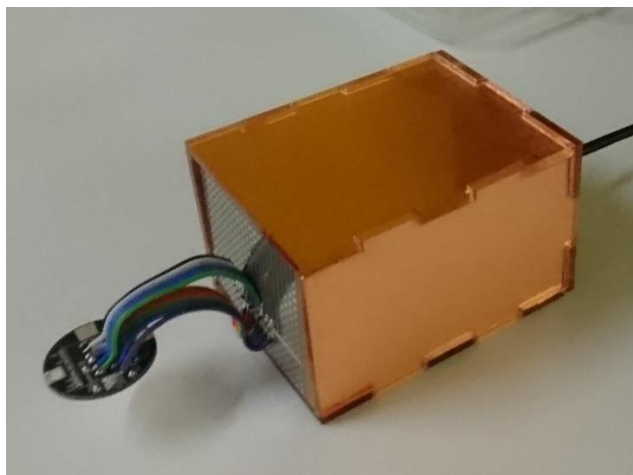


Figure 3.8 Temporary device configuration intended to reduce noise, with a plastic box coated in a copper film, and the long wires replaced with shorter, sturdier wires.

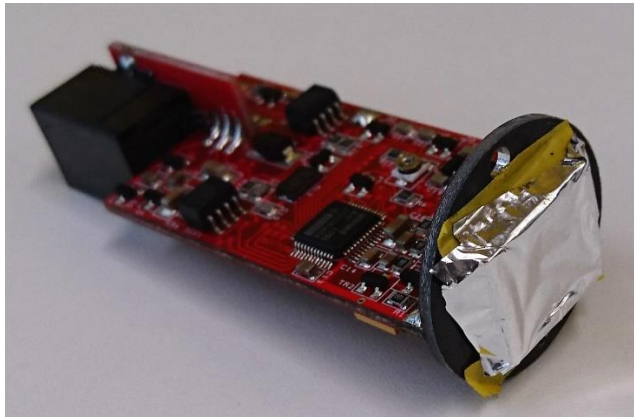


Figure 3.9 Final device configuration used in this research.

For experiments requiring additional cooling modifications, a copper heat pipe was attached to the CCD by the author to draw heat away. It passes between the sensor and the backing board, and bends down to pass along the side of the PCB. As the CCD heats up during use, the liquid in the wick of the section of heat pipe in contact with the CCD is evaporated. The vapour then passes through the heat pipe to the other, cooler, end where the vapour is condensed back into a liquid. This transfers the heat through the pipe, demonstrated in Figure 3.10. If the cold end is cooled externally with a fan or heat sink, this process is more efficient. The heat pipe used was a Wakefield-Vette heat pipe of size $7 \times 100 \times 1$ mm. The maximum heat transfer is 12W, through a powder sintered copper wick.

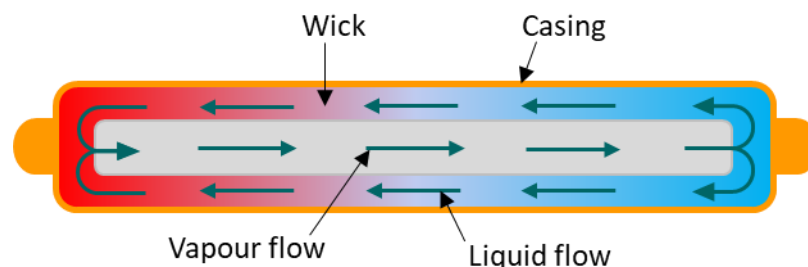


Figure 3.10 Diagram detailing the operation of a heat pipe, with the heat source indicated by the red colouring on the left, where evaporation occurs, and the cooler side indicated by the blue colouring, where the condensation occurs.

Opposite the cold end of the heat pipe a fan is attached to aid heat transfer to the air from the pipe. The fan used was a Sunon MagLev motor fan, 25 × 25 × 10 mm in size with 5V operation. This enables it to be powered potentially through the same USB cable that the CCD uses. The device with the cooling equipment in place is shown in Figure 3.11.

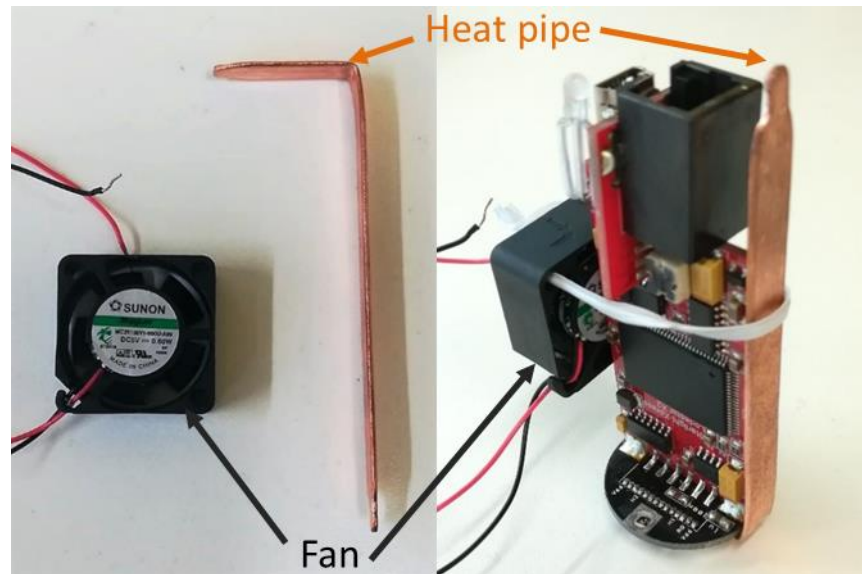


Figure 3.11 Left: The fan and the heat pipe developed in and used in this research. Right: The fan and the heat pipe in the primary positions used on the device.

3.1.3 CCD software

The software, QubiX Radiation Detector, was provided by BIC Technology Ltd. specifically for use with this CCD system. The software reads in the data from the CCD and removes any pixels below a set intensity threshold. A minimum threshold must be set for the software to run, this varies between CCDs depending on the inherent noise in the system.

When the software is loaded, the user is prompted to set up the exposure to be taken, as can be seen in Figure 3.12. The three main settings are threshold, camera gain, and camera offset. The camera gain and offset were kept constant at the values

shown in Figure 3.12. The gain is set high to ensure the maximum number of signals can be seen over the threshold level. The offset was found to not have a noticeable effect on the images produced and so was left at the default setting of 10. The threshold varied depending on the CCD used, the level of damage, and the temperature. The values used varied between 50 and 100, but for the majority of results taken, a threshold of 70 was used for consistency.

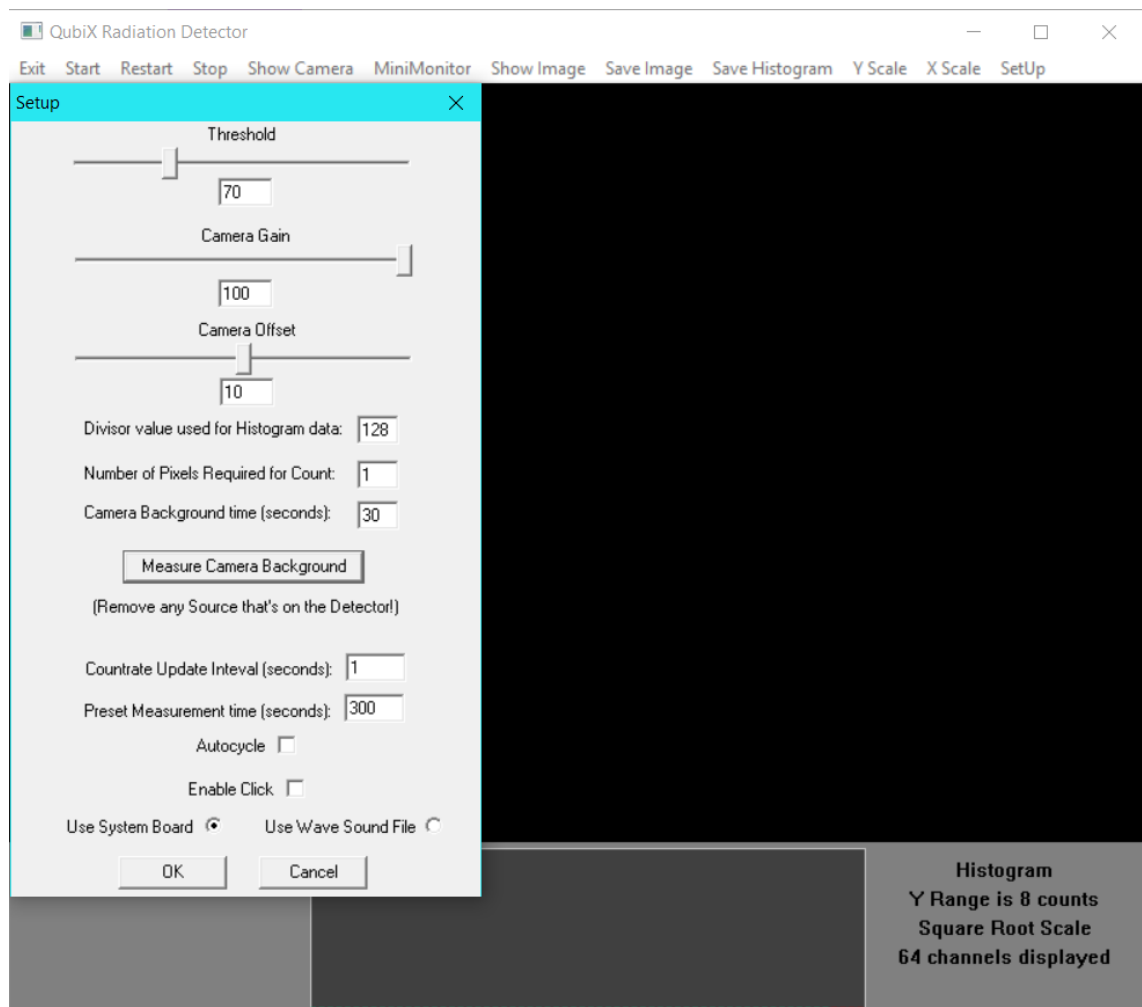


Figure 3.12 Graphical user interface (GUI) for the QubiX Radiation Detector software used with the CCD in this work.

To obtain an image, a background image must first be taken. This is an exposure of the CCD in darkness, with no source of radiation present. This measurement therefore records the dark current within the CCD. Usually, a 30 s background

Characteristic responses of a COTS CCD to α , β -, and neutron-induced triton radiations and strategies to reduce noise

measurement was taken. These background signals were then subtracted from the data when the subsequent desired image is taken. This removes the noise inherent to the CCD. An example of a background image can be seen in Figure 3.13.

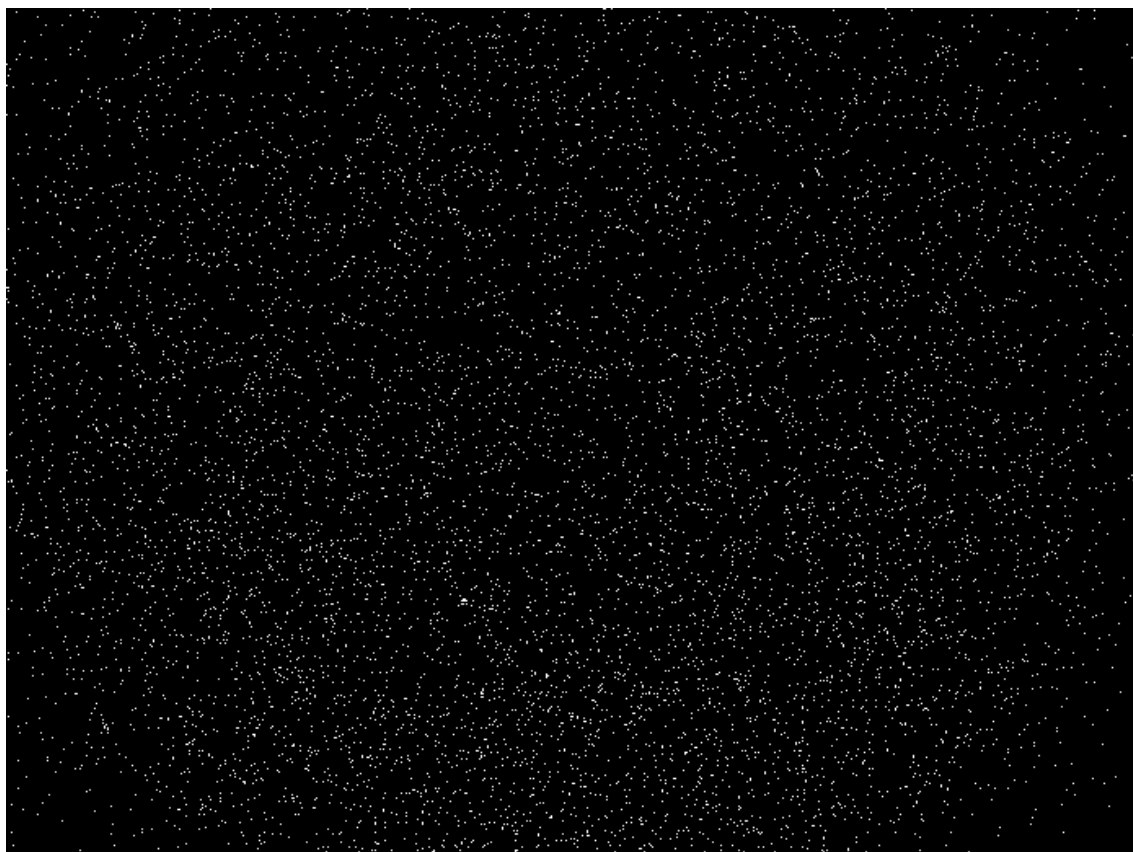


Figure 3.13 Example of a 30-s background measurement taken with one of the CCDs in this work. The pixels have been highlighted to have the maximum intensity of 255 ADU (Analogue-to-Digital Units).

3.1.4 Post-processing software

The images produced by the CCD were processed further using python™ 3.6, through Spyder (Scientific Python Development Environment) 3.2.8 as part of the Anaconda Navigator. This processing fulfilled several useful purposes. These include: finding the properties of the clusters, including size, shape and intensity; identifying different types of signals based on these properties; counting the

numbers of clusters; and performing any image modifications required. Different functions were created to perform each of these tasks, given in Appendix A.

3.2 Modelling methods

The interactions of α and β^- radiation with the CCDs were modelled using Monte Carlo simulations. Monte Carlo particle simulations use random numbers to simulate paths that particles will take when travelling through a material. Experimental information about the particle and the material are used to determine the probabilities of different interactions occurring, and the random numbers are used to determine which interactions occur for each particle in the simulation. Two pieces of modelling software were used in this research: SRIM (the Stopping and Range of Ions in Matter) version SRIM-2013.00 [10] to simulate α radiation, and CASINO (Monte Carlo Simulation of Electron Trajectory in Solids) v3.3.0.4 [11] to simulate β^- radiation.

3.2.1 CCD structure

To simulate the interaction of radiation with CCDs, the structure of the CCD must be modelled. Manufacturers do not typically share the specific layer depth information, and so these details were not known for the Sony ICX825AL CCDs used. Estimates were therefore made using the available literature on similar devices. Two sets of structures were devised, using thin layers that are typically used, and using thicker layers to perform a more conservative estimation.

The thin values were taken from a scanning electron microscopy image of a CCD [12], [13], which seem to be typical based on information from other sources [14], [15]. Guidance from several sources were used to determine upper estimates for the thicknesses of the various layers [16]–[18]. For most of the simulations, the thicker

values were used to give conservative estimates, however these were also compared with thinner values in some cases. The total thicknesses of the two gate structures are $0.69\ \mu\text{m}$ and $2.00\ \mu\text{m}$ respectively. For a front-illuminated CCD, the active region can range from $10\ \mu\text{m}$ up to $100\text{s of } \mu\text{m}$, with many modern devices having thicknesses of at least $60\ \mu\text{m}$ [14], [19], [20]. Therefore, this value was used in the estimation.

For α -particle simulations in particular, it is important that the entire source-to-CCD distance is modelled due to the high LET of α -particles. Information pertaining to the ^{210}Po source was therefore used, including the air gap necessitated by the shape of the source, and the thin plastic covering, as detailed in Section 3.1.1.1. In addition to this, the thickness of the aluminised Mylar foil used was measured. The aluminium layers were measured using x-ray diffraction to give a thickness of $(0.61 \pm 0.04)\ \mu\text{m}$ in total. A section of foil of dimensions $(5.90 \pm 0.05) \times (6.00 \pm 0.05)\ \text{cm}$ was then weighed using a precision balance, giving a mass of $(17.59 \pm 0.01)\ \text{mg}$. Given the density of aluminium of $2.70\ \text{g cm}^{-3}$, the mass attributed to the aluminium was $(5.83 \pm 0.39)\ \text{mg}$. The weight of the Mylar is therefore $(11.76 \pm 0.79)\ \text{mg}$. Using the density of Mylar to be $1.39\ \text{g cm}^{-3}$, the thickness of the Mylar is calculated to be $(2.39 \pm 0.16)\ \mu\text{m}$. This gives a total thickness of $(3.00 \pm 0.40)\ \mu\text{m}$ per layer of the film. The total layout for the simulations for the full source-to-CCD distance is given in Table 3.1.

Table 3.1 Estimated and measured layers of the total source-to-CCD distance for the ^{210}Po source. The two values for each layer in the gate structure represent the thick (left) and thin (right) structures used.

Layer		Thicknesses
Plastic on source		0.45 μm
Air to CCD		3.18 mm
Mylar foil (two layers)	Aluminium	1.2 μm
	Mylar	4.78 μm
Air from Mylar to CCD		1 mm
CCD gate structure	Silicon dioxide	1 μm / 0.36 μm
	Polysilicon	1 μm / 0.33 μm
Active region (silicon)		60 μm
Substrate (silicon)		>60 μm

3.2.2 SRIM: α radiation

The interaction of α particles with the CCD was modelled using SRIM [10]. This is a Monte Carlo application that simulates ions passing through layers of materials. Helium ions were simulated with an energy of 5.304 MeV to represent the α particles from the ^{210}Po source. For each simulation, 10,000 ions were used. The ‘ion calculation and quick calculation of damage’ option was used to determine the range of the α particles and their energy loss prior to interaction with the CCD. This involves damage calculations based on the theory proposed initially by Kinchin and

Pease [21]. Full damage calculations were not required for these calculations, and the approximations made using the quick calculations allow for significantly faster simulations [22]. Full damage calculations were also performed to investigate the damage induced by the α radiation, which use the full damage cascades generated per ion.

High- and low-energy α particles were also simulated to find the range they would be expected to have into the active layer of the CCD. This was to determine if a full range of α -particle energies from a given isotope might be detectable with this device. Energies from real α -emitting isotopes which could potentially be detected with this device were used. For high-energy particles, a value of 8.748 MeV was used to represent the decay of ^{212}Po . For low energies, ^{147}Sm was considered, producing α particles of 2.232 MeV. These simulations were performed both in direct contact with the Mylar film, and with the plastic covering and air gap associated with the ^{210}Po source, to account for different detection situations.

3.2.3 CASINO: β^- radiation

To simulate the interaction of β^- particles with CCDs, CASINO was used. The 3D version (3.2.0.4) [11] was used to simulate electrons (β^- particles) scattering through multiple pixels. For these simulations it was determined that the Mylar layers and gate structure within the CCD did not impact the energy loss or scattering of the β^- particles significantly, so only the active layer and a section of substrate were simulated, both consisting of silicon. A 10×10 array of pixels was modelled, seen in Figure 3.14, to determine how many pixels the electrons would scatter through.

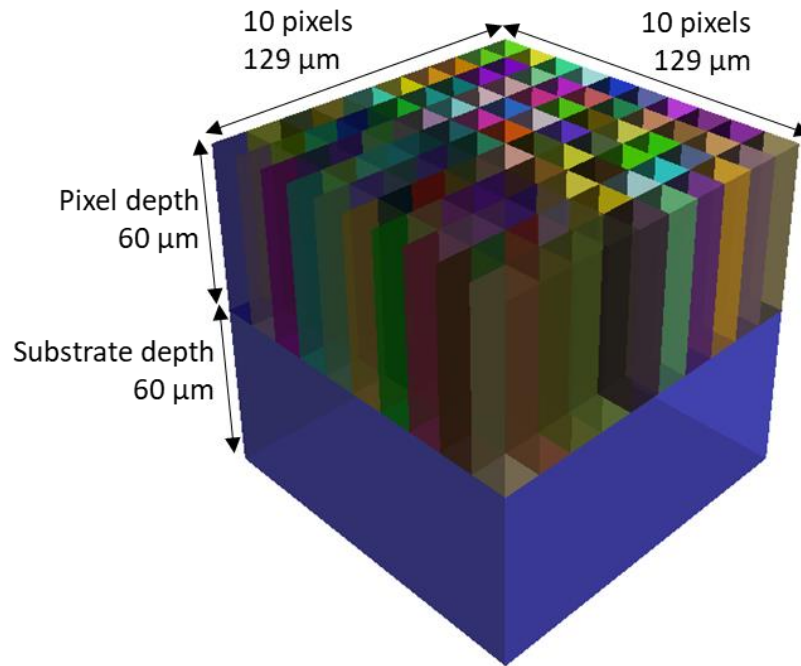


Figure 3.14 The regions used in the CASINO simulation to represent 100 CCD pixels (multi-coloured) and a section of the substrate beneath (blue). Both materials are silicon.

The two sources that were used experimentally, ^{60}Co and ^{137}Cs , were simulated to investigate the scattering of the radiations from them. The maximum energies (E_{max}) for the most common β^- -particle emissions of each source were simulated. Therefore, an energy of 317 keV was used to represent ^{60}Co β^- particles, and 514 keV for ^{137}Cs , from the decay schemes shown in Figure 3.3 and Figure 3.4. In each case, 10,000 particles were simulated.

3.3 Experimental methods

For most of the experiments performed with the α and β^- sources, a standard experimental setup was used, as detailed in Section 3.3.1. Any modifications or different setups used will be discussed in the relevant sections describing the specific experiments performed that involved them. The setup involving the neutron source was different and is described alongside the experimental methods in section 3.3.5.

3.3.1 Standard experimental setup

For most experiments, the following setup was used. Typically, the CCD with the Mylar-film covering was placed in contact with the source and attached to a laptop running the CCD software via a USB cable, as shown in Figure 3.15.

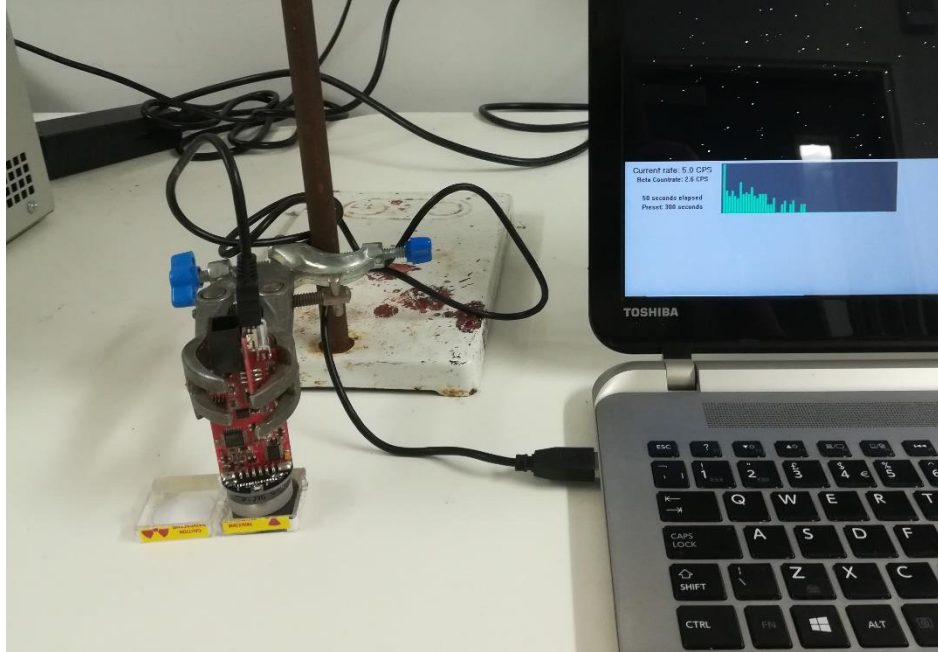


Figure 3.15 The most-commonly used experimental setup, showing the CCD in use with the ^{210}Po source.

As discussed in Chapter 3, the dark current increases with increasing temperature of the device. As the CCD heats up during use, the CCD was operated for 5 minutes with no source present to allow it to reach a stable temperature. A 30-s background measurement was then taken to account for the increased dark current due to the higher temperature of the CCD during operation. This is only repeated when the CCD has had the opportunity to cool down between uses.

Exposure times were varied depending on the activity of the source used and the purpose of the image being produced, but generally the longest exposures were such that very few of the clusters produced overlapped. Overlapping clusters would be

analysed as one cluster, giving incorrect information about cluster sizes and pixel intensities when analysed using python™.

To minimise radiation dose to the user from each of the sources used, a distance of at least 30 cm was maintained between the user and the source during normal operation. Tongs were used to move and position the source, and when using the ^{210}Po source gloves were worn. The dose received was monitored using a dosimeter that was worn at all times in the sealed sources laboratory at Lancaster University. A Geiger counter was also used to ensure there was no residual contamination before and after experiments were performed.

3.3.2 Post-processing techniques

The clusters that arise in response to interactions in the CCDs used in this research for different types of radiation vary in shape. The α particles produce clusters that are approximately symmetrical, either round or in vertical streaks. The β -radiation clusters are much more randomly oriented and may form curved tracks. Using python™, a box may be placed around the clusters to determine these differences. This bounding box is in contact with the cluster on all four sides, such that the box is the smallest that can fit around the cluster. Consider Figure 3.16: here, the box surrounding both the α particle streak and cluster are over 50% occupied, due to the symmetry of the clusters. In contrast, the β track only fills a small area of the box. These are the properties used to identify the different types of radiation, along with the presence of streaks, the total number of pixels in the cluster, and the intensity of the brightest pixel in the cluster, as detailed in Chapter 5.

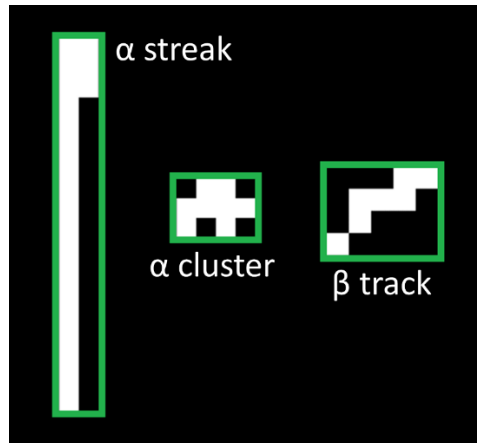


Figure 3.16 Typical examples of a streak and a cluster caused by α radiation, and a track caused by β radiation. Each has been surrounded with a bounding box (in green) used to obtain information about the shapes of these signals. The pixels have been highlighted to the maximum intensity.

Some of the streaks created by interactions in the CCD by α particles have single-pixel gaps in them. This is because the streaks are of a low intensity compared to the site of the α -particle interaction, so some of the pixels may have dropped below the threshold of the software. To ensure a more consistent analysis of streaks exhibiting these effects, these were joined up during image processing, as the analysis techniques used would otherwise identify the streak incorrectly, as two separate clusters. If a minimum of three pixels were connected vertically with a single-pixel gap between two of them, then the missing pixel has had its value changed to be that of the software threshold. This means intensity information will not be completely accurate, however it is an improvement over counting the singular, split streak as two separate streaks. As the missing pixel is surrounded by pixels over the threshold, it is unlikely to have dropped significantly below this value, and hence by setting the intensity to be the threshold value it will be as accurate as possible.

An example of a split streak being filled is shown in Figure 3.17. The image processing works with the intensity value of the pixel and so removes the added colours, leaving the final image in monotone shades.

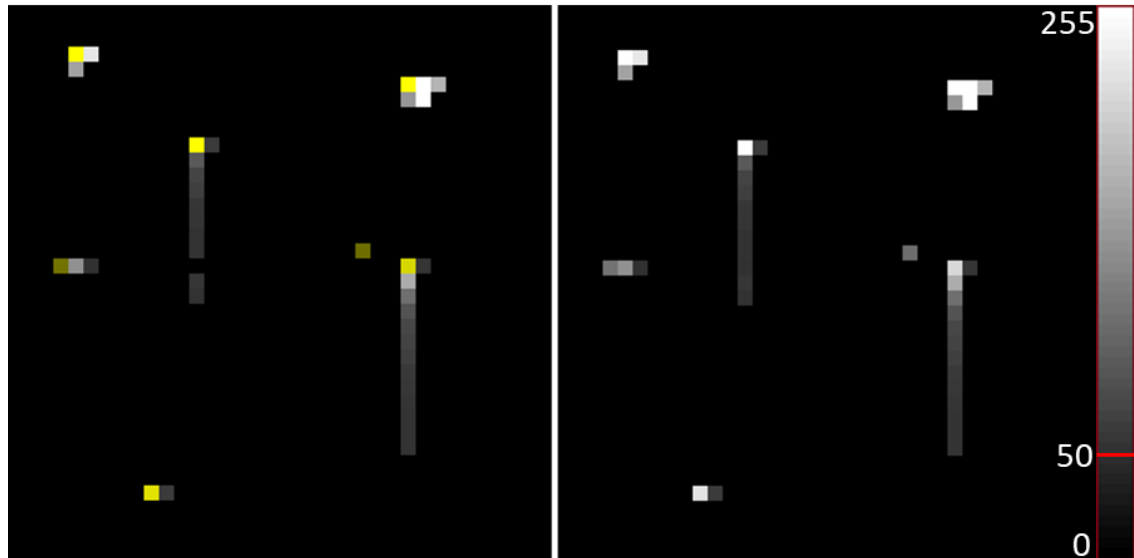


Figure 3.17 Image section showing a split α -induced streak before and after processing. The software threshold is marked in red on the scale.

3.3.3 Experiments with β^- radiation

3.3.3.1 Cluster sizes: comparison with simulation

To compare images produced by the different β^- -particle sources, exposure times were used such that approximately 1000 clusters were accrued in the images. This was to ensure the results are as analogous as possible, by having similar likelihoods of signals (clusters) overlapping. The comparison uses images generated before increased noise levels were noticeable in the CCD. This ensures the clusters are from the radioactive sources rather than noise from damage in the CCD.

For the ^{60}Co source with an activity of 9.32 kBq, an exposure was taken for 5 s. The ^{137}Cs source had an activity of 333 kBq at this time, and an exposure of 1 s was used. The number of counts for each cluster size was normalised to be a percentage of the

total number of counts to ensure comparability between each measurement. For these exposures the CCD was placed with the Mylar film in contact with the radioactive source, as per Figure 3.15, to ensure minimum energy loss.

3.3.3.2 Comparing the responses of β^- and γ radiation

To compare the signals from β^- radiation with those from γ radiation, some aluminium was placed between the CCD and the β^-/γ sources. CASINO simulations were performed to calculate the thickness of aluminium required to block the β^- radiation from the two sources. This was found to 0.423 mm for the ^{60}Co β^- particles, and 0.864 mm for those from ^{137}Cs .

The intensity loss of γ radiation passing through the material was calculated using,

$$I_x = I_0 e^{-\mu_L x}, \quad (3.3)$$

where I_0 is the incident intensity and I is the intensity after passing through a thickness of material x . The linear attenuation coefficient, μ_L , is given by:

$$\mu_L = N\sigma_i, \quad (3.4)$$

where N is the atomic density of the material and σ_i is interaction cross section per atom [23]. The intensity loss was calculated for the two γ rays produced by ^{60}Co and the one γ ray produced by ^{137}Cs , as per Figure 3.3 and Figure 3.4, using equations 3.3 and 3.4. The linear attenuation coefficients used and distances at which the intensities drop to 90% of their incident intensities were calculated and are given in Table 3.2. It was found that the intensity was greater than 90% of its maximum for both sources at a depth of 5 mm into the aluminium.

Table 3.2 Linear mass attenuation coefficients for the γ rays produced by the two sources used, using data from [24], and the distance into aluminium at which they will be at 90% of their original intensities.

Source	γ energy (MeV)	μ (cm^{-1})	x at $I = 0.9I_0$ (cm)
^{60}Co	1.1732	0.154	0.680
	1.3325	0.140	0.753
^{137}Cs	0.6617	0.203	0.519

A piece of aluminium of thickness 4 mm was available and was chosen to be used as it would block all of the β^- radiation from both sources, whilst maintaining a γ -ray intensity of over 90%. For both sources in the covered and uncovered states, 10 images were taken. In each case, the CCD was positioned 1 cm away from the source. Exposures were taken for 55 s for the ^{60}Co source, and 10 s for the ^{137}Cs source. This was to ensure approximately 1000 clusters in each of the images, where the activities of the two sources were 6.5 kBq and 312 kBq, respectively. The same length of time was used for the covered images to investigate the reduction in the number of clusters detected in that time period.

3.3.4 Experiments with α radiation

To characterise the signals from α radiation and investigate the potential of using CCDs to perform spectroscopy of this radiation, many images were taken over the course of the research, using the basic setup described in Section 3.3.1. Exposures were varied from 30 s to 5 minutes, depending on the activity of the ^{210}Po source at

the time of a particular measurement. Final analyses on streak and cluster size were performed using only exposures taken with the CCD in its final configuration, as per Figure 3.9, and with the cooling equipment in place to minimise noise. In total, 185 images were used for these analyses, and to determine the intensities of the pixels in the α clusters and streaks.

Additional experiments were performed with the ^{210}Po source to investigate noise-related problems and solutions, and these will be described separately in Section 3.3.6.

3.3.5 Experiments with neutron radiation

To investigate the ability of the CCD to detect neutron radiation, lithium crystals were used. The interaction of neutrons with ^6Li to produce α particles is,



where the α particle produced has an energy of 2.05 MeV, and the triton (T^+) has an energy of 2.75 MeV [25]. These particles may then be detected by the CCD as for the other measurements described earlier.

A 4×4 grid of crystals containing lithium was used to cover the CCD, with each crystal having dimensions of $3.2 \times 3.2 \times 0.9$ mm. This covered a total area of 12.8×12.8 mm, completely covering the CCD imaging area. The crystals used are Harshaw TLD-600 (thermoluminescent dosimeters), consisting of $\text{LiF}(\text{Mg},\text{Ti})$, which is enriched with ^6Li to 95.62% [26]. This isotope has a (n, α) cross-section of approximately 0.2 barns at a neutron energy of 2 MeV, compared with the more abundant ^7Li which does not readily interact with neutrons to produce α particles

[27], [28]. The lithium grid was placed outside the Mylar film to allow it to be used on a removable cap, to alternate between α/β - and neutron detection.

The CCD was placed parallel to the tank at the point at which maximum neutron emission occurs, marked by the 'X' on the tank, shown in Figure 3.18. A 5-metre long cable was used to connect the CCD to the laptop, allowing it to be used on the opposite side of the tank, ensuring minimal dose was received when operating the laptop. Once the equipment was in place, a background measurement was taken. This will include some signals from the γ radiation which is emitted from the neutron source. Barriers were then placed to restrict access to the exposed side of the source as is normal procedure when using this source. The source was exposed and the measurements taken over an hour, with three 10-minute exposures and one 30-minute exposure. Neutron dosimetry badges were worn in addition to γ badges to monitor the dose received, and a neutron area survey monitor was used in the laboratory to confirm when the source was exposed and secured.

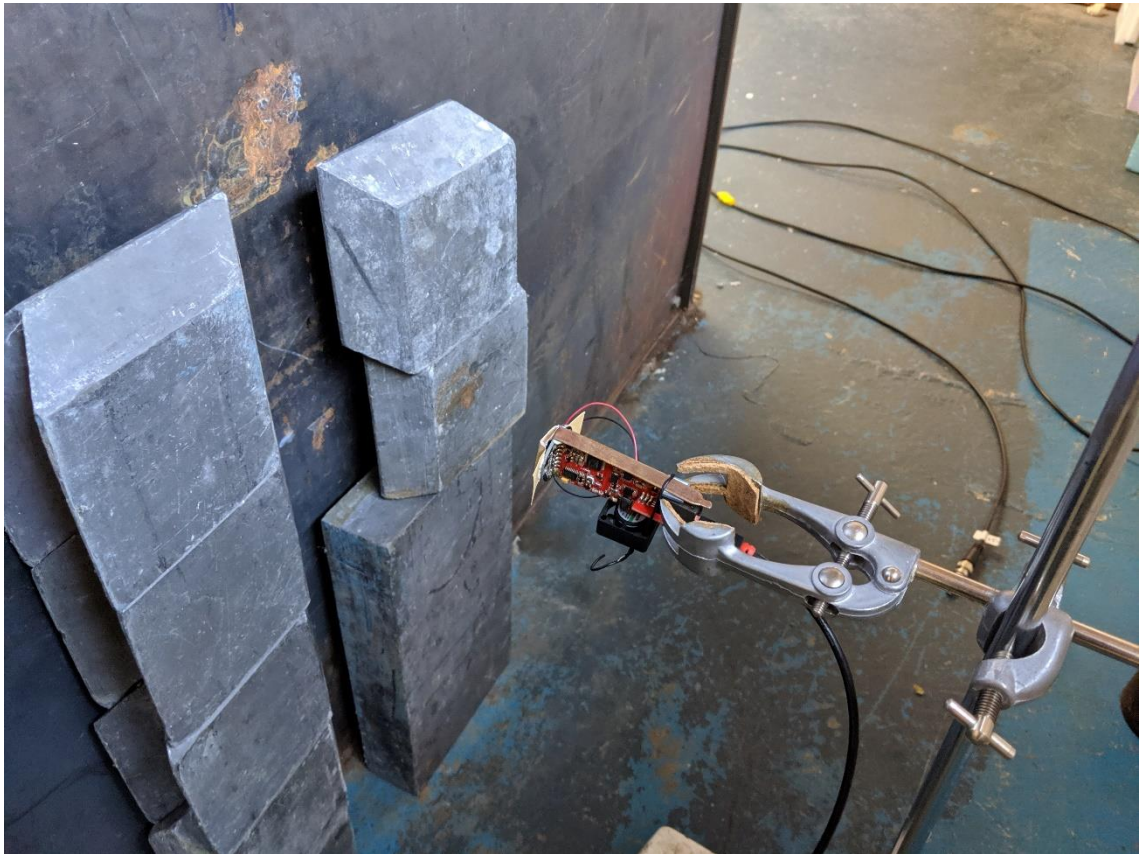


Figure 3.18 Experimental setup in the neutron lab., with the CCD held in place facing the neutron tank.

3.3.6 Noise investigation

Over continued use of the CCD, an increase in noise was observed in the images produced. This noise consists of bright pixels where no interactions with radiation have occurred during the current exposure. At low levels of noise this does not cause a significant problem, however a high level of noise can impact the accuracy of α -particle detection. As the additional noise was likely to be caused by damage in the CCD, the effects of α and β^- radiation were investigated.

To investigate the damage caused by α radiation, half of the CCD imaging area was covered with a 0.5-mm thick piece of card, sufficiently thick to stop the α particles from the ^{210}Po source. This was attached to the CCD underneath the Mylar film to ensure the area covered was kept constant. This allowed half of the CCD to be

Characteristic responses of a COTS CCD to α , β^- , and neutron-induced triton radiations and strategies to reduce noise

exposed whilst the other half would not experience any interactions with α radiation, so the differences could be compared directly.

A background image was taken, and the CCD was then exposed to the ^{210}Po source for 5 hours, with an activity of 28 Bq. After each hour, the source was removed and an additional background image was taken. Sections of 250×520 pixels from the covered and uncovered sides of each image were taken and the number of white pixels counted. The exposures occurred with the CCD biased (in operation) to identify whether the noise was due to the source or whether it built up over general use of the CCD.

To test the ^{137}Cs source for the effects of β/γ radiation on the noise produced, the background over the whole CCD imaging area was compared over time. Exposures were taken for 9 hours total over 2 days with the CCD biased, with background measurements taken at 30 mins, 1.5 hours, and 4 hours on the first day, with an additional 5-hour exposure on the second day. To confirm the effects of this source with the CCD, the same experiment was repeated with the CCD unbiased. No attempt was made to repair damage between these two experiments with the ^{137}Cs source, so any damage should be cumulative. The activity of the source during these measurements was approximately 320 kBq.

3.3.6.1 Annealing

Annealing is a method of heating a radiation-damaged object over a period of time to allow displaced ions to recombine with vacancies within the CCD, repairing some of the damage [29]. Annealing was performed at different temperatures and times to find an optimal protocol for repairing damage within the CCD, whilst also being practical for the user to implement. The prior art suggests temperatures for

annealing of room temperature up to 350°C or higher, across different situations [29]–[34], however only temperatures were considered which would not damage the electronics or cause the solder to melt, so that the device did not need to be disassembled. Lower temperatures were initially considered for convenience. The solder was determined to melt at 120°C, so the highest temperature used was 100°C to ensure an appropriate buffer with the melting point.

Table 3.3 The oven temperatures and respective lengths of time tested for annealing.

Temperature (°C)	Time (Hours)
50	4
60	0.5
	24
80	5
	24
100	5
	24

The lower temperatures were found to be ineffective at annealing. Annealing at 80°C for 24 hours reduced the noise by approximately half. Using a temperature of 100°C for 5 hours produced a similar outcome, but using 100°C for 24 hours was found to be adequately effective and was used in this research, as detailed in Chapter 4.

To determine the noise reduction in the annealing process, 10 exposures were taken with no source present for 5 minutes each, both before and after annealing. By

taking images with no source present, all of the clusters in the image can be deemed to be noise beyond that which is removed during the background subtraction. The total number of clusters in each image were counted and averaged over the sets of 8 images.

3.3.6.2 Cooling

Cooling is a common method for reducing noise in scientific CCDs [14], [17]. This technique can be used to minimise the noise caused by the damage during operation, as well as the CCD dark current. Two pieces of equipment were considered for this: a copper heat pipe is used to draw heat away from the CCD, and fan is also used to cool either the heat pipe or the CCD directly. Experiments were performed to compare the effectiveness of four different setups for cooling, as shown in Figure 3.19.

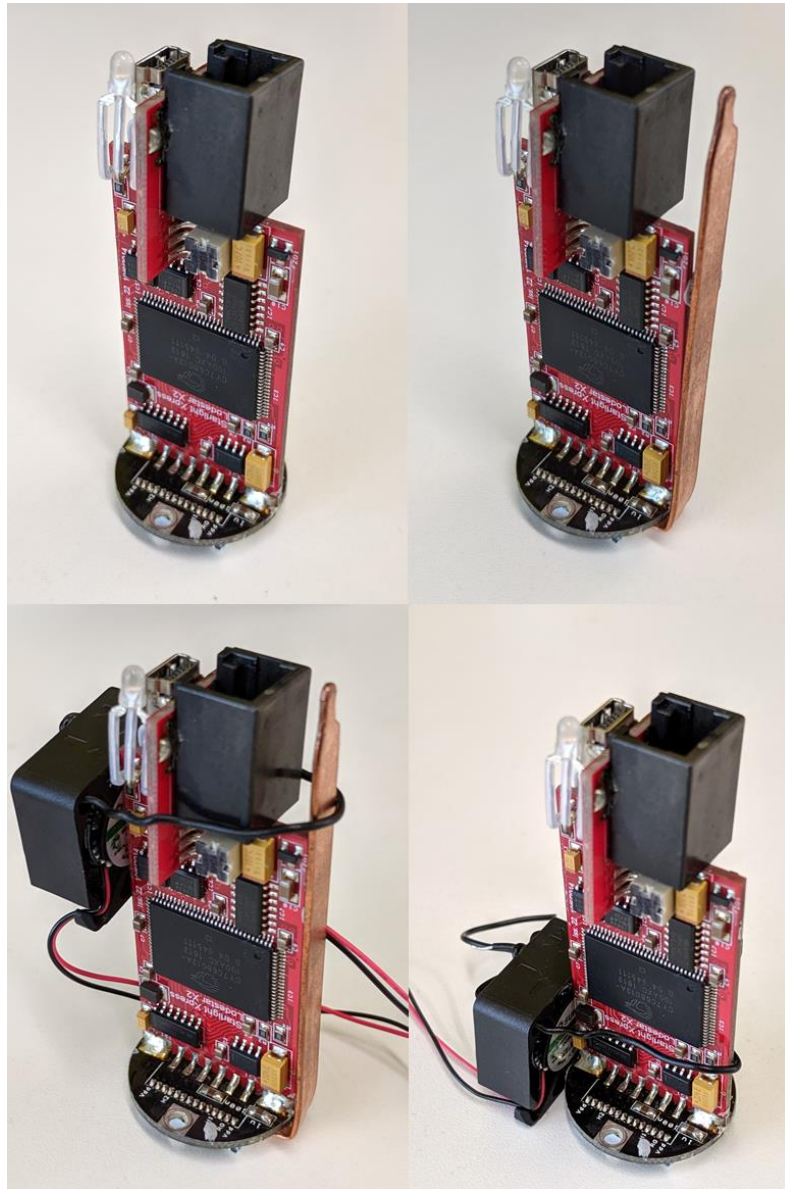


Figure 3.19 Different setups used for cooling. Top left: no cooling. Top right: the heat pipe alone. Bottom left: the heat pipe being cooled by the fan. Bottom right: the fan directly cooling the CCD without the heat pipe.

These exposures were taken when the CCD was exhibiting a lot of noise from damage, to highlight the effects of the cooling. Exposures were taken for 3 minutes with no source present, and the average number of clusters were counted over 10 exposures for each cooling technique.

3.3.6.3 Image processing

Image processing techniques were also developed to remove noise, a function which can be performed before further analysis to allow for more accurate results. As the noise is all low-intensity in comparison to the α radiation, and typically occurs in single pixels, the images can be processed to remove this low intensity noise. Images were taken with no source present to obtain pure noise images, and the intensity of the pixels considered and compared with those from α radiation to determine a threshold.

The α -particle data were taken from the experiments performed as described in Section 3.3.4. The noise data were taken from a sum of 97 exposures with no source present.

3.4 References

- [1] A. Shor *et al.*, "Branching ratio to the 803 keV level in Po 210 α decay," *Phys. Rev. C*, vol. 97, no. 3, pp. 1–6, 2018.
- [2] M. Bé, V. Chisté, C. Dulieu, V. Chechev, N. Kuzmenko, and M. Galán, "Table of Radionuclides (Vol. 4 – A = 133 to 252)," vol. 5, 2010.
- [3] M.-M. Bé *et al.*, "Table of Radionuclides (Vol. 3 - A = 3 to 244)," vol. 3, 2006.
- [4] E. J. Axton and A. G. Bardell, "Neutron yield from the spontaneous fission of ^{252}Cf ," *Metrologia*, vol. 21, no. 2, pp. 59–74, 1985.
- [5] R. C. Martin, J. B. Knauer, and P. A. Balo, "Production, Distribution, and Applications of Californium-252 Neutron Sources," 1999.
- [6] "Ultrastar and Ultrastar C," *Starlight Xpress*. [Online]. Available:

<https://www.sxccd.com/ultrastar-and-ultrastar-c>. [Accessed: 29-Mar-2019].

- [7] A. Theuwissen, *Solid-state Imaging with Charge-Coupled Devices*. 1995.
- [8] S. M. Sze and K. K. Ng, *Physics of Semiconductor Devices*, 3rd ed. Hoboken: John Wiley & Sons, 2006.
- [9] P. M. Epperson and M. B. Denton, "Binning Spectral Images in a Charge-Coupled Device," *Anal. Chem.*, vol. 61, no. 14, pp. 1513–1519, 1989.
- [10] J. F. Ziegler, M. D. Ziegler, and J. P. Biersack, "SRIM – The stopping and range of ions in matter (2010)," *Nucl. Instruments Methods Phys. Res. Sect. B Beam Interact. with Mater. Atoms*, vol. 268, no. 11–12, pp. 1818–1823, Jun. 2010.
- [11] H. Demers *et al.*, "Three-dimensional electron microscopy simulation with the CASINO Monte Carlo software.," *Scanning*, vol. 33, no. 3, pp. 135–46, Jan. .
- [12] L. K. Townsley, P. S. Broos, G. Chartas, E. Moskalenko, J. A. Nousek, and G. G. Pavlov, "Simulating CCDs for the Chandra Advanced CCD Imaging Spectrometer," *Nucl. Instruments Methods Phys. Res. Sect. A Accel. Spectrometers, Detect. Assoc. Equip.*, vol. 486, no. 3, pp. 716–750, Jul. 2002.
- [13] M. Bautz, J. A. Nousek, and G. Garmire, "Calibration report for the AXAF CCD imaging spectrometer," 1999. .
- [14] B. Burke, P. Jorden, and V. U. Paul, "CCD technology," *Exp. Astron.*, vol. 19, no. 1–3, pp. 69–102, 2006.
- [15] *Measurement, Instrumentation, and Sensors Handbook, Second Edition: Electromagnetic, Optical, Radiation, Chemical, and Biomedical Measurement*. CRC Press, 2014.

- [16] A. Aguilar-Arevalo *et al.*, "Measurement of radioactive contamination in the CCD's of the DAMIC experiment," *J. Phys. Conf. Ser.*, vol. 718, p. 042057, May 2016.
- [17] J. R. Janesick, *Scientific Charge-coupled Devices*. SPIE Press, 2001.
- [18] A. Sopczak *et al.*, "Modeling of Charge Transfer Inefficiency in a CCD With High-Speed Column Parallel Readout," *IEEE Trans. Nucl. Sci.*, vol. 56, no. 3, pp. 1613–1617, Jun. 2009.
- [19] F. Li and A. Nathan, *CCD Image Sensors in Deep-Ultraviolet: Degradation Behavior and Damage Mechanisms*. Springer Science & Business Media, 2006.
- [20] A. Aguilar-Arevalo *et al.*, "Measurement of radioactive contamination in the high-resistivity silicon CCDs of the DAMIC experiment," *J. Instrum.*, vol. 10, no. 08, pp. P08014–P08014, Aug. 2015.
- [21] G. H. Kinchin and R. S. Pease, "The Displacement of Atoms in Solids by Radiation," *Reports Prog. Phys.*, vol. 18, no. 1, p. 301, Jan. 1955.
- [22] J. F. Ziegler, J. P. Biersack, and M. D. Ziegler, *SRIM: Stopping and Range of Ions in Matter*. 2008.
- [23] J. S. Lilley, *Nuclear Physics: Principles and Applications*. John Wiley & Sons, 2001.
- [24] J. H. Hubbell and S. M. Seltzer, "X-Ray Mass Attenuation Coefficients," *NIST Stand. Ref. Database 126*, 2004.
- [25] E. Savvides, M. Zamani, and S. Charalambous, "An Approach to Fast and Thermal Neutron Spectroscopy Based on ${}^6\text{Li}(n,\alpha){}^3\text{H}$ Reaction," *Nucl. Tracks*

Radiat. Meas., vol. 15, pp. 495–498, 1988.

- [26] T. A. Cavalieri, V. A. Castro, and P. T. D. Siqueira, “Differences in Tld 600 and Tld 700 Glow Curves Derived From Distict Mixed Gamma/Neutron Field Irradiations,” *2013 Int. Nucl. Atl. Conf.*, pp. 24–29, 2013.
- [27] N. Soppera, M. Bossant, and E. Dupont, “JANIS 4: An Improved Version of the NEA JAva-based Nuclear Data Information System,” *Nucl. Data Sheets*, vol. 120, 2014.
- [28] J. Glodo *et al.*, “Fast neutron detection with Cs₂LiYCl₆,” *IEEE Trans. Nucl. Sci.*, vol. 60, no. 2, pp. 864–870, 2013.
- [29] P. V. Ma, T.P. and Dressendorfer, “Ionizing Radiation Effects in MOS Devices and Circuits,” p. 587, 1989.
- [30] Z. Wang *et al.*, “Dose rate effects on array CCDs exposed by Co-60 γ rays induce saturation output degradation and annealing tests,” *AIP Adv.*, vol. 5, no. 10, 2015.
- [31] G. R. Hopkinson and A. Mohammadzadeh, “CCD Radiation Testing at Low Temperatures Using a Laboratory Alpha Particle Source,” *IEEE Trans. Nucl. Sci.*, vol. 53, no. 6, pp. 3758–3763, Dec. 2006.
- [32] G. R. Hopkinson and A. Mohammadzadeh, “Comparison of CCD Damage Due to 10- and 60-MeV Protons,” *IEEE Trans. Nucl. Sci.*, vol. 50, no. 6 I, pp. 1960–1967, 2003.
- [33] C. Tivarus and W. C. McColgin, “Dark Current Spectroscopy of Irradiated CCD Image Sensors,” *IEEE Trans. Nucl. Sci.*, vol. 55, no. 3, pp. 1719–1724, Jun. 2008.

- [34] N. Meidinger, L. Strüder, P. Holl, H. Soltau, and C. v. Zanthier, "Analysis of trapping effects on charge transfer in proton irradiated pn-CCDs," *Nucl. Instruments Methods Phys. Res. Sect. A Accel. Spectrometers, Detect. Assoc. Equip.*, vol. 377, no. 2–3, pp. 298–311, Aug. 1996.

4 Results

4 RESULTS	78
4.1 CCDs for radiation detection	79
4.1.1 <i>SRIM simulations</i>	79
4.1.2 <i>CASINO simulations</i>	83
4.1.3 <i>Initial images</i>	86
4.2 Detecting β radiation	89
4.2.1 <i>Cluster sizes for different energy β particles</i>	89
4.2.2 <i>Blocking β radiation</i>	91
4.3 Detecting α radiation	95
4.3.1 <i>Cluster sizes</i>	95
4.3.2 <i>Streak lengths</i>	97
4.3.3 <i>Pixel intensities</i>	98
4.4 Detecting neutron radiation.....	100
4.5 Noise investigations	105
4.5.1 <i>Identifying radiation damage</i>	108
4.5.2 <i>Damage repair and mitigation</i>	113
4.6 References	119

This chapter describes the results for the simulations and experiments performed, consisting of five sections. The first section shows the interactions of radiation with the CCDs, through simulations showing the α - and β -particle interactions, and initial images taken with the CCDs. Results from experiments performed with different types of radiation are then presented, organised by the radiation type being considered. Initially, investigations into the detection of β^- particles are presented, followed by similar

experiments performed for α radiation and then neutron radiation. Finally, results derived from investigations of the source of noise and trials of methods to mitigate these problems are given.

During this research, 45 images were analysed in the β^- -radiation section with exposures typically between 1 s and 10 s, 185 images were analysed in the α -radiation section with exposures typically between 30 s and 5 minutes, and 4 images were analysed in the neutron section with exposures between 10 minutes and 30 minutes. Fewer images were used for the neutron investigations due to the longer times required for the exposures. For the noise investigations, 18 exposures were used to identify the source of the noise for α particles and 24 for β^- particles. 97 noise exposures were analysed for the intensities and cluster sizes. For each of the cooling methods used, 10 exposures were analysed. Finally, 20 exposures were used to test the annealing process. Image processing techniques were performed using existing exposures. Many additional exposures were taken to inform this research, such as during the investigation of different annealing temperatures as described in Section 3.3.6.1, but were not used in the final analyses. A few typical examples of the raw images have been included in this chapter, however the value of the images is in the analysis which has been presented in place of the entirety of the raw images.

4.1 CCDs for radiation detection

4.1.1 SRIM simulations

Simulations were performed using SRIM (the Stopping and Range of Ions in Matter) [1] to investigate the interactions of α particles in the CCD. The aim of this was to identify the potential of using these devices to detect α particles. The simulations were made to find the energy loss of the α particles from the ^{210}Po source and to identify how many of the α particles should be detected, based on the range they penetrate into the CCD. Figure 4.1 shows the simulation through the entire source-to-CCD distance, and Figure 4.2

focuses on the CCD layers to show the relevant information more clearly. In each, the tracks of the α particles are shown on the left and the energy loss to ionisation is shown on the right.

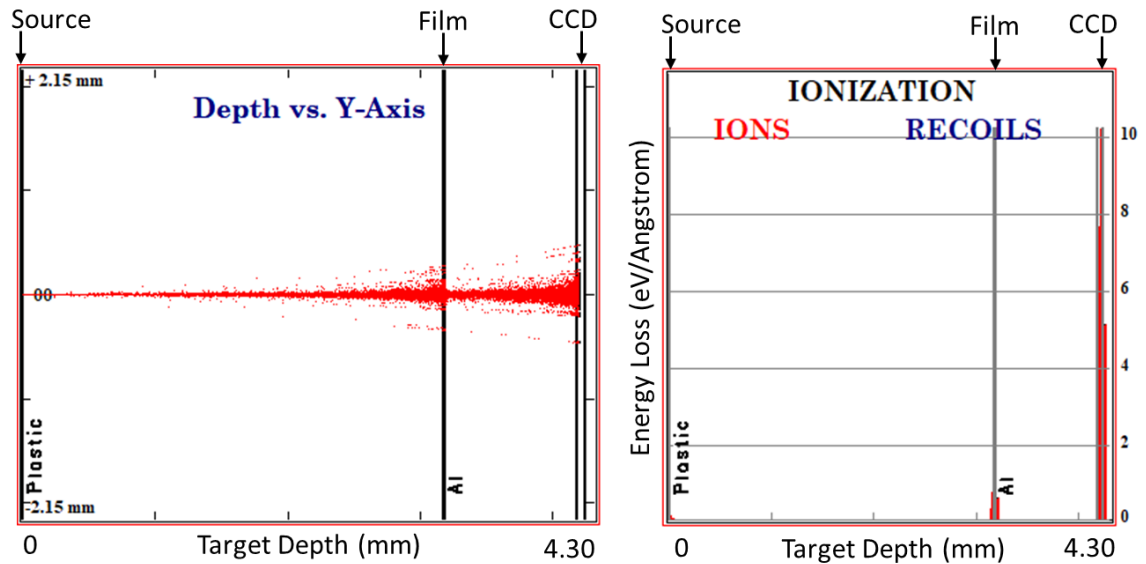


Figure 4.1 SRIM simulation results for the interactions of 10,000 α particles with an incident energy of 5.304 MeV through the total source-to-CCD distance. Left: α -particle tracks showing their range and spread. Right: Energy loss to ionisation as a function of depth.

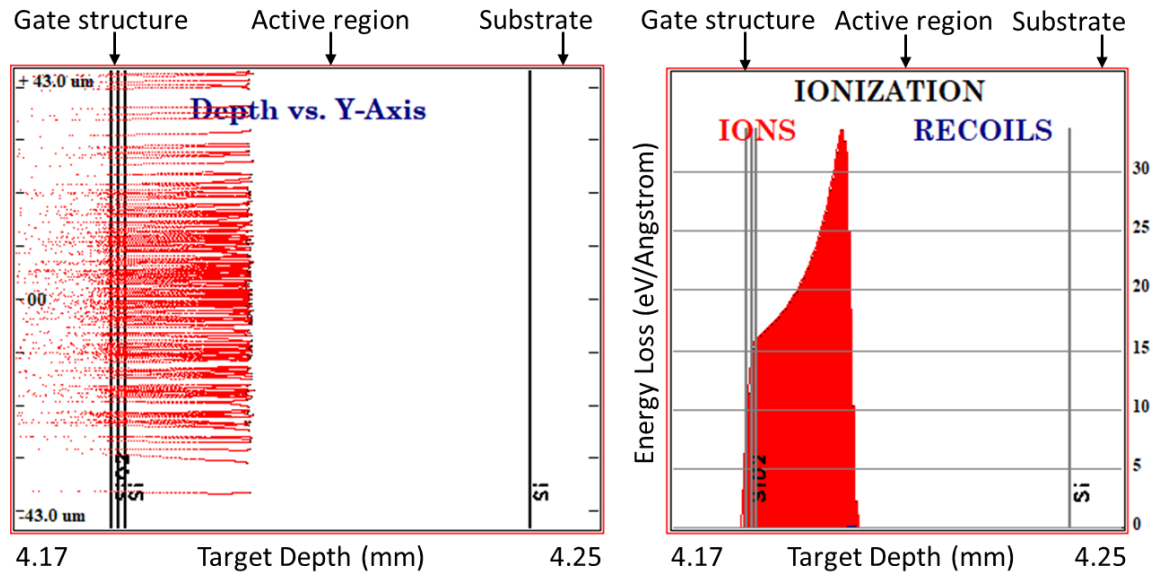


Figure 4.2 SRIM simulation sections focusing on the CCD layers. **Left:** Tracks showing the range of the α particles within the CCD. Only 200 tracks are shown for clarity. **Right:** Energy loss to ionisation for all 10,000 α particles simulated as a function of depth.

The data from these graphs show that all of the α particles will be stopped at a depth of 16 μm into the active layer of the CCD after passing through all of the prior layers. An average energy loss for each α particle prior to entering the active region was calculated to be 1.6 MeV, leaving 3.7 MeV available to be detected. These were for the conservative gate thickness estimates used; the thinner values have a range of 17 μm into the active region, and an energy loss of 1.4 MeV before this layer.

Full-damage calculations performed using SRIM show that each ion from ^{210}Po produces 356 displacements in the target. Of these, 27 are replaced through further collisions, giving the total number of vacancies as 329 per ion. This covers the entire source-to-CCD distance, however the collision events graph in Figure 4.3 shows that the majority of these occur within the CCD active layer.

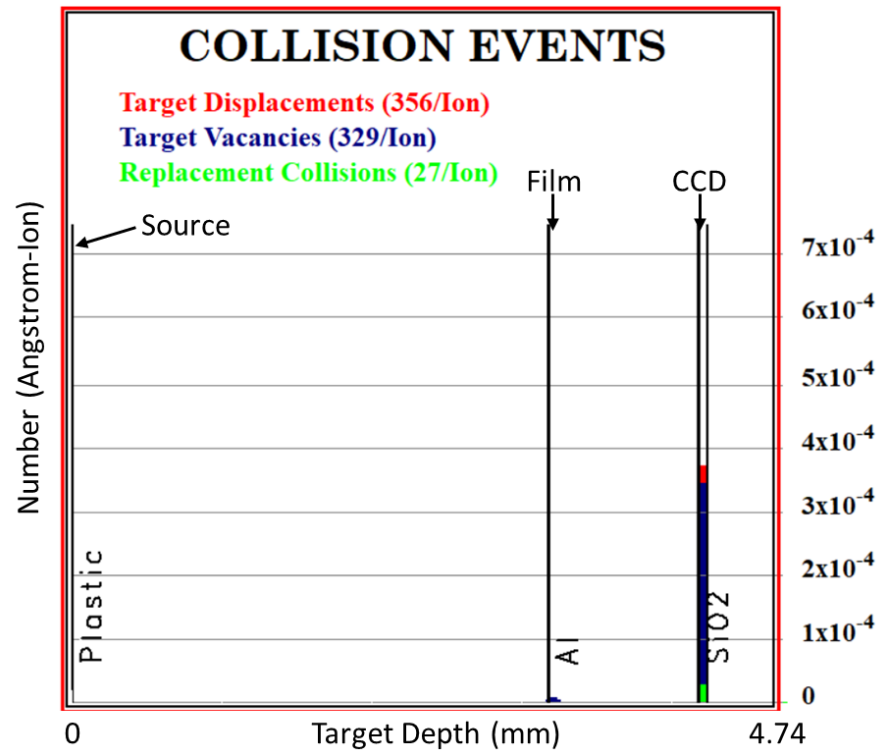


Figure 4.3 SRIM simulation showing the collisions of 10,000 α particles with an incident energy of 5.304 MeV through the total source-to-CCD distance. The displacements per ion, replacement collisions, and resultant number of vacancies are shown. The detail of what is happening in the CCD can be seen in Figure 4.2.

To test the potential of the device to detect a broad range of α -particle energies, two additional energies were simulated. The conservative CCD gate structure was used. To account for different detection situations, simulations were performed both with the source in contact with the Mylar film and with the full ^{210}Po source structure, including the covering plastic and air layer. The total ranges and energy loss prior to the active layer are given in Table 4.1.

Table 4.1 Average energy remaining to be detected in the active region and range of the α particles into the active region for different α -particle energies, using conservative gate thickness estimates.

α -particle energy	Direct contact with Mylar		^{210}Po source structure	
	Depth into active region (mm)	Detectable energy (MeV)	Depth into active region (mm)	Detectable energy (MeV)
8.748 MeV (^{212}Po)	0.049 ± 0.001	7.951	0.047 ± 0.001	7.706
5.304 MeV (^{210}Po)	0.018 ± 0.001	4.132	0.016 ± 0.001	3.736
2.232 MeV (^{147}Sm)	0.00 ± 0.03	0.021	-0.1 ± 0.2	0.007

4.1.2 CASINO simulations

To improve the ability to identify β^- particles, CASINO [2] simulations were performed to estimate the number of pixels the β^- particles will scatter through. Example tracks of electrons scattering through the active layer and substrate layers of the model for energies representing ^{60}Co and ^{137}Cs are shown in Figure 4.4

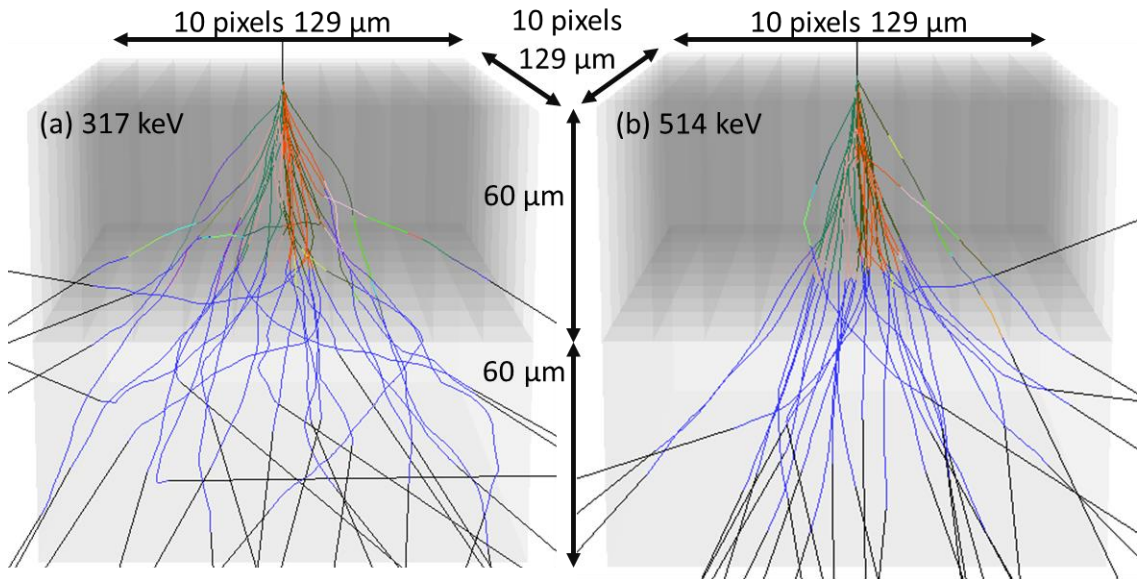


Figure 4.4 CASINO simulations showing 30 of the 10,000 tracks for β particles with an energy of (a) 317 keV and (b) 514 keV to represent ^{60}Co and ^{137}Cs , respectively. 10×10 binned pixels are simulated. These are $60 \mu\text{m}$ deep on top of a $60 \mu\text{m}$ substrate layer. All regions are silicon. Different colours represent different regions each electron has passed through.

The backscattering coefficients are 0.07 for the 317 keV electrons and 0.01 for the 514 keV electrons. This is the probability that electrons are scattered back out of the CCD, rather than passing through the full active layer. The cluster sizes were calculated as the number of unique pixels each electron passed through, not including the substrate. The simulated cluster sizes can be seen for the two energies in Figure 4.5.

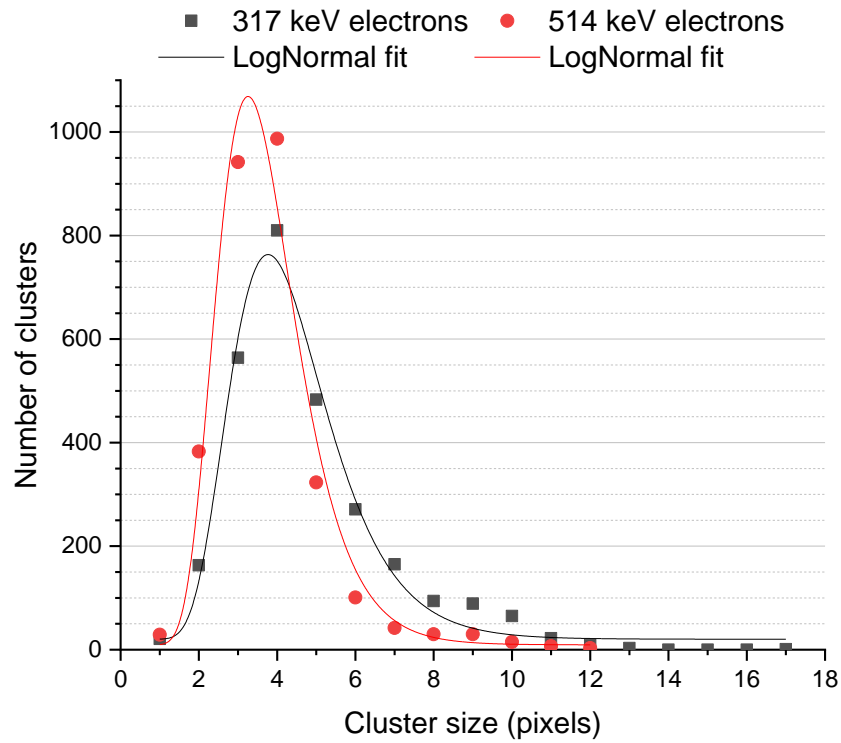


Figure 4.5 CASINO simulation data showing the cluster sizes for 10,000 electrons at two energies, 317 keV and 514 keV, passing through the active layer and substrate of the CCD.

LogNormal curves gave the best empirical fit to these data. The equation of a lognormal curve is:

$$y = y_0 + \frac{A}{\sqrt{2\pi} \sigma_l x} e^{-\frac{(\ln(\frac{x}{xc}))^2}{2\sigma_l^2}}, \quad (4.1)$$

Where y_0 is the offset, xc is the centre, σ_l is the log standard deviation, and A is the area [3]. The parameters for the two fits are given in Table 4.2. The mean value for 317 keV, μ , is 4.42 with a standard deviation, σ , of 1.48. For 514 keV the mean is 3.8 and the standard deviation is 1.2.

Table 4.2 Parameters for the lognormal fits in Figure 4.5, of simulated cluster sizes for 317 keV and 514 keV electrons.

Parameter	317 keV		514 keV	
	Value	Standard error	Value	Standard error
y_0	20	11	9	30
xc	4.19	0.07	3.58	0.09
σ_l	0.33	0.02	0.31	0.02
A	2416	95	2780	180
$Adj.R^2$	0.9796		0.9597	

4.1.3 Initial images

The response of the CCDs to different types of radiation was tested by exposing them to three separate sources, ^{210}Po , ^{137}Cs , and ^{60}Co . An example of a typical exposure to each of these sources can be seen in Figure 4.6-Figure 4.8.



Figure 4.6 Typical example of a 6-minute exposure to a ^{210}Po α -particle source with an activity of 43 Bq. Clusters are highlighted to have the maximum intensity of 255 ADU.



Figure 4.7 Typical example of a 1-s exposure to a ^{137}Cs β/γ source with an activity of 330 kBq. Clusters are highlighted to have the maximum intensity of 255 ADU.



Figure 4.8 Typical example of a 5-s exposure to a ^{60}Co β/γ source with an activity of 8.84 kBq. Clusters are highlighted to have the maximum intensity of 255 ADU.

These are full size 696×520 pixel images produced by the CCD, where the pixels have been highlighted such that all of the pixel intensities above the software threshold have been set to the maximum value of 255 ADU (Analog to Digital Units). This is to enable the sizes and shapes of the pixel clusters to be seen more clearly.

4.2 Detecting β radiation

4.2.1 Cluster sizes for different energy β particles

To compare with the CASINO simulations, cluster sizes taken from exposures to the ^{60}Co and ^{137}Cs sources have been analysed. These are for all clusters produced by the two sources, including those produced by γ radiation and the full spectrum of β -particle energies. The data, along with LogNormal fits, can be seen in Figure 4.9. The parameters

for the fits are given in Table 4.3. For 317 keV the mean is 1.91 and the standard deviation is 1.01, and for 514 keV the mean is 1.21 and the standard deviation is 1.11.

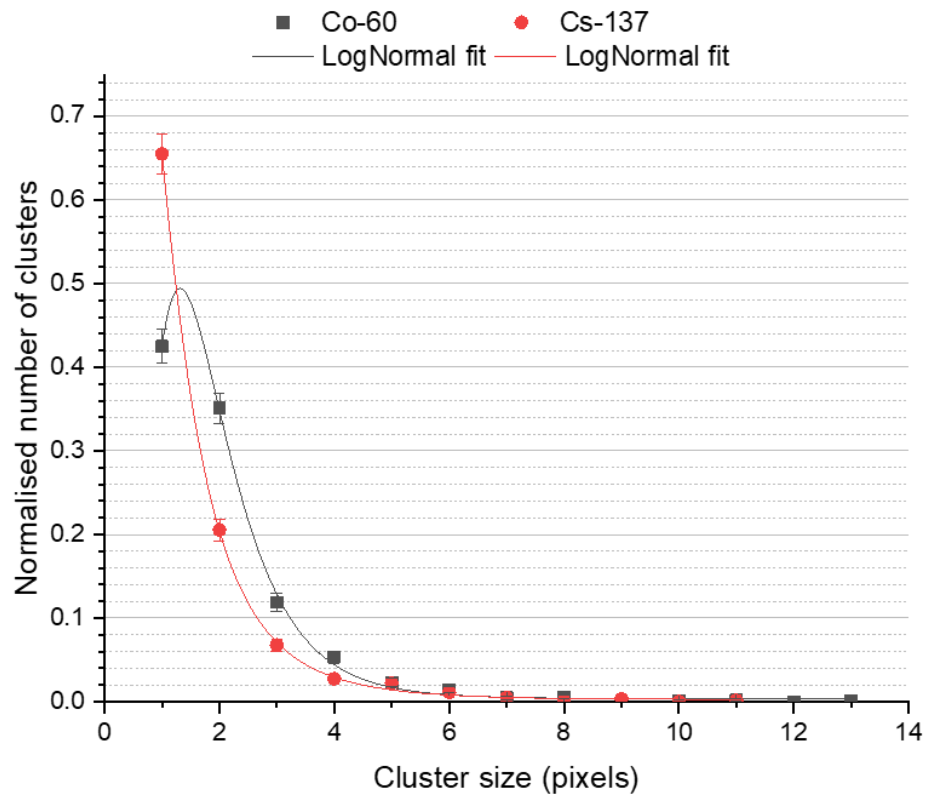


Figure 4.9 Cluster sizes for clusters produced by ^{60}Co and ^{137}Cs interactions in the CCD. The number of clusters has been normalised; the original number of counts used are 1043 for ^{60}Co and 1168 for ^{137}Cs .

Table 4.3 Parameters for the lognormal fits in Figure 4.9, of the cluster sizes produced by exposures to ^{60}Co and ^{137}Cs .

Parameter	^{60}Co		^{137}Cs	
	Value	Standard error	Value	Standard error
y_0	0.004	0.002	0.002	0.002
xc	1.69	0.02	0.95	0.06
σ_l	0.50	0.01	0.75	0.05
A	0.91	0.02	1.24	0.01
$Adj.R^2$	0.9983		0.9996	

4.2.2 Blocking β radiation

A comparison of the number of clusters produced when exposed to ^{60}Co and ^{137}Cs covered with 4-mm thick piece of aluminium to effectively block the β^- radiation, is shown in Figure 4.10. Typical examples of the ^{137}Cs exposures can be seen in Figure 4.11. When covered, the number of clusters produced by the ^{60}Co source decreases by $(98 \pm 31)\%$, from (1053 ± 33) to (29 ± 9) clusters. For the ^{137}Cs source, the number of clusters reduces by $(89 \pm 26)\%$, from (1228 ± 64) to (131 ± 35) clusters. As the two sources are not being directly compared, the number of clusters has not been normalised. This allows for a comparison between the covered and uncovered situations for exposures of a set length of time.

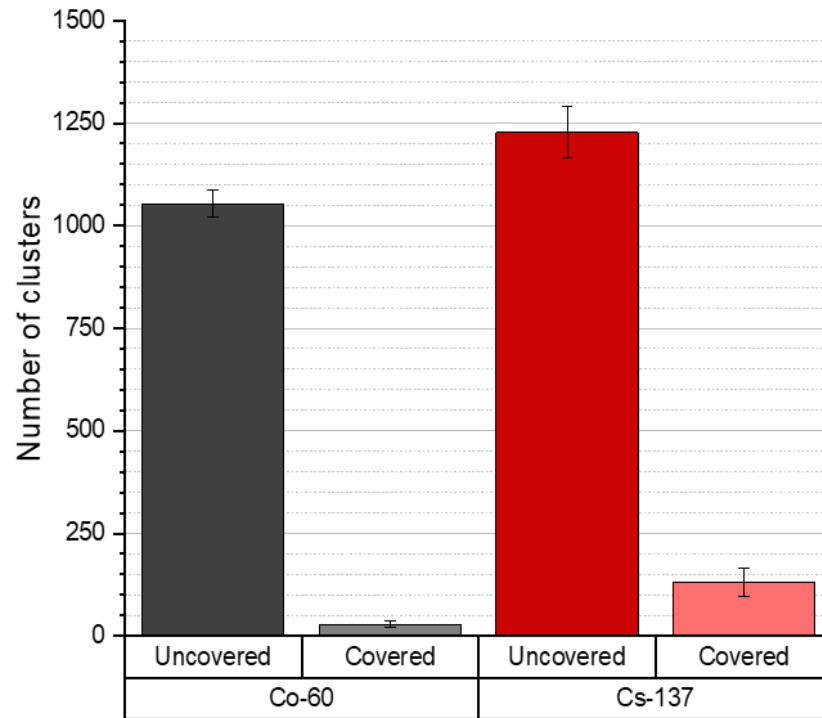


Figure 4.10 The average number of clusters produced in 55-s exposures to ^{60}Co and 10-s exposures to ^{137}Cs , both with and without a 4 mm aluminium covering. Each average is over 10 images.

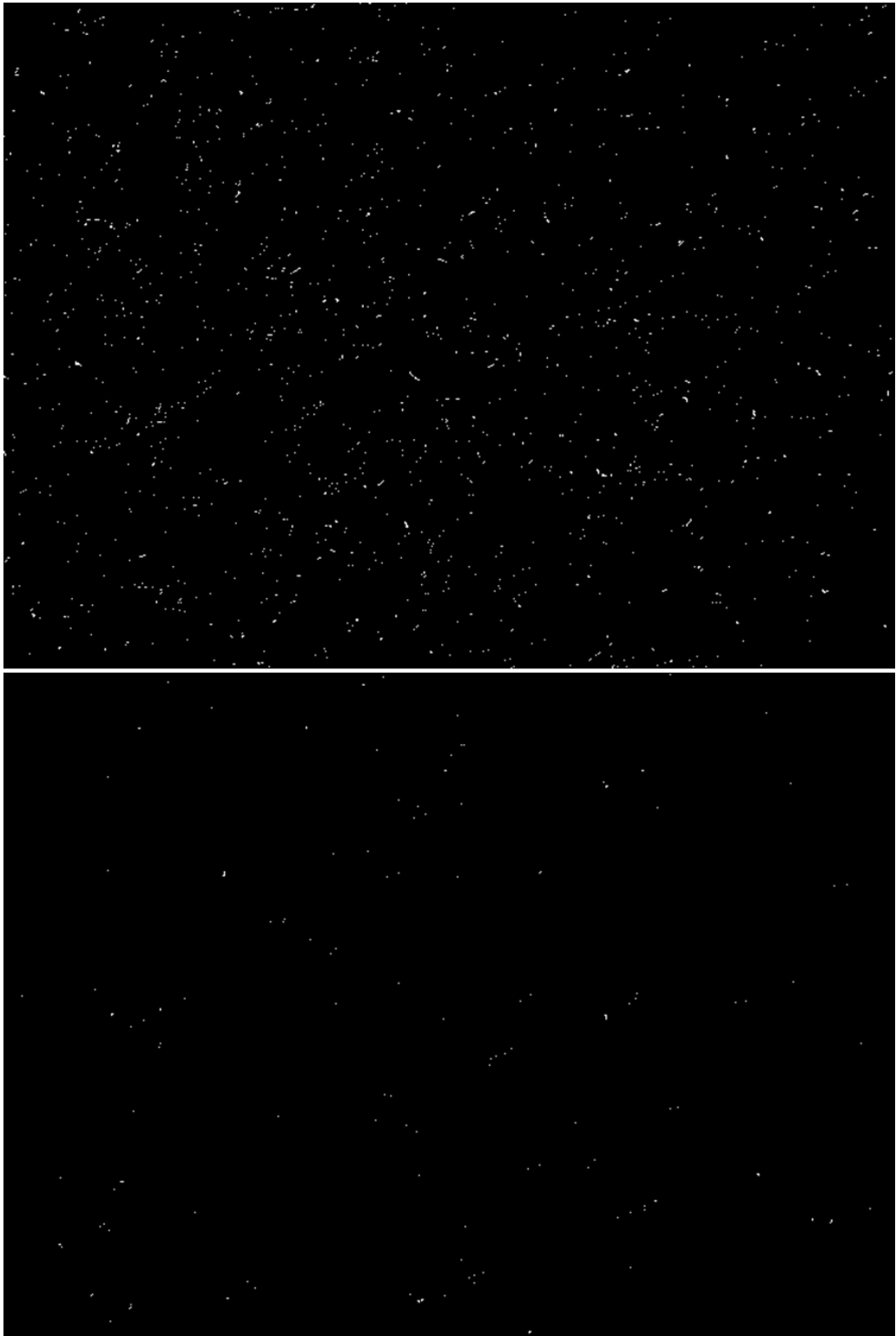


Figure 4.11 Example 10-s exposures to a ^{137}Cs source of activity 312 keV uncovered (top) and covered with a 4 mm piece of aluminium (bottom). Clusters are highlighted to have the maximum intensity (255 ADU).

The intensity of the brightest pixel in each cluster was analysed for both the covered and the uncovered states. Examples sections showing the intensities of some clusters are shown in Figure 4.12. The graphical data is given in Figure 4.13. In each of the four cases, there were some clusters which had pixels of the maximum intensity. For ^{60}Co , 0.23% of the uncovered clusters and 0.35% of the covered clusters had the maximum intensity. For ^{137}Cs the percentages are 0.17% for the uncovered clusters and 0.15% for the covered clusters.

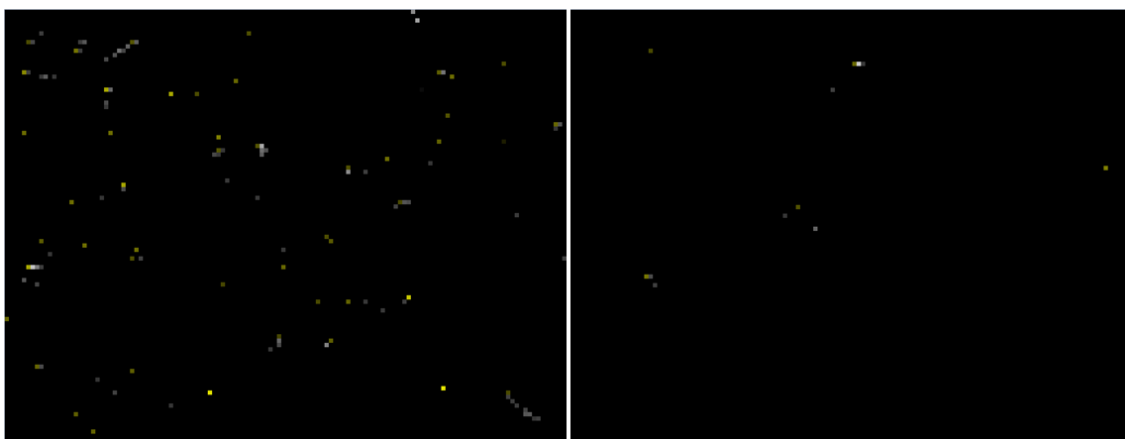


Figure 4.12 Example 130×100 pixel sections of the exposures in Figure 4.11, demonstrating the original intensities of the clusters.

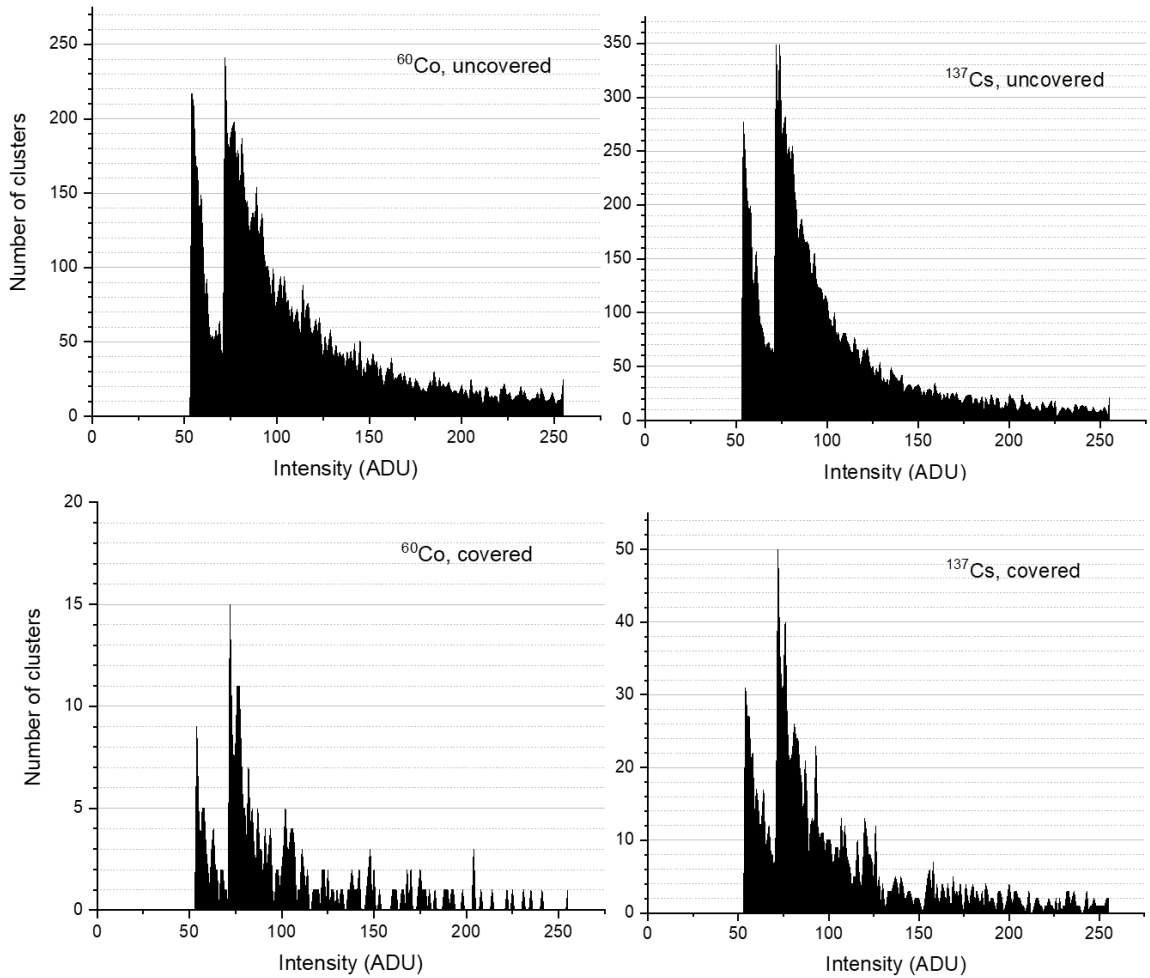


Figure 4.13 The intensities of the brightest pixels in clusters produced in exposures to ^{60}Co (left) and ^{137}Cs (right), both uncovered (top) and with a 4mm aluminium covering to block the β radiation (bottom). Each graph uses data from 10 exposures. The CCD software removes pixels below a threshold intensity of 54 ADU.

4.3 Detecting α radiation

4.3.1 Cluster sizes

The overall sizes of the clusters produced by the interactions of α particles from the ^{210}Po source with the CCD can be seen in Figure 4.14. This analysis was performed without processing the images to remove noise. The number of 1-pixel clusters was 54,700 and was not included on this graph so the rest of the data can be seen more clearly. A Gaussian

fit was found to be the best empirical fit for these data, excluding the data from 1- and 2-pixel cluster sizes. The equation of a Gaussian curve as fit by OriginPro® is:

$$y = y_0 + \frac{A'}{\sqrt{\frac{\pi}{2}} w} e^{-2\left(\frac{x-xc}{w}\right)^2}, \quad (4.2)$$

where y_0 is the offset, xc is the centre of the peak, w is the width at 1 standard deviation (σ), and A' is the area [4]. The parameters of this fit for the cluster sizes are given in Table 4.4, including the height and full width at half maximum (FWHM).

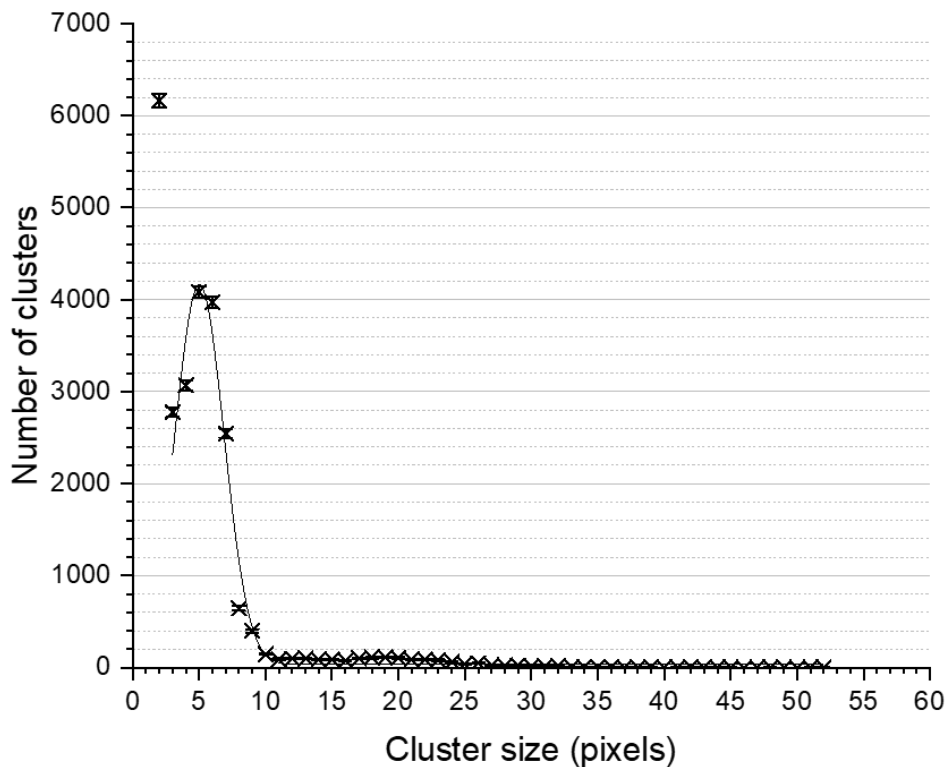


Figure 4.14 Cluster sizes for α particles produced by ^{210}Po . Clusters of 1 pixel were not included, with a value of 54,700.

Table 4.4 Parameters for the Gaussian fit in Figure 4.14, for cluster sizes from α particles produced by ^{210}Po .

Parameter	Value	Standard error
y_0	32	22
x_c	5.02	0.06
w	3.7	0.1
A'	19200	600
σ	1.85	0.07
<i>FWHM</i>	4.4	0.2
<i>Height</i>	4100	100
<i>Adj. R²</i>	0.9789	

4.3.2 Streak lengths

The streak lengths were calculated using the height of the bounding box and are given in Figure 4.15. The first three values are not included as a convention was adopted such that these do not constitute streaks, primarily because the large numbers of these obscure the relevant streak information. The missing values are: 1 = 75,312; 2 = 14,718; and 3 = 3066.

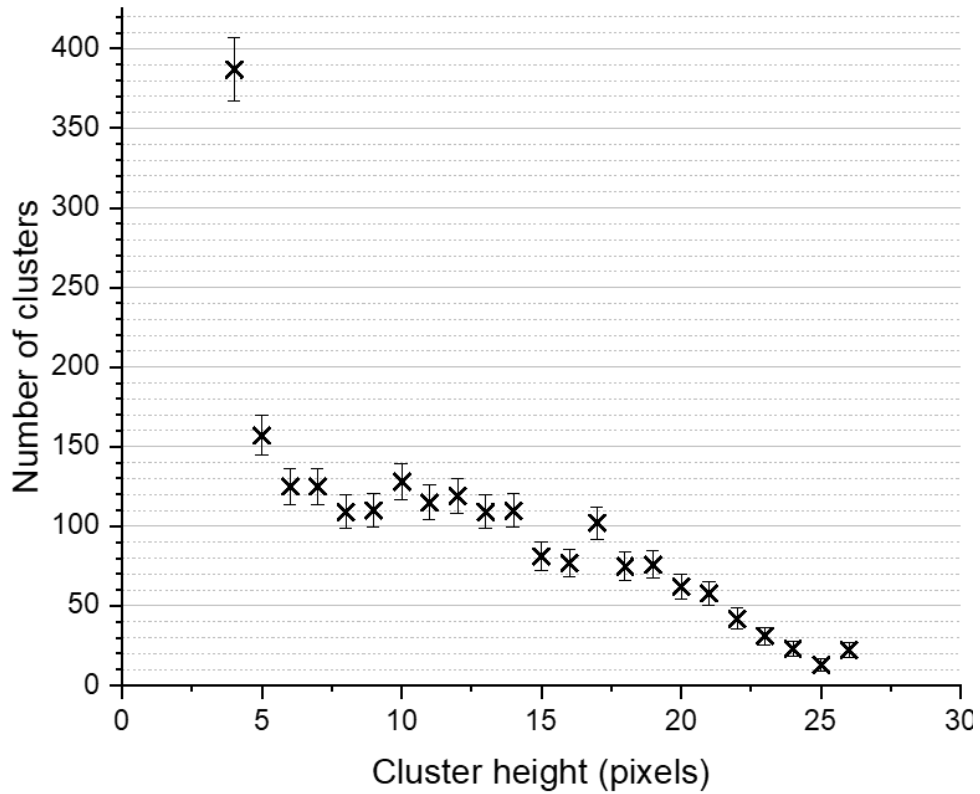


Figure 4.15 Streak lengths for the ^{210}Po source. Cluster heights of 1-3 are excluded from the graph as these do not constitute streaks, to allow the relevant streak data to be seen more clearly.

Among 185 exposures to the ^{210}Po source, whilst the CCD is cooled, there was on average 1 streak for every (9 ± 4) clusters produced. A streak was defined as consisting of at least 6 pixels in vertical length, and a cluster was defined as having an area of at least 4 pixels.

4.3.3 Pixel intensities

Finally, the intensities of the clusters may be considered. Figure 4.16 is an example section of an exposure showing the intensities of clusters produced by interactions of α particles from the ^{210}Po source with the CCD. Signals determined to be from α radiation were investigated, and a plot of the intensity of the brightest pixel in each cluster is shown in Figure 4.17. The α signals were determined to be those greater than 3 pixels in size to

minimise the amount of noise that was included. 92% of the clusters had at least one pixel with the maximum possible intensity of 255 ADU.

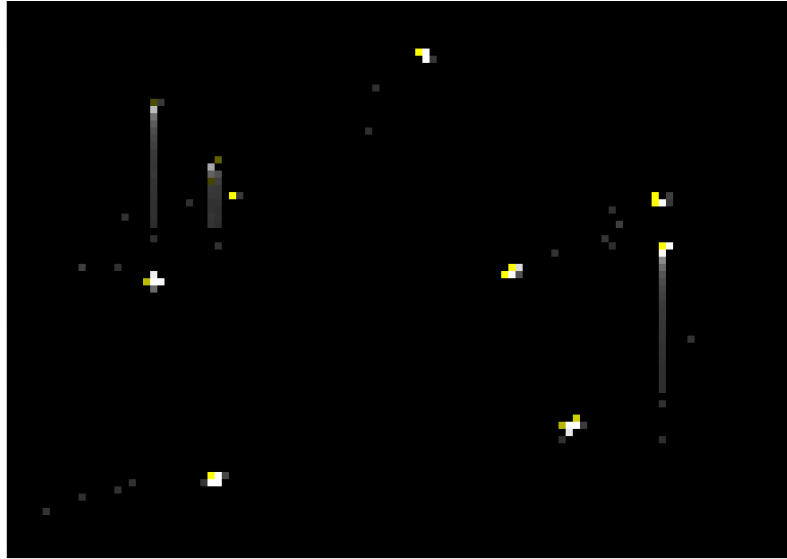


Figure 4.16 Example 110×78 pixel section of a typical exposure to the ^{210}Po source. The clusters have their original intensities.

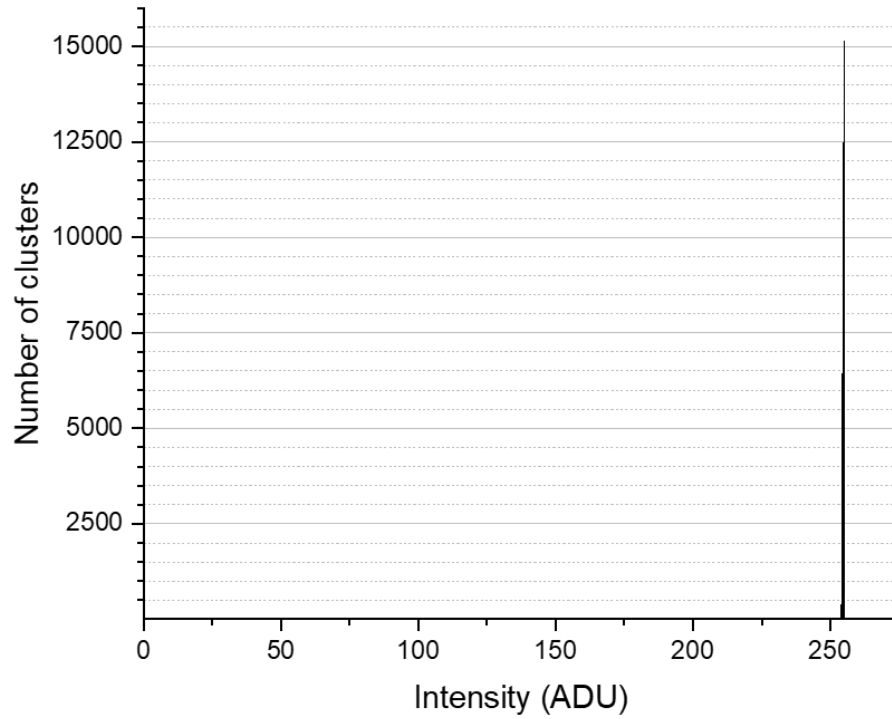


Figure 4.17 The intensities of the brightest pixels in clusters identified as being created from α particle interactions in the CCD. The software threshold automatically removed any pixels below 50 ADU.

4.4 Detecting neutron radiation

When the CCD covered with ${}^6\text{Li}$ -enriched crystals was exposed to neutron radiation, small bright clusters are seen, but there are no streaks, as seen in Figure 4.18.



Figure 4.18 Full 10-minute exposure to the ^{252}Cf neutron source with an activity of 17.5 MBq, with a covering of ^6Li -enriched crystals over the CCD. The clusters have been highlighted to the maximum intensity (255 ADU).

As both an α -particle and a triton (T^+) are produced in the reaction of neutrons with ^6Li , as shown in equation 3.5, simulations were performed to suggest which of the two products will have interacted with the CCD. SRIM simulations showing the energy loss to ionisation for each of these particles is given in Figure 4.19. The average energy loss prior to the active layer and the range into the CCD is given in Table 4.5.

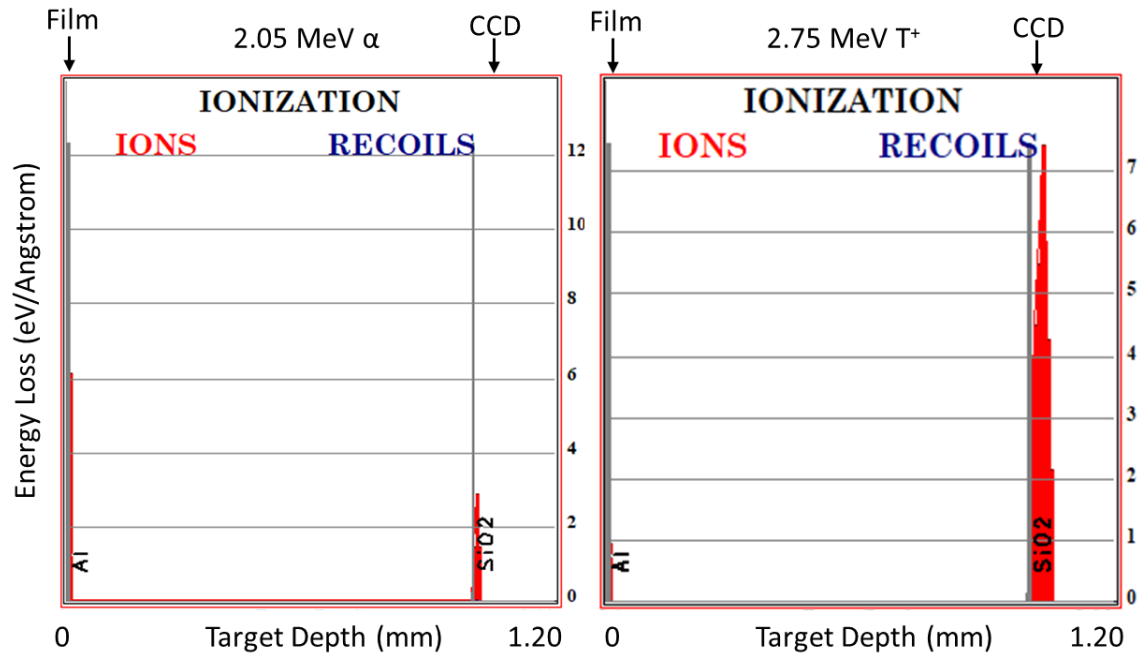


Figure 4.19 SRIM simulations showing the ionisation of 2.05 MeV α particles (left) and 2.75 MeV T^+ particles (right) in the CCD, with the particles produced in contact with the Mylar film.

Table 4.5 Average energy loss prior to the active region and total range of 2.05 MeV α particles and 2.75 MeV T^+ particles produced from neutron interactions with ${}^6\text{Li}$ in contact with the Mylar film.

	2.05 MeV α particle	2.75 MeV T^+
Energy loss prior to active region (MeV)	2.043	0.360
Range from Mylar film (mm) 1.008 mm to active region	1.01 ± 0.03	1.044 ± 0.001

After removal of noise from the images taken of the exposure to the ${}^{252}\text{Cf}$ neutron source using the lithium crystals, the following data were obtained for the total cluster size,

Figure 4.20, and the maximum intensity pixel per cluster, Figure 4.21. In total, 157 clusters were analysed, over 4 exposures totalling 1 hour. The parameters for the Gaussian fit for the cluster size data is given in Table 4.6. The percentage of clusters with at least one pixel of maximum intensity is 29%.

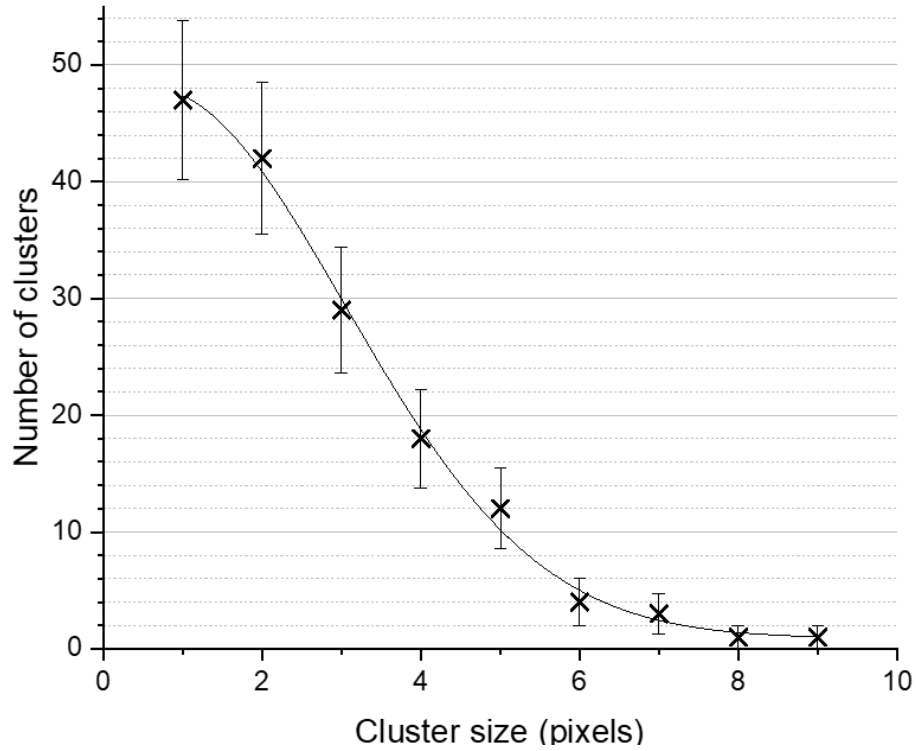


Figure 4.20 Cluster sizes for particles produced by experimental neutron interactions with ${}^6\text{Li}$. 157 clusters were analysed over 4 images.

Table 4.6 Parameters for the Gaussian fit in Figure 4.20, of the cluster sizes from particles produced in neutron interactions with ${}^6\text{Li}$.

Parameter	Value	Standard error
y_0	0.9	0.9
x_c	0.6	0.3
w	4.9	0.5
A'	290	40
σ	2.4	0.2
<i>FWHM</i>	5.8	0.5
<i>Height</i>	47	2
<i>Adj. R²</i>	0.9952	

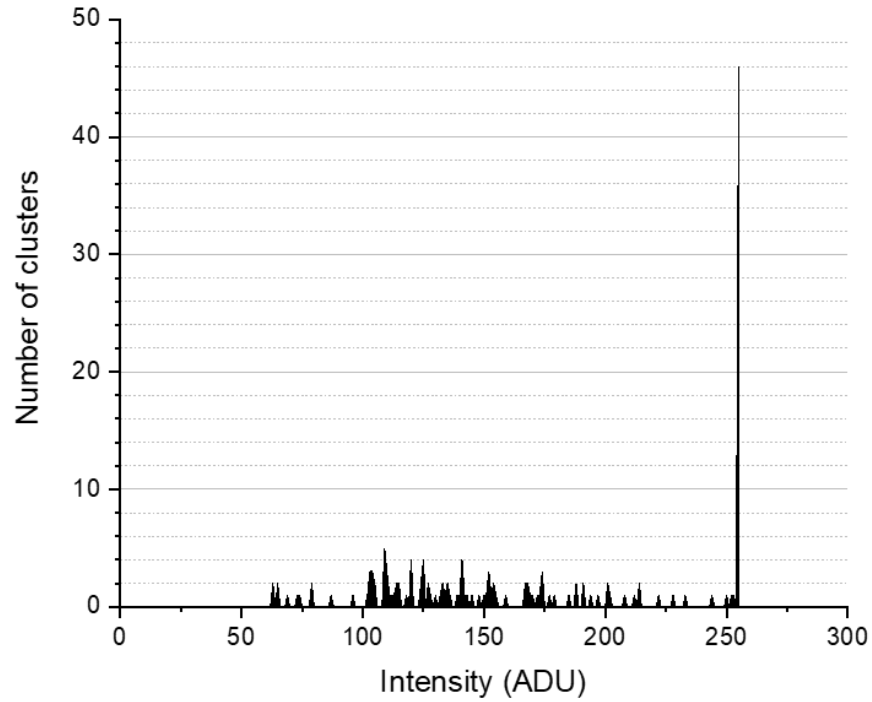


Figure 4.21 The intensity of the brightest pixel in each cluster from particles produced by the interaction of the neutron source with ${}^6\text{Li}$. The software threshold automatically removed any pixels below 50 ADU.

4.5 Noise investigations

Over time, an increased amount of noise was seen in the images produced by the CCD. An exposure of the CCD in the dark with no source present is shown in Figure 4.22, taken at a time when the CCD was exhibiting a lot of noise. As there is no source to generate clusters in the CCD, all the clusters seen are from noise within the CCD itself.



Figure 4.22 Example exposure with no source present, taken over 60-s with the CCD. Pixels have been highlighted to their maximum intensity (255 ADU).

The sizes of clusters produced by noise over 97 exposures with no source present are shown in Figure 4.23, and the intensity of the brightest pixel in each cluster is given in Figure 4.24. A power-law fit was found to be the best fit to the cluster size data, using the following equation:

$$y = ax^b, \quad (4.3)$$

where a is the coefficient and b is the power [5]. The parameters for this fit are given in Table 4.7.

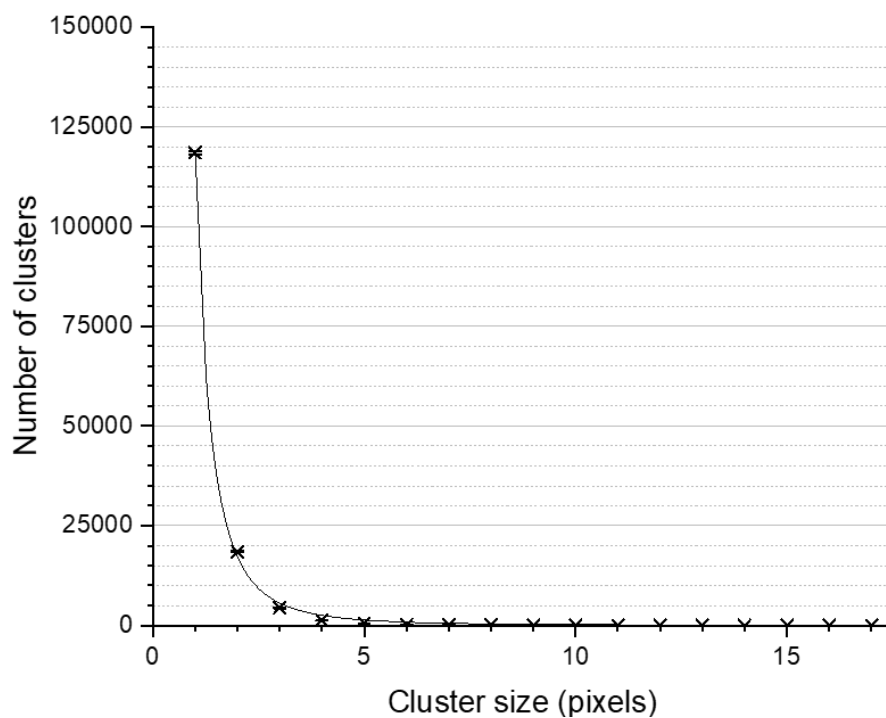


Figure 4.23 Sizes of clusters produced by noise within the CCD during exposures with no source present. 143,622 clusters were analysed over 97 images.

Table 4.7 Power-law fit parameters for the cluster sizes produced by noise within the CCD, in Figure 4.23.

Parameter	Value	Standard error
a	118600	600
b	-2.78	0.05
$Adj. R2$	0.9995	

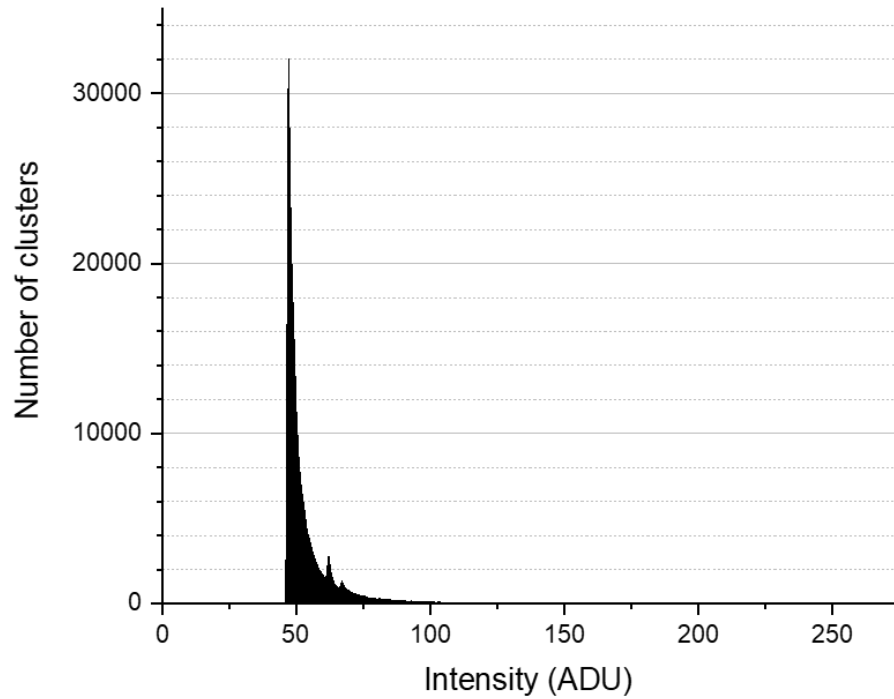


Figure 4.24 The intensities of the brightest pixels in clusters produced by noise in the CCD. The software threshold automatically removed any pixels below 50 ADU.

4.5.1 Identifying radiation damage

The comparison of the number of clusters in the background images produced by the half-covered CCD after increasing exposure times to the ^{210}Po source can be seen in Figure 4.25. On the uncovered side, where α particles can interact with the CCD, there is an increase in the number of counts. The covered side, with the α particles blocked, has no significant change. The difference can be seen in Figure 4.26, which gives example background images before and after the 5-hour irradiation.

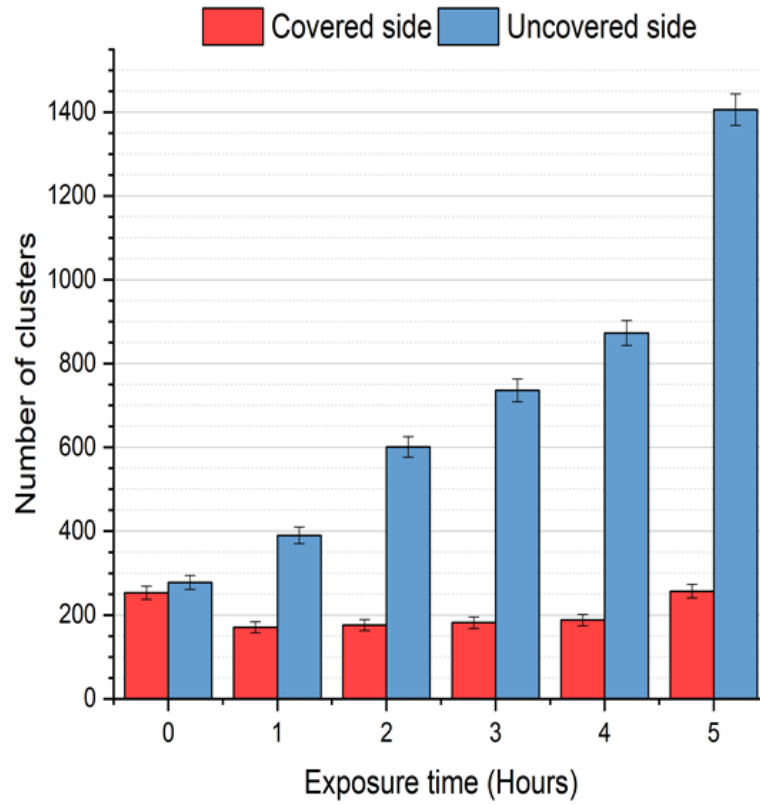


Figure 4.25 The number of bright pixels in a 30-s background measurement for equivalent sized sections on the covered and uncovered side of the CCD after each additional exposure to a ^{210}Po source.

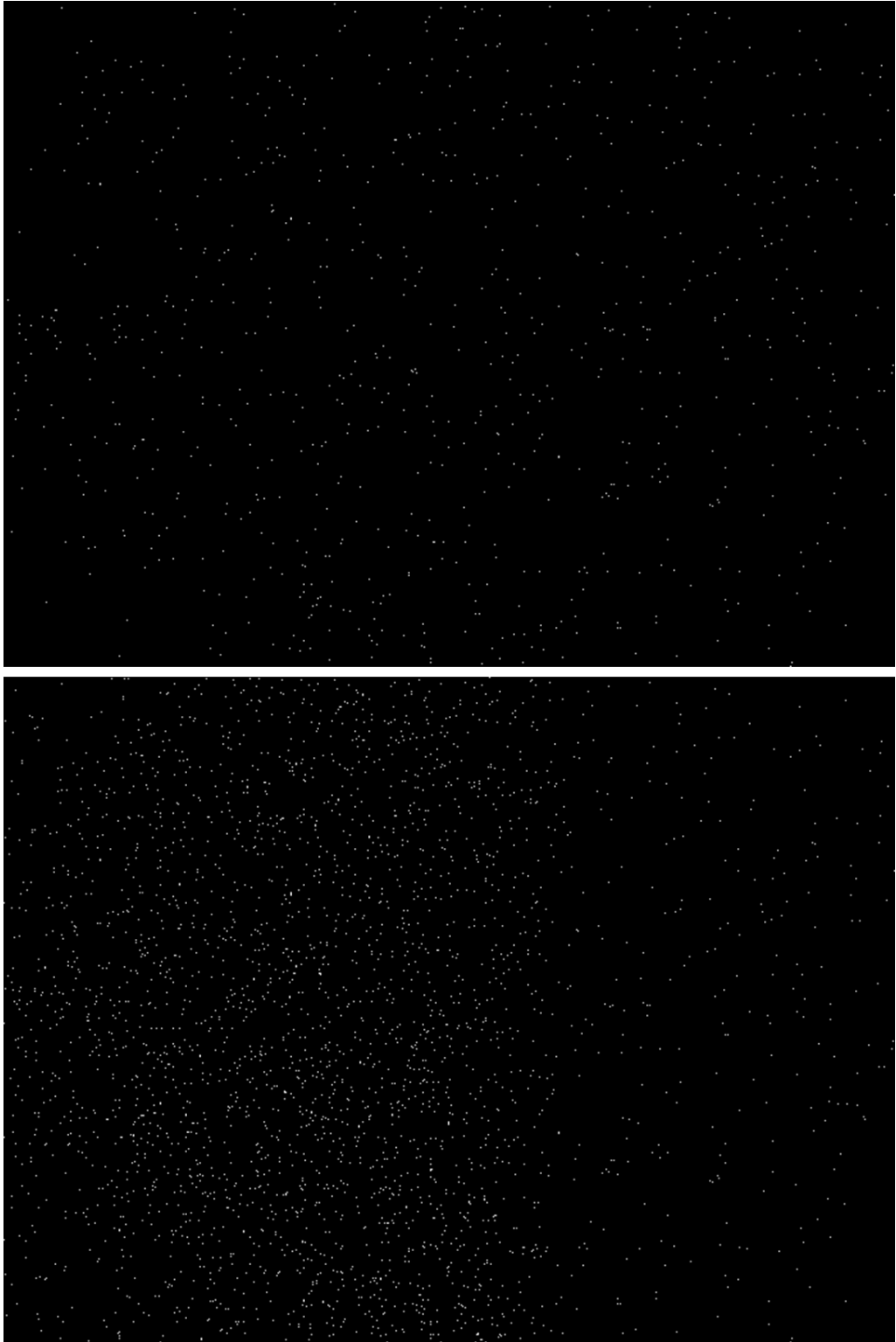


Figure 4.26 Example images of the 30-s background before irradiation (top) and after 5 hours exposure to the ^{210}Po source (bottom), with the right half of the CCD covered in card.

A similar test was performed with the ^{137}Cs source considering the whole CCD imaging area over sessions totalling 19 hours, shown in Figure 4.27. Example backgrounds before exposure and after 19 hours are shown in Figure 4.28. There is no significant increase in the number of clusters in the background over this time.

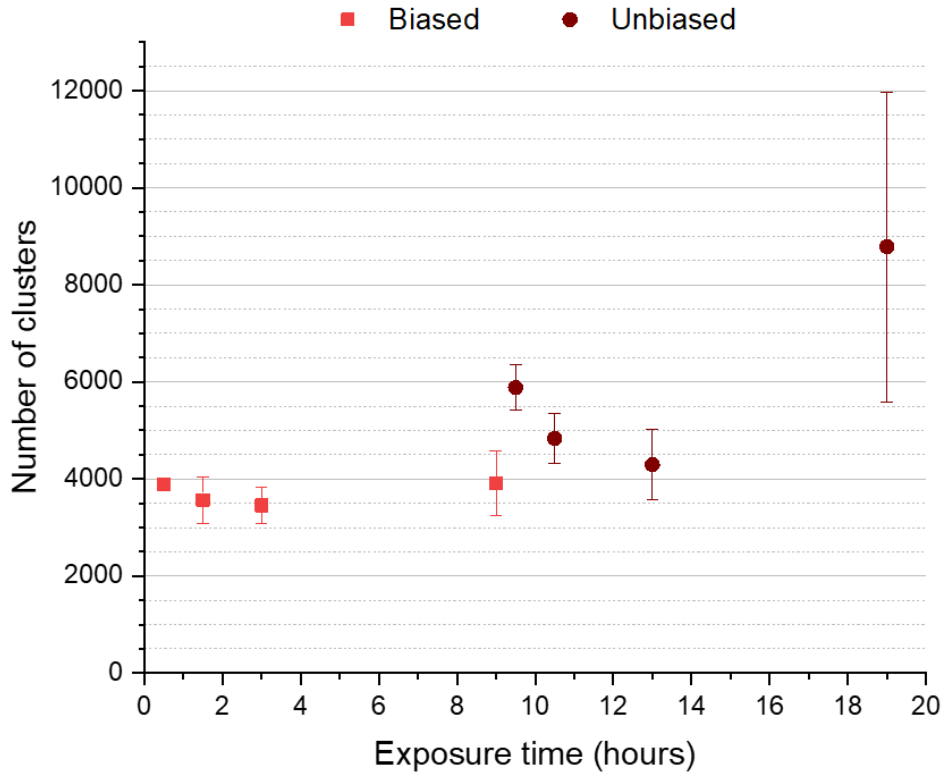


Figure 4.27 The number of bright pixels in a 30-s background measurement for the whole CCD imaging area over exposures to the ^{137}Cs source.

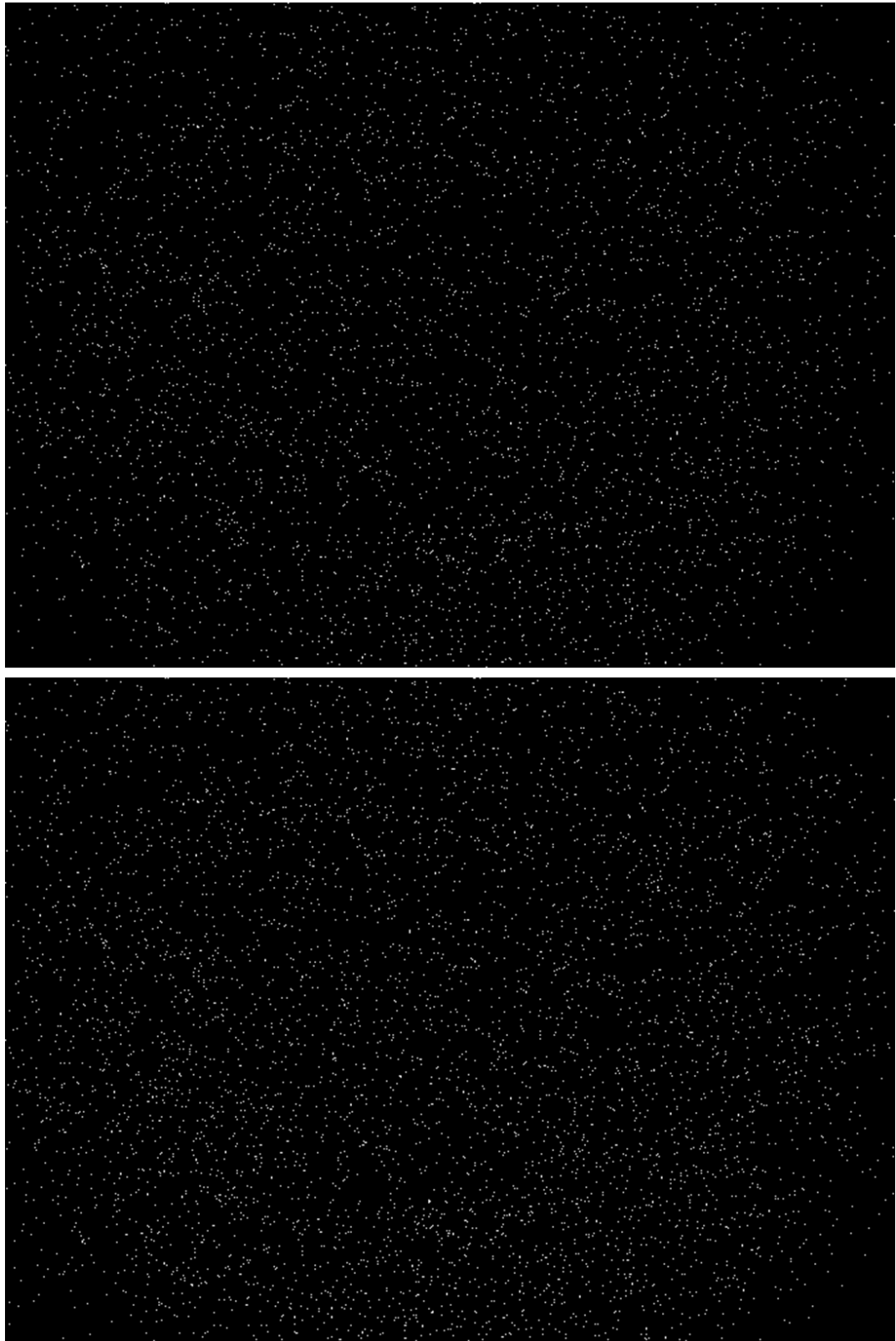


Figure 4.28 Example images of the 30-s background before irradiation (top) and after 19 hours exposure to the ^{137}Cs source (bottom).

4.5.2 Damage repair and mitigation

Multiple techniques have been considered to repair the damage from α radiation and mitigate its effects during exposure. These have consisted of annealing, cooling and image processing.

4.5.2.1 Annealing

Annealing at 100°C for 24 hours caused an $(89 \pm 28)\%$ reduction in the noise from one anneal, from (244 ± 52) clusters on average before the anneal, to (26 ± 6) clusters after the anneal. Example images can be seen in Figure 4.29. It was found that annealing is slightly less effective with each subsequent cycle, as not all of the damage is repaired.

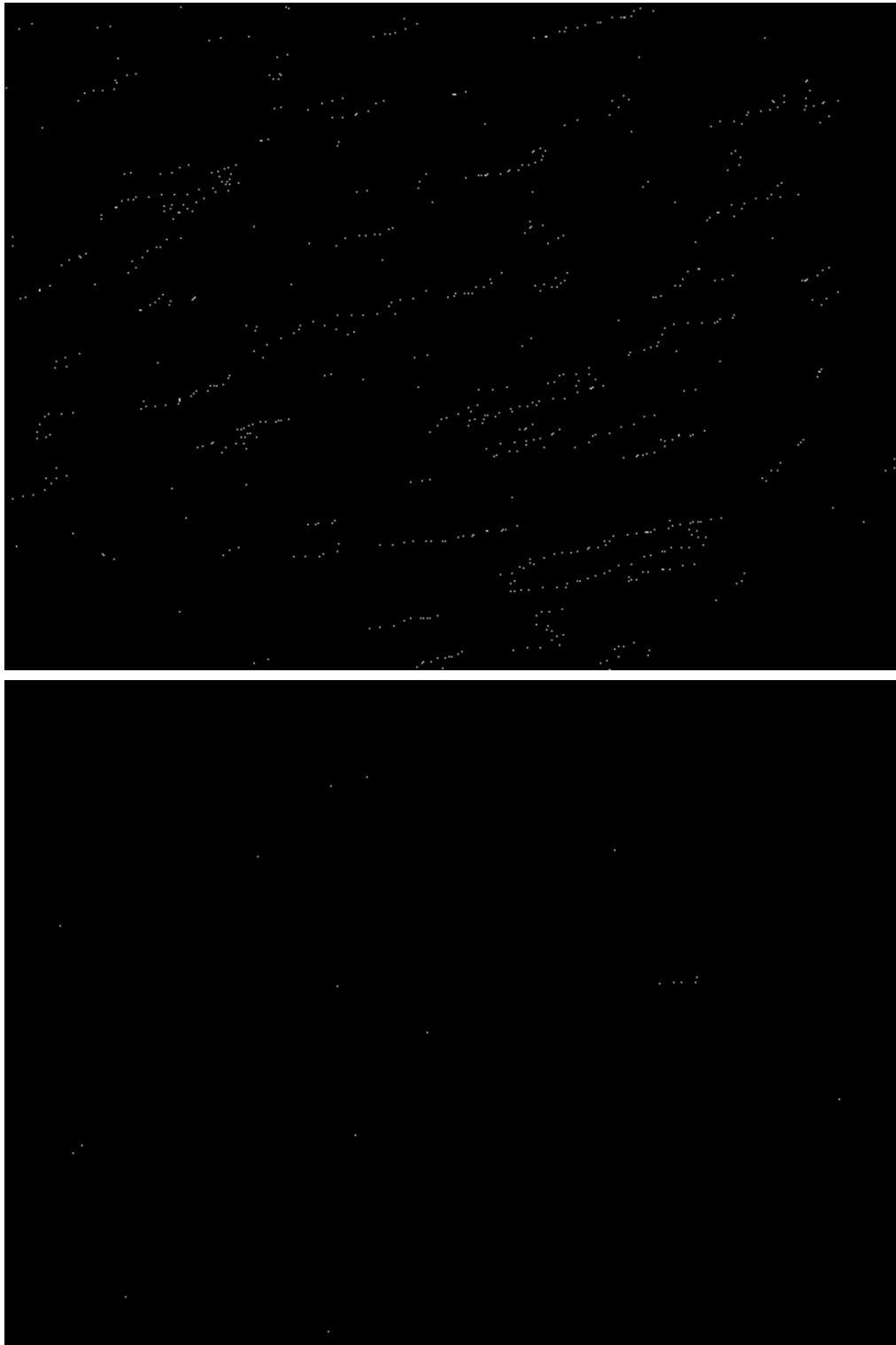


Figure 4.29 Examples of 5-minute exposures with no source present before (top) and after (bottom) a 24 hour anneal at 100°C. Pixels are highlighted to have the maximum intensity (255 ADU).

4.5.2.2 Cooling

The noise reduction from cooling with different combinations of the fan and heat pipe can be seen in Figure 4.30.

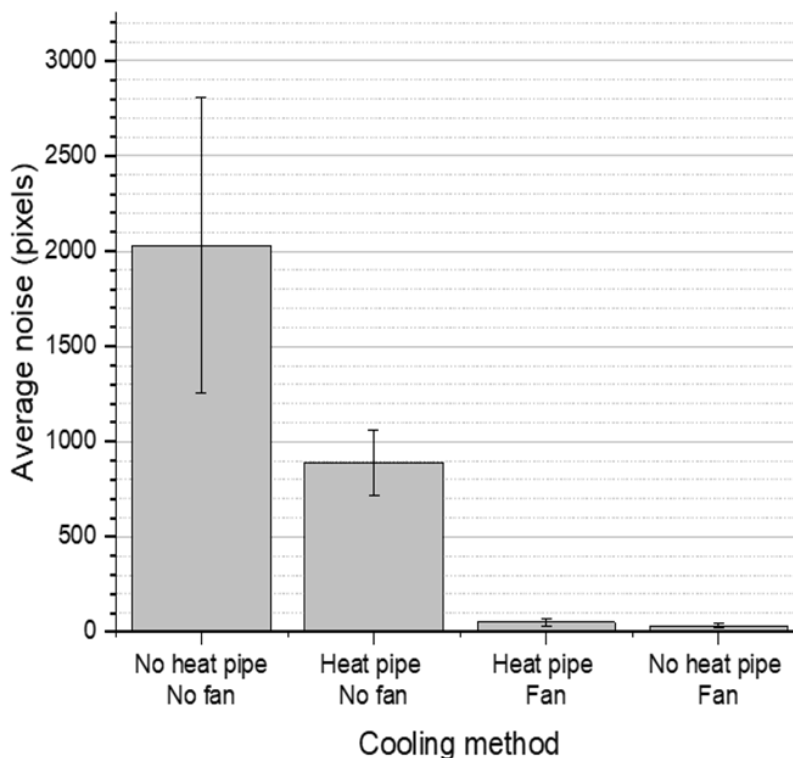


Figure 4.30 Average number of bright pixels (noise) in images produced by the CCD in 5-minute exposures with no source present at four levels of cooling: No cooling, just the heat pipe, both the heat pipe and the fan, and just the fan.

Using the heat pipe with no fan, the average noise per image reduced by $(56 \pm 19)\%$. If a fan can also be used then the noise can be reduced by $(98 \pm 1)\%$. Measurements were also taken of the fan cooling the CCD directly, and showed a reduction of $(98.3 \pm 0.8)\%$. Example sections of exposures with each type of cooling method are shown in Figure 4.31.

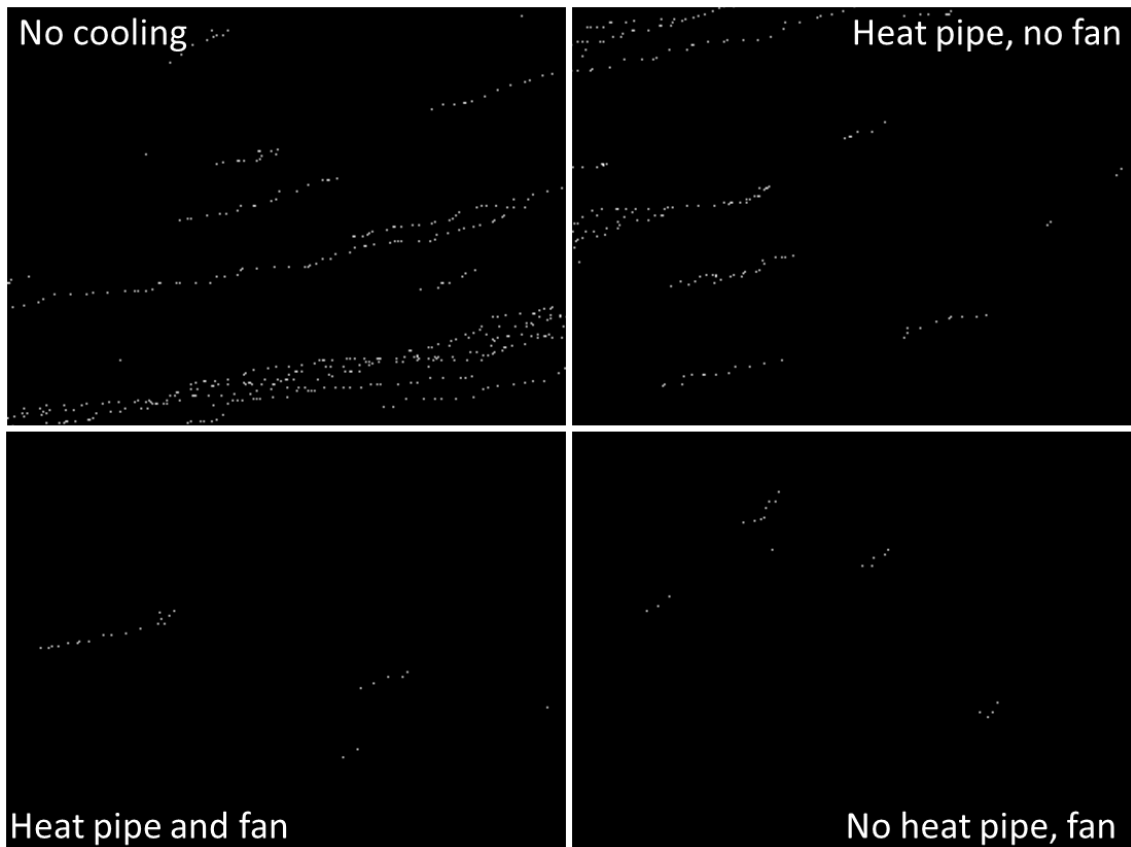


Figure 4.31 Example 348×260 pixel sections of 3-minute exposures with no source present for with different methods of cooling.

4.5.2.3 Image processing

A comparison of intensity images for noise alone and during an exposure to the ^{210}Po source is shown in Figure 4.32. The intensities of the brightest pixel in each cluster produced by noise, shown in Figure 4.24, were compared with the intensities of typical α -particle signals from Figure 4.17, to determine a cut-off intensity of 100 ADU for post-processing to remove noise clusters. For any cluster of pixels in which the brightest pixel has an intensity of less than 100, the entire cluster is removed. If any single pixel is over this threshold, the entire cluster is kept. This accounts for the low-intensity ends of the streaks caused by α radiation, so that no useful information is lost. Example images before and after processing can be seen in Figure 4.33.

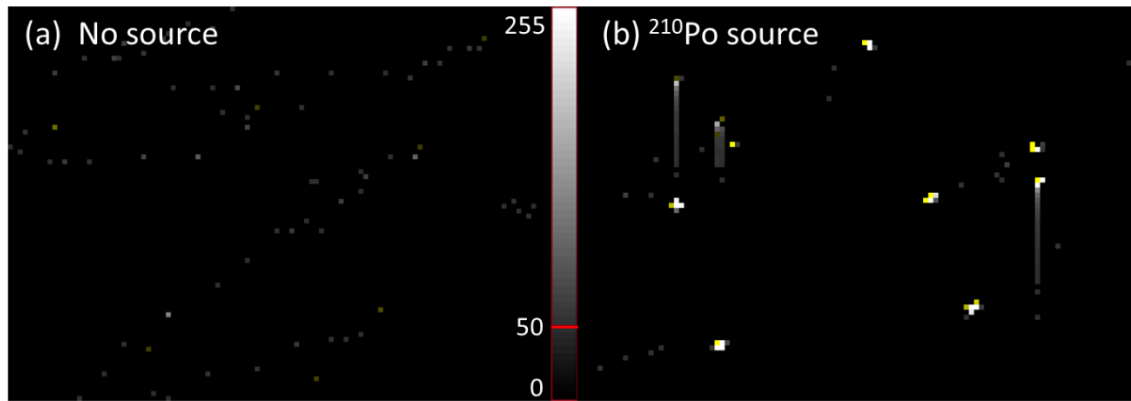


Figure 4.32 Example 110×80 pixel sections of exposures to (a) no source, showing just noise, and (b) the ^{210}Po source with both clusters and streaks from α particles. These images show the relative intensities of the pixels on a scale from 0 (black) to 255 (white). The software threshold is marked in red on the scale.

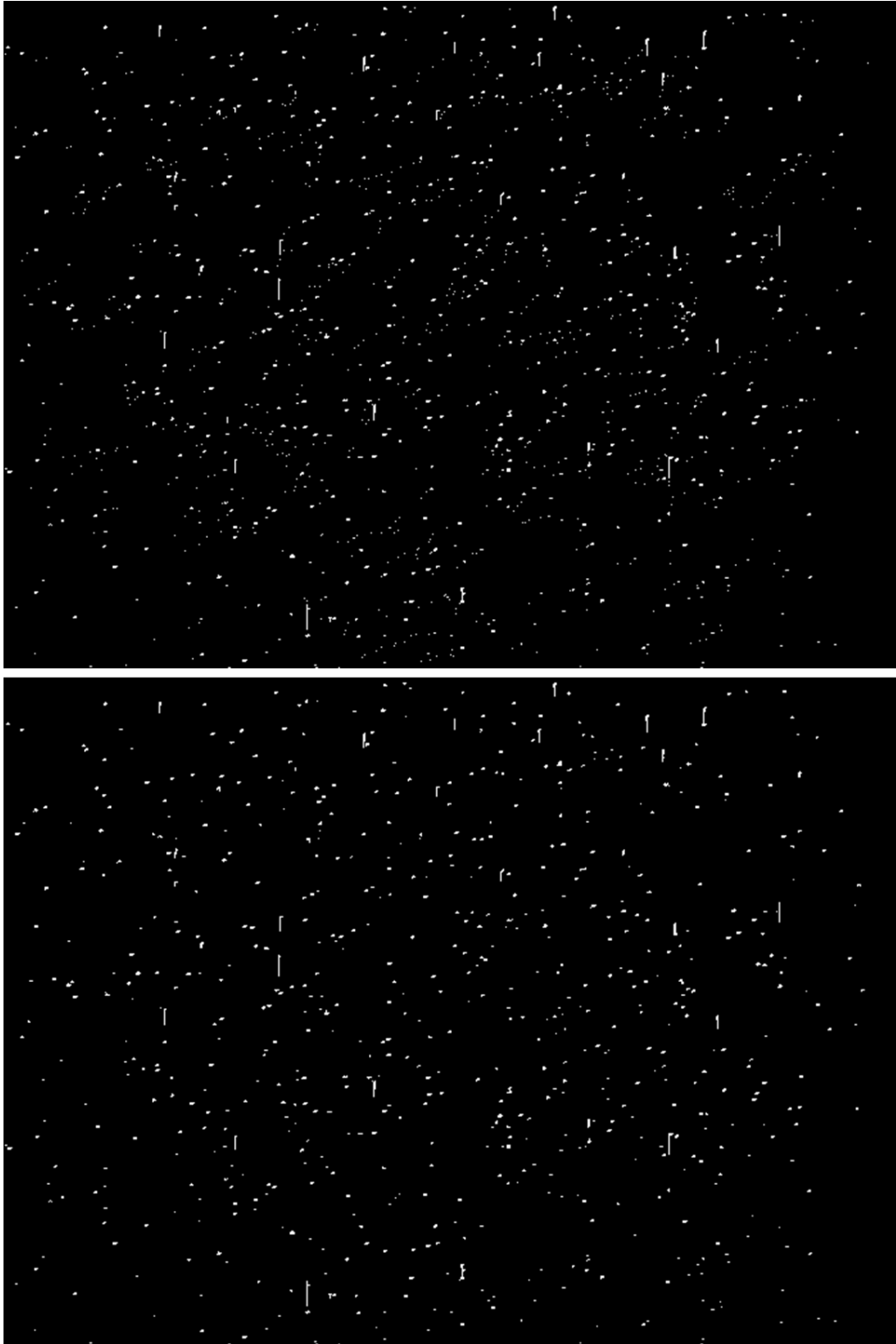


Figure 4.33 Example images of a 15-minute exposure to the ^{210}Po source with an activity of 19 Bq before and after image processing to remove the noise. The clusters have been highlighted to have the maximum intensity of 255 ADU for clarity.

4.6 References

- [1] J. F. Ziegler, M. D. Ziegler, and J. P. Biersack, “SRIM – The stopping and range of ions in matter (2010),” *Nucl. Instruments Methods Phys. Res. Sect. B Beam Interact. with Mater. Atoms*, vol. 268, no. 11–12, pp. 1818–1823, Jun. 2010.
- [2] H. Demers *et al.*, “Three-dimensional electron microscopy simulation with the CASINO Monte Carlo software.,” *Scanning*, vol. 33, no. 3, pp. 135–46, Jan. .
- [3] “LogNormal Fit Function,” *OriginLab*. [Online]. Available: <https://www.originlab.com/doc/Origin-Help/LogNormal-FitFunc>. [Accessed: 09-Nov-2019].
- [4] “Gaussian Fit Function,” *OriginLab*. [Online]. Available: <https://www.originlab.com/doc/Origin-Help/Gaussian-Function-FitFunc>. [Accessed: 09-Nov-2019].
- [5] “Allometric Fit Function,” *OriginLab*. [Online]. Available: <https://www.originlab.com/doc/Origin-Help/Allometric1-FitFunc>. [Accessed: 13-Nov-2019].

5 Discussion

5 DISCUSSION	120
5.1 The potential of CCDs for radiation detection and spectroscopy	121
5.1.1 <i>SRIM simulations</i>	121
5.1.2 <i>CASINO simulations</i>	123
5.1.3 <i>Experimental comparison with models</i>	126
5.2 Identification of radiation type	131
5.2.1 <i>Proof of the correlation between cluster shape and radiation type</i>	131
5.2.2 <i>Comparison of different radiation types</i>	134
5.3 Noise and radiation damage	143
5.3.1 <i>Noise increase</i>	143
5.3.2 <i>Radiation damage</i>	143
5.3.3 <i>Mitigation of radiation damage effects</i>	145
5.4 Comparison with existing technologies	149
5.5 References	151

This chapter discusses the results presented in Chapter 4. The first section considers the potential of using CCDs for performing the detection and spectroscopy of α and β radiation, through a comparison of the simulations and the experimental results. Properties of the clusters produced by the different types of radiation, including γ radiation, neutrons and tritons, are then discussed, to allow for the identification of the type of radiation being observed. The third section discusses the damage caused by interactions of radiation within the CCDs, and the development of the device to mitigating

problems induced by this damage. Finally, the CCD as a radiation detector is compared with existing technologies.

5.1 The potential of CCDs for radiation detection and spectroscopy

5.1.1 SRIM simulations

5.1.1.1 Detecting α particles from ^{210}Po

All of the α particles simulated to be from the ^{210}Po source are stopped with a maximum depth of 17 μm into the active layer within the CCD after passing through all of the prior layers, for both gate thickness estimates, using data from Figure 4.2. They should therefore all be detected with the maximum number of charge carriers produced within the active layer. This 17 μm thickness is amongst the thinnest of active layers within front-illuminated CCDs as discussed in Section 3.2.1, indicating that even if the estimates of the CCD layer depths are not accurate the α particles should all still be detected. In the event that the active layer is thinner than this, the α particles will definitely be stopped within the substrate layer, where most of the charge carriers should diffuse and be collected, but some of this evolved charge may be lost.

5.1.1.2 Energy loss determination

As the Mylar is the site of the greatest energy loss prior to the active layer, the estimates made for the thicknesses of the gate structure will have a minimal impact on this energy loss. This was confirmed by the simulations of energy loss prior to the active layer using thin and thick estimates for the gate structure, which made a difference in the energy loss calculations of 200 keV, increasing the energy loss from 1.4 MeV to 1.6 MeV. This only consists of 14% of the total energy loss. Therefore, any errors due to the estimates of the CCD layer thicknesses are anticipated to have a minimal effect compared to the thickness of the Mylar film, which has been measured.

The energy loss in the Mylar film cannot be avoided as the film is required to block the light from interacting with the CCD. Using a single layer of film is not sufficient for this task, as some light is able to pass through one layer of film to be detected by the CCD. Therefore, using two layers gives the minimum possible thickness. Alternative methods of detecting α radiation involve the use of dark chambers so that no film covering is needed, however these require isolating the contaminated item, and make the detector setup less readily portable for use *in-situ* [1]–[3].

5.1.1.3 Spectroscopy potential with α radiation

The simulated range and energy loss data, as given in Table 4.1, shows that the CCD has the capability to detect radiation from a variety of α sources. If the source of the radiation is directly in contact with the Mylar film, it is still feasible for α particles with some of the lowest energies to penetrate the active layer of the CCD, and so be detected. However, much of the energy is lost, on average 2.211 MeV of the total 2.232 MeV simulated. The range of (1.01 ± 0.03) mm is also spread such that not all of the α particles will be detected in the active layer which starts at 1.008 mm in the model. This means there can be partial detection of the radiation associated with these low-energy sources, but the count rate will be lower and the energy information less precise. The clusters and streak lengths should be smaller, as fewer charge carriers will be produced to overflow into the surrounding pixels. With a small air gap between the source of the α radiation and the Mylar covering, such as with the ^{210}Po source structure, it is anticipated that these low-energy α particles will lose even more energy and thus fewer will reach the active region.

The ^{210}Po source is discussed above, representing the most common α -particle energies between 4-6 MeV. For the higher energies, it is anticipated that the interactions of these α particles will extend further into the active region. The greatest range for α particles with an energy of 8.748 MeV is for the simulation in direct contact with the Mylar,

extending (1.057 ± 0.001) mm through the model. This corresponds to a range of (49 ± 1) μm into the active region. For the simulated active region, having a thickness of 60 μm , it is anticipated that all of the remaining energy of 7.951 MeV will be detected. However, this is an estimated depth and, in the situation where the active region is thinner than the 49 μm range, the α particles will still deposit the maximum possible amount of energy in the active layer, but there may be more charge in the substrate to diffuse into the surrounding area. This should still give a larger cluster size than the lower energy pixels, and be more likely to generate streaks through blooming, though there will be a greater charge transfer inefficiency so that not all of the charge carriers produced may be collected or transferred.

Therefore, on the basis of the SRIM simulations it is anticipated that a broad range of α -particle energies are detectable, and that their approximate energies should be identifiable based on the cluster sizes, streak lengths and number of streaks produced. However, specific energy information will be lost at the very highest and lowest energies, and the number of counts at low energies will not be sufficiently reliable to estimate the activity of the source. For the most common α -particle energies around 5 MeV, such as that from ^{210}Po of 5.304 MeV [4], there should be a full collection of information, if the CCD is within approximately 3 mm of the source.

5.1.2 CASINO simulations

5.1.2.1 Detecting β^- particles from ^{60}Co and ^{137}Cs

As the simulated electrons scatter through multiple pixels, interacting within each pixel, this suggests that a characteristic trail of charge should be left by each β^- particle passing through the CCD, which is seen experimentally. A small percentage are scattered back out of the CCD and may not deposit enough energy to be detected. This is 7.2% for the simulated electrons with energies representing ^{60}Co and 1.3% for those representing

^{137}Cs . All of the remaining β^- particles will pass through to the substrate layer and, as such, the majority of incident β^- particles should interact with these devices. As lower-energy β^- particles will scatter more, as demonstrated in Figure 4.4, it would be expected that a greater number will backscatter, and so fewer will be detected.

5.1.2.2 Spectroscopy potential with β^- radiation

The potential for lower-energy electrons to scatter through more pixels than higher-energy electrons is due to the higher scattering cross section of lower-energy electrons relative to that of higher-energy electrons. This is because the scattering cross section is related to the inverse of the kinetic energy of the electron [5]. The actual number of pixels scattered through for each simulation is shown in Figure 4.5 and reproduced here in Figure 5.1 for clarity. Here it can be seen that, on average, lower-energy electrons yield a larger number of bigger cluster sizes, and a wider spread of cluster sizes.

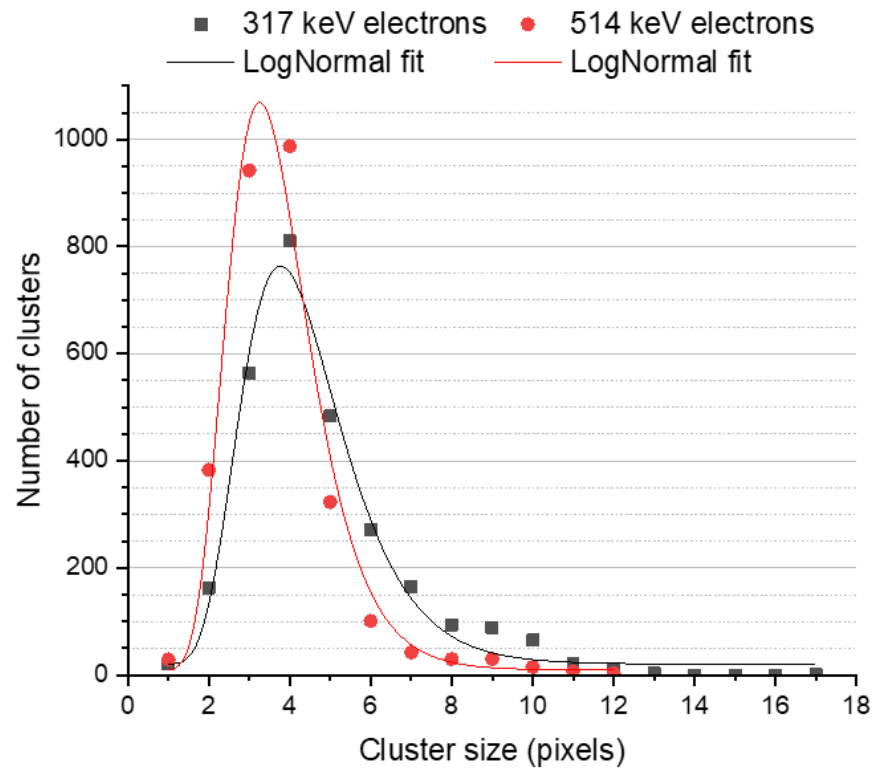


Figure 5.1 CASINO simulation data showing the cluster sizes for 10,000 electrons at two energies, 317 keV and 514 keV, passing through the active layer and substrate of the CCD. Reproduced from Figure 4.5.

LogNormal curves were found to be the best fit to these data. This is appropriate due to the cluster size being a result of many scattering stages within the CCD; a lognormal distribution occurs in situations that are the result of many small percentage changes, rather than absolute changes as it would be for a normal distribution [6]. As the electrons scatter through the medium, the scattering will be dependent on the energy of the electron, which will reduce with each scatter. The adjusted R^2 values of 0.9796 and 0.9597 for the lower and higher energies, respectively, indicate that these are good fits to the data. The difference between the fits for the two energies is significant, with centres at (4.19 ± 0.07) and (3.58 ± 0.09) respectively, showing that a distinction should be possible over a relatively small energy difference of 197 keV. With a wider variety of energies, a more pronounced

difference might be observable. This suggests that this CCD should be able to distinguish between high- and low-energy β^- radiation successfully.

5.1.2.3 Limitations of the simulations

There are several limitations of these simulations. Firstly, a single energy is simulated for each source, whereas β^- -particle sources produce a continuous spectrum of energies as discussed in Section 2.12. Secondly, there were some electrons that scattered outside of the simulated 10×10 pixel grid. Therefore, there may be larger cluster sizes than have been accounted for. Additionally, there may be errors from the method of counting the cluster sizes. The numbers of unique pixels passed through were counted to ensure cluster sizes were not extended incorrectly by counting the same pixel multiple times. However, the unique pixels were not necessarily in contact with each other, as electrons may have scattered into the substrate and back into a pixel which is not adjacent to the ones previously scattered through. This would be counted as a single track in the simulation, but experimentally this would appear as two, separate, smaller tracks. Finally, estimates have been used for the thickness of the active region. If the active region is deeper than that simulated, the electrons may scatter more creating larger cluster sizes. If the active region is shallower, the electrons will not be able to scatter through as many pixels or may backscatter more frequently into the active area from the substrate, creating multiple, smaller clusters.

5.1.3 Experimental comparison with models

5.1.3.1 The potential to perform α -particle detection and spectroscopy

As shown in the simulations, every α particle of sufficient energy should interact in the CCD to produce a signal. The uniquely large, round clusters, vertical streaks and bright intensities produced by these interactions experimentally are sufficiently distinct that every cluster can be identified. Therefore, every incident α particle should interact and be

able to be identified. This means that the devices may be used for detection of very low activity sources, as only a few α particles need to be detected for a user to be aware there is an α -particle source present. By the end of this research, the ^{210}Po source used had an activity of less than 20 Bq but could still be identified clearly as an α source within one minute of exposure time. If a source is of too great an activity, the interactions will fill the image with overlapping clusters, making it difficult to obtain any useful information as the processing used relies on separate clusters being produced. An example section of an exposure with overlapping clusters can be seen in Figure 5.2. In this case, shorter exposures can be taken. The QubiX Radiation Detector software used currently has a minimum exposure time of 1 s, however shorter exposures are possible with these devices. It should therefore be possible to detect a broad range of activities with these devices. The highest activity of the ^{210}Po used during this research was 356 Bq, for which 20 s exposures were commonly used, and the lowest activity used was 11 Bq, with 5 minute exposures.

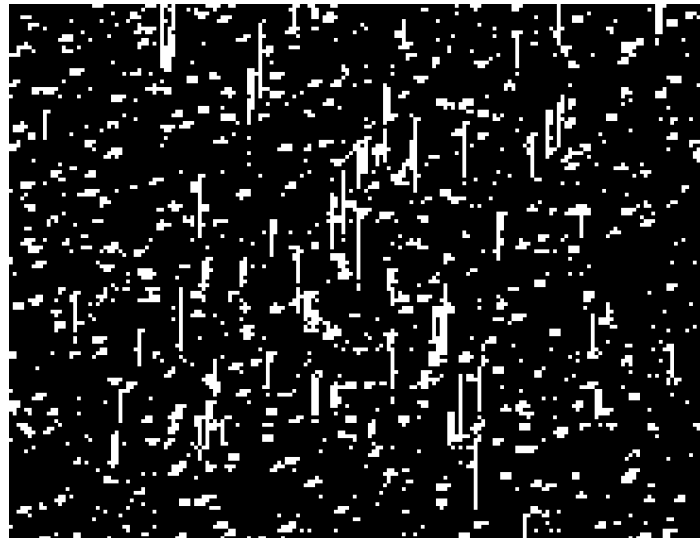


Figure 5.2 Highlighted 165×142 pixel section of a 2.5-hour exposure to the ^{210}Po source with an activity of 11 Bq, demonstrating overlapping clusters.

The cluster sizes produced by the ^{210}Po source form a Gaussian shape (qualitatively), neglecting cluster sizes of 1 and 2, as seen in Figure 4.14 and reproduced for clarity in Figure 5.3. The greater number of clusters at these small sizes may be attributed to noise and hence are not formed from the interactions of the α radiation. The adjusted R^2 value of 0.9789 indicates that this is a good fit. The peak of the cluster sizes is at 5 pixels. The SRIM simulations show that higher-energy α particles will generate a greater number of charge carriers than lower-energy α particles, which should lead to a greater amount of overflow into the surrounding pixels. Therefore, the peak cluster size should vary depending on the incident α -particle energy, providing a noticeable difference for higher- or lower-energy α particles.

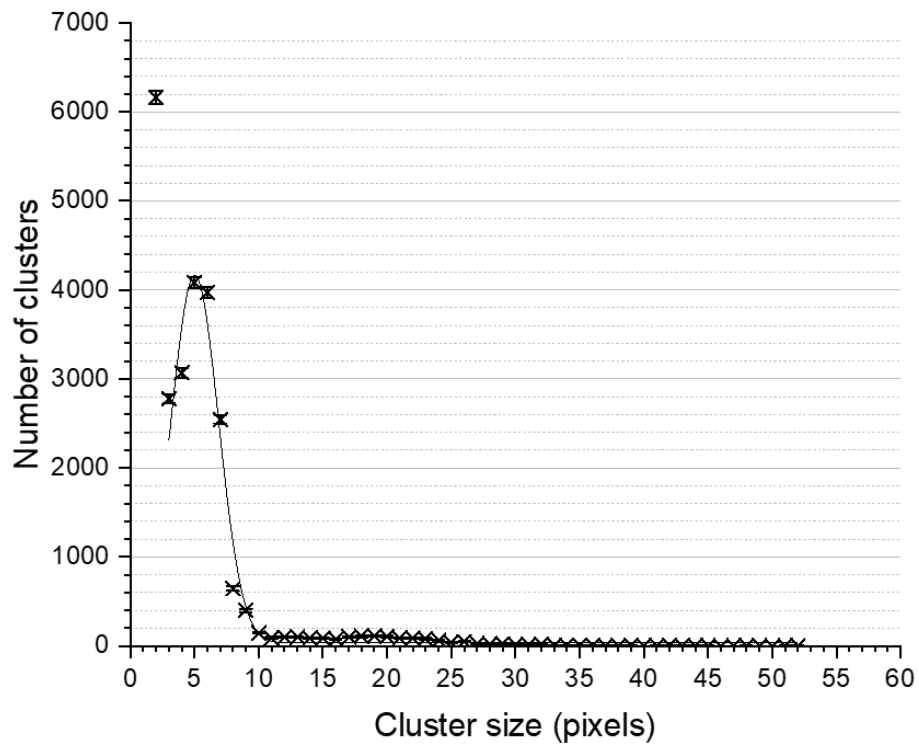


Figure 5.3 Cluster sizes for α particles produced by ^{210}Po . Clusters of 1 pixel were not included, with a value of 54,700. Reproduced from Figure 4.14.

The streak lengths produced by the ^{210}Po source do not form a noticeable peak in Figure 4.15 and, as such, accurate spectroscopy will be difficult to achieve with the current setup

using these lengths. It is still anticipated that, as with the overall cluster sizes, the lengths of the streaks will vary in relation to the energy of the α particles responsible for them. It is also possible that as the energy of the α -particle increases, the likelihood of blooms occurring will increase more than the current ratio for the ^{210}Po source of 1 streak occurring for approximately every 10 clusters. Further research should be done to determine the accuracy achievable via this approach, and to determine if higher-energy α particles will produce longer streaks as is hypothesised.

The most beneficial aspect of the streaks associated with the α -particle interactions is that they are remarkably distinctive, allowing α radiation to be identified quickly and with ease. In particular, humans are very capable of identifying these types of distinguishing features, allowing the user to identify the presence of α radiation quickly and confidently without the need for analysis [7]. While there may be some variation of the lengths of these streaks with different energies, the neat gaussian curve produced by the overall cluster sizes is more likely to provide viable spectroscopic information. Therefore, the importance of the streaks is associated with the quick identification of α radioactivity and as a means for the approximation of α -particle energy, but analysis using all of the clusters generated will be required for each spectroscopic study.

5.1.3.2 The potential to perform β^- -particle detection and spectroscopy

The larger, curved tracks created by the interaction of β^- particles with CCDs are distinctive and can be identified easily by a user. However, these constitute only a small proportion of the range of clusters produced by these sources. Therefore, longer exposures or additional analysis is required to be confident of the identification of β^- radiation and to assess its energy. The properties used to identify these clusters through image processing will be discussed in Section 5.2.2.

The cluster sizes produced by the ^{60}Co and ^{137}Cs sources show similar trends to the simulations, with the ^{60}Co source (which emits lower-energy electrons) producing on average larger cluster sizes. A comparison of the simulation and the experimental results can be seen in Figure 5.4. Lognormal distributions also provide consistent fits to these curves, with adjusted R^2 values of 0.9983 for the ^{60}Co source and 0.9996 for the ^{137}Cs source indicating that these are good fits to the experimental data in addition to the simulated data. The experimental peak centres are at (2 ± 1) and (1 ± 1) pixels respectively. They are therefore not statistically significantly different, unlike the simulation data. This suggests that the energy difference between these two sources is too small to distinguish experimentally. A wider variety of energies may still present a statistical difference, allowing for spectroscopy to occur, but not with the accuracy originally suggested by the simulations.

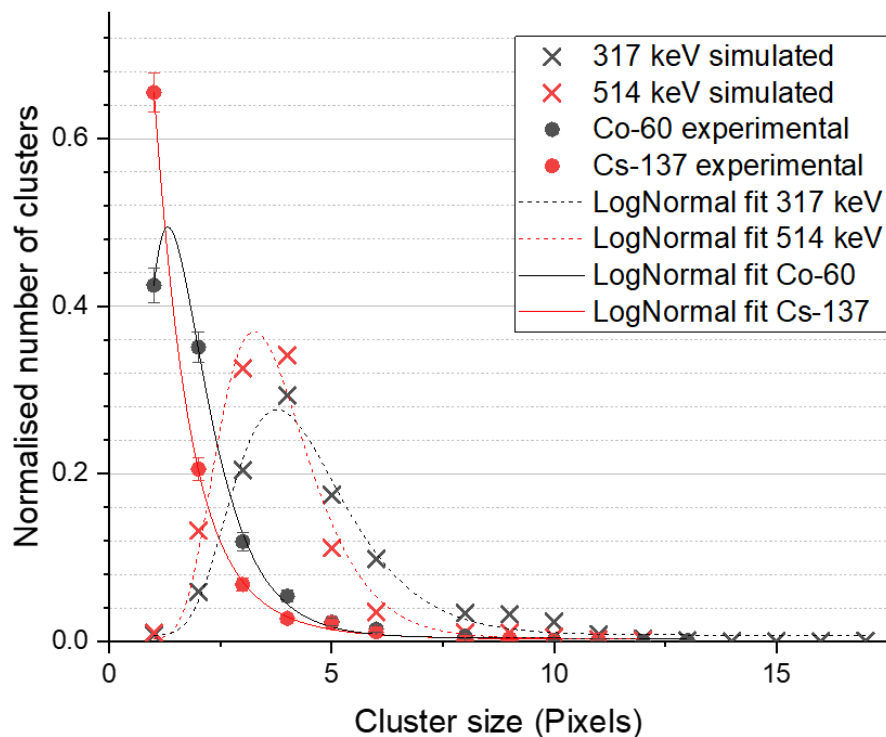


Figure 5.4 A comparison of the cluster sizes produced by experimental data for ^{60}Co and ^{137}Cs , and CASINO simulations of energies representing the β^- particles produced by these sources.

The peaks of the cluster distributions are shifted to smaller sizes compared with the simulations. There are several potential reasons for this. Many causes of these differences will be related to the simplifications and assumptions made by the model, as discussed in Section 5.1.2.3. The most significant of these affecting the peak shift are likely to be the single β^- -particle energy being simulated rather than the full, continuous spectrum, and the estimates made on the depth of the active region. As the average cluster sizes are shorter experimentally this implies that the active region could be thinner than the one simulated. Another cause may be the CCD threshold, as the lower intensity pixels will be removed. This will reduce the size of clusters or, if a low-intensity pixel occurs in the middle of a track, split them such that they appear to be multiple, smaller clusters.

The shift in the peaks and the smaller cluster sizes suggest that identifying β^- particles with a significantly higher energy than that associated with ^{137}Cs will be difficult, as the cluster sizes will become much smaller and thus it is harder to positively identify as β^- radiation or distinguish between different energies.

5.2 Identification of radiation type

5.2.1 Proof of the correlation between cluster shape and radiation type

Throughout the experimental research performed that is described in this thesis, there were situations providing proof of the type of radiation being analysed. Those experiments are discussed in this section for each of the radiation types considered and for noise produced after background subtraction when the CCD is exposed with no source present.

5.2.1.1 α radiation

When considering α radiation, the experiments performed in Section 4.5.1 showed that initially no signals were seen on the half of the CCD that was covered with card.

Therefore, all of the large, round clusters and streaks seen on the uncovered half must be due to the α radiation produced by the ^{210}Po source, according to the interaction properties as described in Section 2.1.5.1. As this source is almost a pure α -particle emitter, there is no potential for confusion with another radiation type.

5.2.1.2 β^- radiation

Similarly, when considering the two β^-/γ sources, the longer, curved tracks (which are to be expected from the simulations and initial images taken) are not observed when the CCD is covered with a 4-mm thick piece of aluminium, as detailed in Section 4.2.2. Some signals remain, but these are smaller and do not have the appearance of scattered tracks. Therefore, the curved tracks must be produced by the β^- radiation which was blocked by the aluminium.

5.2.1.3 γ radiation

Based on the interaction properties described in Section 2.1.5.1, it was expected that γ radiation would leave small clusters, primarily, likely to be only a single pixel in size. By covering the ^{60}Co and ^{137}Cs sources with aluminium sufficiently thick to block the β^- radiation, but thin enough to maintain greater than 90% of the γ -ray intensity, it was inferred that the remaining signals would be due to the γ radiation.

For the ^{60}Co source, the clusters are stopped almost entirely when the β^- -radiation is blocked. For ^{137}Cs , the total number of clusters observed decreases by approximately 90%. These decreases are much more than would be expected if all of the γ radiation produced by these sources was detected. As two γ rays are produced for 99.88% of the β^- particles emitted by the ^{60}Co source, the number of clusters detected would be expected to be reduced by approximately one third [8]. Similarly, one γ ray is produced for 94.4% of the β^- particles produced by the ^{137}Cs source, suggesting the number of clusters observed should be approximately half that seen with the uncovered device [8]. In both

of these cases, slightly fewer clusters would be seen than expected as the intensity of the γ radiation is reduced slightly by the aluminium. However, more than 90% of the intensity of the γ radiation was calculated to remain, which does not account for the number of counts being reduced significantly more than expected. It is also likely that there is some noise in these images, which cannot be distinguished from those signals produced by γ radiation.

Though there is a significant reduction in the number of counts seen, the shapes of the graphs in Figure 4.13 are similar both for the covered and uncovered cases. This suggests that the signals from γ radiation that are detected may be due to electrons produced by Compton scattering in the aluminium, some of which would be incident on the CCD and produce similar signals to those from β radiation, rather than signals caused by γ radiation directly ionising the active layer in the CCD.

The discussion above demonstrates that the CCD is not very sensitive to γ radiation. This is beneficial if using the device to study β^- radiation specifically, which is often produced alongside γ radiation, as the clusters observed are more likely to be from the β^- particles than from a γ ray. It will also minimise the number of unwanted signals observed when looking for α radiation in a mixed-field environment. However, as the potential to detect some γ radiation still exists, this possibility cannot be neglected entirely when considering cluster sizes and count rate.

5.2.1.4 Neutrons and Tritons

Finally, for the clusters produced by the products of the interactions of neutrons with the ^6Li -enriched crystals, SRIM simulations indicate that it is most likely to be the tritons from these interactions which are being detected primarily, rather than the α radiation or the neutrons themselves. As the α particles produced have an energy of 2.05 MeV [9], a significant amount of this energy will be lost in the Mylar film layers. As the SRIM

simulations show in Table 4.5, α particles of this energy will have a range of (1.01 ± 0.03) mm and so not all will penetrate through to the active layer of the CCD at a depth of 1.008 mm. They will also have lost the majority of their energy before reaching this layer, an average of 2.043 MeV. This also assumes the α particles are released from the edge of the lithium crystal. More energy will be lost within the crystal if the α particle is produced away from the edge. Barely any of the α particles will have the range to interact in the active region of the CCD, whereas it is calculated that all of the tritons, produced with 2.75 MeV [9], will reach this layer with only a small energy loss of ~ 360 keV. Therefore, all of the tritons produced should be detected. As no streaks are observed, as is typical with α radiation, this reinforces the conclusion that the majority of clusters seen are due to the triton which is produced in the $n(^6\text{Li}, \text{T}^+)\alpha$ reaction, rather than the α particle.

5.2.1.5 Noise

Noise is inherent to the response of the CCD, and therefore it can be evident in exposures taken in the dark with no radioactive source present. As there is no external source of ionisation and a background subtraction is performed, the image produced should be completely black, and any clusters that arise will be a result of additional noise. Some signals may be seen from effects due to cosmic radiation, but these are very unlikely over the timescales of the exposures typically used in this research, most commonly ranging from 2-s to 5 minutes [10].

5.2.2 Comparison of different radiation types

There is a distinctive difference between the pixel clusters produced by the CCD interacting with the α source and the two β^-/γ sources. Example image sections focusing on these features can be seen in Figure 5.5 and Figure 5.6. It can be seen that α particles produce large round clusters from diffusion through the substrate layer and vertical

streaks from blooming, as expected. As α particles will cause so much ionisation in a single pixel within the CCD, it is anticipated the pixel will reach its full well capacity, creating diffusion and consistent with the blooming effects as described in Section 2.2.2.4 [11]–[13].

In contrast, β^- radiation will produce much smaller clusters as it is less interacting and so will cause less ionisation within the CCD. As can be seen in the CASINO simulations in Section 4.1.2, it is feasible for β^- particles to scatter through several pixels, creating curved trails which are clearly seen in the experimental images produced by the CCD. As γ radiation is very weakly ionising, most of these photons will pass through the device creating single-pixel spots or without producing enough charge carriers to cross the pixel intensity threshold set by the software, hence leaving no signal at all, as discussed in Section 5.2.1.3.



Figure 5.5 A highlighted 246×165 pixel section of a typical 60-s exposure to the ^{210}Po source.

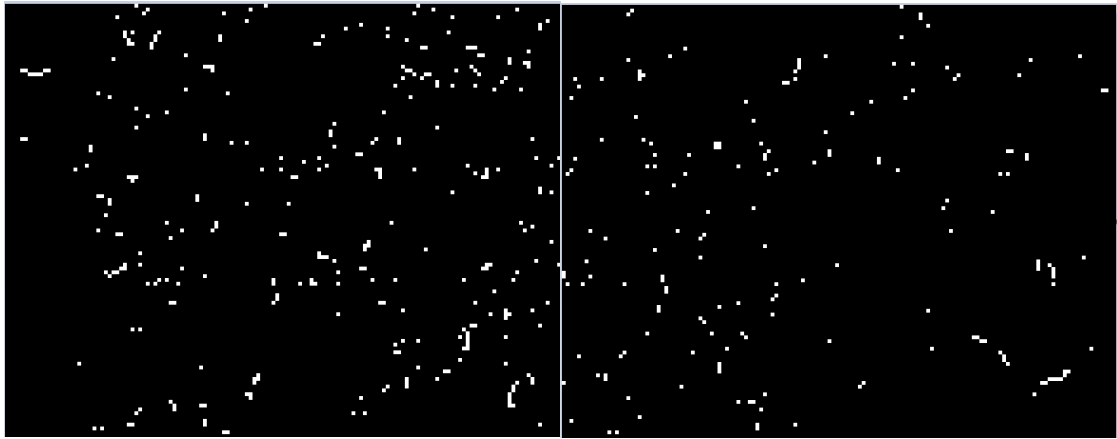


Figure 5.6 Highlighted 146×114 pixel sections of typical exposures to the ^{60}Co (left, 5-s exposure) and ^{137}Cs (right, 1-s exposure) sources.

5.2.2.1 Detecting neutrons

As described in Section 5.2.1.4 it is likely that the majority, if not all, of the signals produced in the CCD when exposed to the ^{252}Cf neutron source with a covering of ^6Li -enriched crystals are from the interactions of the tritons from the $n(^6\text{Li}, \text{T}^+)\alpha$ reaction with the CCD, rather than the low-energy α -particles. The tritons exhibit similar characteristics to signals produced by α -particle interactions, by producing enough charge carriers to overflow into large, round clusters. These clusters can be recognised by a user, but more clusters will be required for a confident identification of the presence of neutrons as they are not unique as in the case of the streaks produced by α radiation.

Similar to α radiation, a Gaussian curve fits to the cluster size data, with a good adjusted R^2 value of 0.9952. The larger errors in these data are due to the smaller number of clusters analysed. The intensities of the brightest pixels in each cluster also follow a similar pattern, but only 29% of the clusters contain a pixel of maximum intensity, significantly fewer than are observed for the ^{210}Po source. Some of these differences may be due to the lower energy being detected, but it is also likely they are due to tritons being

less interacting than α -particles of the same kinetic energy because of their smaller charge, as per the stopping power dependence with energy described by Equation 2.6.

This method of detecting neutron radiation also ensures there is no confusion between particles produced by interactions with the lithium and those from external α -particle sources. The lithium crystals will stop any α particles produced externally, meaning that any clusters seen which can be identified as being produced by an α particle or triton must be from neutron interactions in the lithium, notwithstanding the potential for there to be trace quantities of α -emitting contamination i.e. uranium in the detector materials and lithium crystals. However, the rate of interaction between the neutrons and the ${}^6\text{Li}$ is quite low and therefore longer exposures may be required to identify a neutron source confidently than is necessary for a similar-activity α - or β^- -particle source.

5.2.2.2 Comparing cluster sizes

The sizes of the clusters produced by the four radiation types explored in this research and those produced by noise have been normalised and are compared in Figure 5.7. Large cluster sizes, i.e., between 15 and 55 pixels, have not been included for ${}^{210}\text{Po}$ so that the comparison can be seen more clearly. The peak of α -particle cluster sizes for ${}^{210}\text{Po}$ appears smaller by comparison due to the large number of noise signals in the data. The first three data follow a power-law equation with the same power used in the fit for noise with an adjusted R^2 value of 0.9981, as shown in Figure 5.8, confirming that this peak is due to noise. The centres for each of the peaks are given in Table 5.1. The centres for the two β^- sources and the neutron source with lithium crystals are not significantly different from each other, but the different fits can provide some distinction between the different types of radiation. The centre for the ${}^{210}\text{Po}$ clusters are significantly different from these, allowing the use of the cluster size alone to identify the presence of this source. The noise

also has a distinctive fit for the cluster sizes produced, which can allow it to be separated from data of interest, as was done with the ^{210}Po data in Figure 5.8.

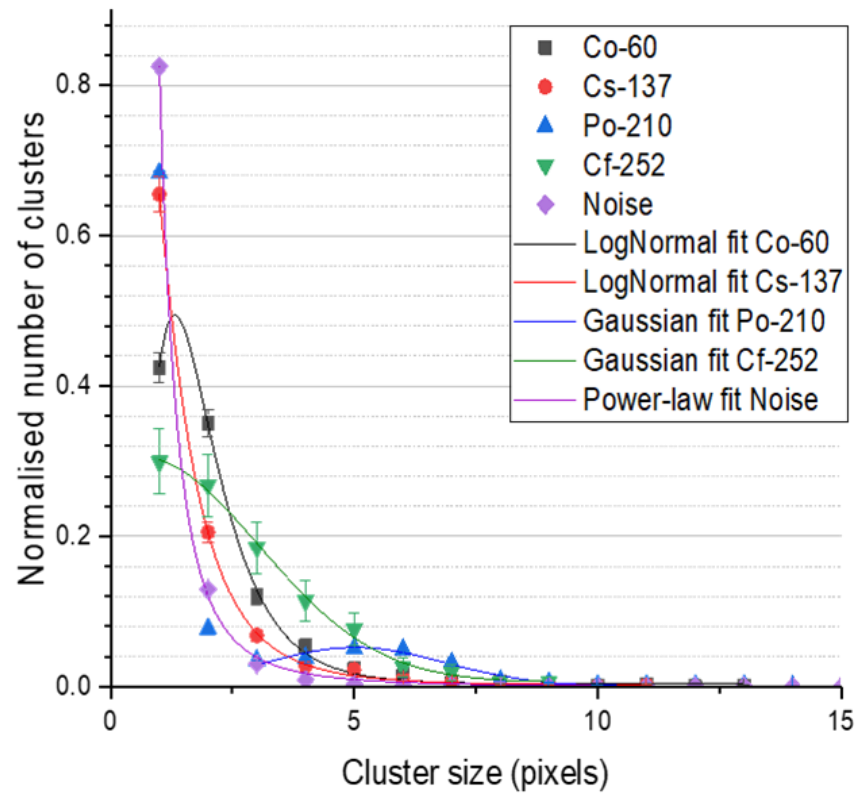


Figure 5.7 A comparison of the cluster sizes produced for each of the radiation types studied in this research and for noise when no radiation is present. The ^{210}Po data continued the trend up to a cluster size of 55 pixels, but have not been included so the peaks can be seen more clearly. Where error bars cannot be seen they are smaller than the symbols used for the data points.

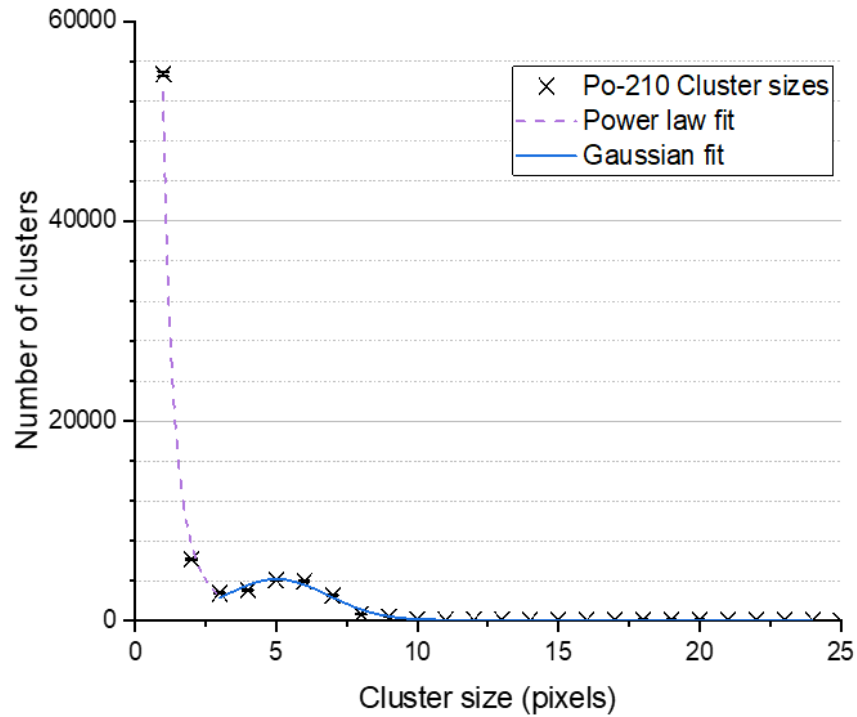


Figure 5.8 Cluster sizes up to size 25 for exposures to the ^{210}Po source. A power law fit has been applied to the first three data points, and a Gaussian fit to the remaining data points.

Table 5.1 Peak centres and standard deviations for clusters produced by radiation from the four different sources considered.

Source	Peak centre (pixels)
^{60}Co	2 ± 1
^{137}Cs	1 ± 1
^{210}Po	5 ± 2
^{252}Cf	1 ± 2

5.2.2.3 Comparing intensities

A comparison of the intensity graphs (Figures 4.13, 4.17, 4.21, and 4.24) clearly shows that α particles and tritons produce a larger number of bright clusters, whilst β^- radiation and noise both produce lower intensity clusters. This can be used to distinguish α particles and tritons from noise in particular, as the signals have minimal overlap as shown in Figure 5.9. An intensity threshold of 100 ADU is chosen to include 99% of the clusters produced by α particles, whilst excluding 98% of the clusters produced by noise. A similar analysis shows an intensity threshold of 100 ADU will also account for 93% of the clusters produced by tritons.

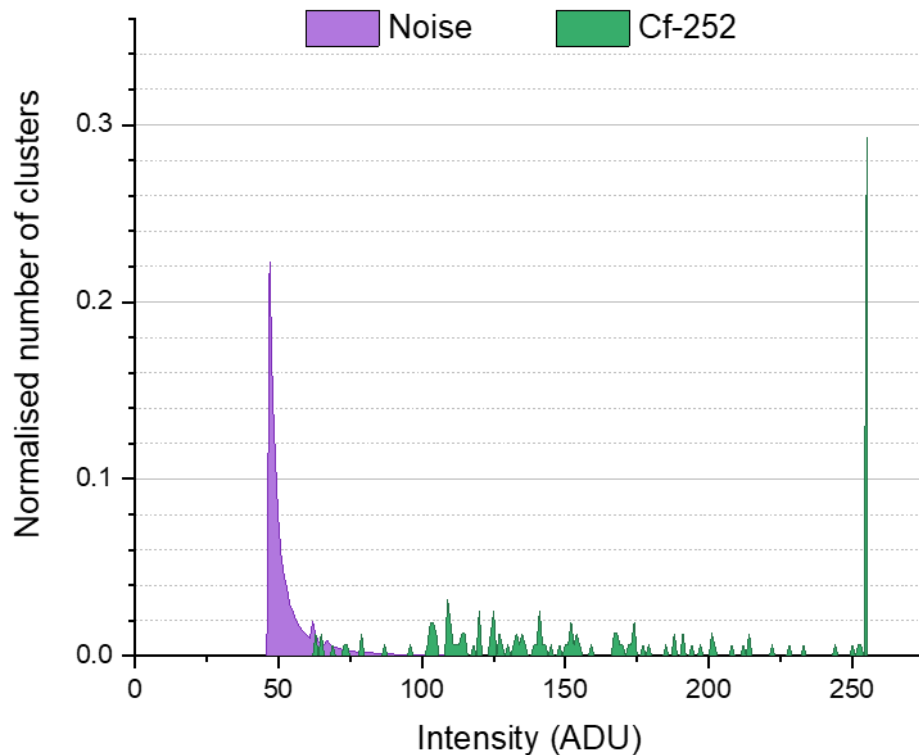


Figure 5.9 A comparison of the intensities of the brightest pixel in each cluster produced by noise and by particles produced in the interactions of neutrons from ^{252}Cf with ^6Li . The total number of clusters has been normalised for each source.

Two peaks were seen in the intensity graphs for ^{60}Co and ^{137}Cs , Figure 4.13. The ^{137}Cs data have been compared with the noise intensity data in Figure 5.10, with the noise

normalised such that the lowest intensity for each dataset has the same number of clusters. It can be seen that the first peak in the ^{137}Cs data is very similar to the noise data. It is expected that there should be noise in these images due to the level of damage when these images were taken, suggesting that based on Figure 5.10 the noise and the β^- radiation produce distinctive peaks. This could allow for discrimination between noise and β^- radiation, which is not easily done based on cluster size alone as both will produce a considerable number of 1-pixel clusters. Based on Figure 5.10, all β^- particles will produce clusters with an intensity greater than 70 ADU. In addition to this, as only 0.2% of the β^- particles have the maximum intensity of 255, it can also be said that if a cluster has a pixel of this intensity it is unlikely to be from β^- radiation, allowing for greater distinction between α and β^- radiation.

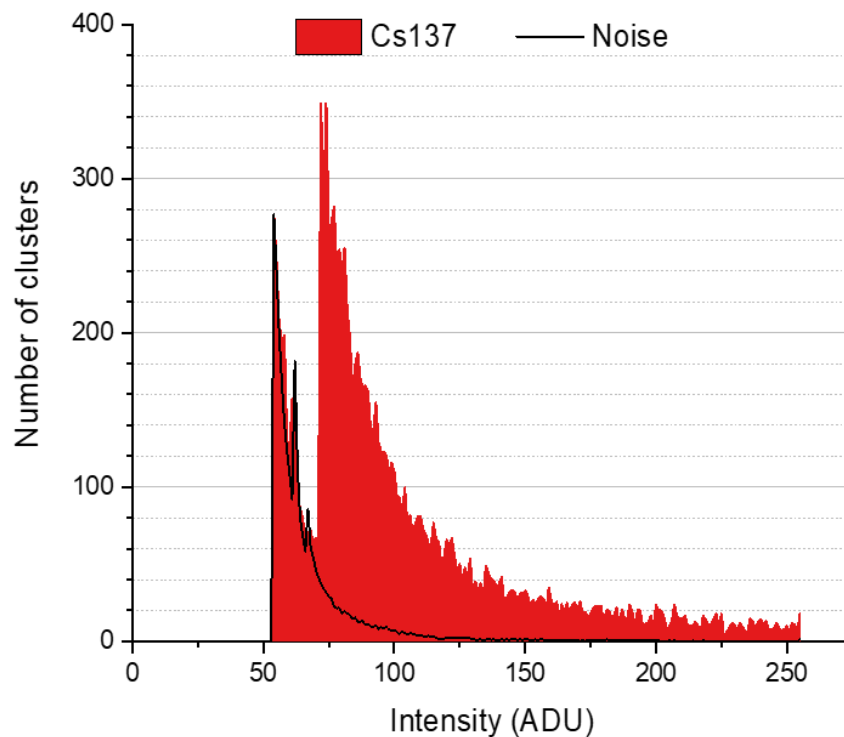


Figure 5.10 A comparison of the intensities of the brightest pixel in each cluster for ^{137}Cs and noise. The noise data have been normalised to the height of the first peak in the ^{137}Cs data.

5.2.2.4 Properties for identifying radiation type

By using information from the previous sections, properties pertaining to the detection of each of the radiation types and to noise were determined, as detailed in Table 5.2. To determine a streak, the criterion used is that the vertical height of the cluster is greater than 5 pixels, based on observations of the α -particle exposures that the round clusters are usually not longer than 5 pixels in height.

Table 5.2 Properties to identify different types of radiation and noise within the CCD. The CCD is not sensitive to γ radiation and so this cannot be identified.

Properties	α	T ⁺	β^-	Noise
Cluster size (pixels)	>3	>1	>1	<3
Cluster size fit	Gaussian	Gaussian	LogNormal	Power law
Streaks observed	Yes	No	No	No
Intensities (ADU)	>100	>100	>70, <255	<100
Clusters with a pixel of maximum intensity (%)	92%	29%	<1%	0.05%
Bounding box fill (%)	>50%	>50%	<50%	>50%

These properties will allow a user to determine which type of radiation is present from a single source of α particles, β^- particles and tritons. In a mixed-field environment with γ radiation, this identification will still be possible as the CCD is not very sensitive to γ rays. In situations where multiple types of radiation are present, clusters produced by α

particles and tritons ought to be readily distinguished from those produced by β^- particles or noise. It will be more difficult to distinguish between clusters produced by α particles and those produced by tritons in real time as the round clusters produced are similar. Similarly, there are some overlapping properties for β^- radiation and noise. By later processing the images produced and performing full analyses of cluster size and intensities, the different types of radiation can be confidently identified.

To identify neutrons, a lithium covering is required and the α particles and tritons produced can then be detected using the properties in Table 5.2. There should be no interference from any additional sources of α -particles or tritons as these particles would be stopped within the lithium covering.

5.3 Noise and radiation damage

5.3.1 Noise increase

Over time, the CCD images became noisier, with a greater portion of low-intensity 1-pixel clusters being produced both in the presence of radioactive sources and without. Initially, this noise was not associated with radiation damage, as the noise was observed to fluctuate. This led to the development of the device configuration to minimise noise fluctuations, as detailed in Section 3.1.2.2. After the instabilities were resolved by removing the wires connecting the CCD to the electronics, noise still remained. It was at this point that the possibility of radiation damage was investigated.

5.3.2 Radiation damage

The simulations in Section 4.1.1 show that α radiation does cause damage in CCDs. That the damage events caused by the α -particle interactions occur primarily in the active layer, as demonstrated in Figure 4.3, is to be expected due to this layer also being the primary location for energy loss of the α particles. The simulations show that some recombination

occurs, but only for 7.6% of the total displacements. These displacements can lead to traps, generating noise and charge transfer inefficiency as discussed in Section 2.2.4.2 [14]–[16]. This information indicates that α radiation is a strong candidate for causing the additional noise seen in the CCDs over time, leading to the experimental investigation on the effects of α radiation, and also of β^- radiation for comparison.

These experiments show that the α radiation causes a significant increase in the noise, detailed in Figure 4.25 and reproduced here in Figure 5.11. It can clearly be seen that the uncovered side of the CCD which could interact with radiation has had a significant increase in the background over the 5-hour period. Conversely, the covered side did not see any significant increase in the background. Therefore, the α radiation must be causing this damage. This agrees with the SRIM simulations and prior art, as discussed in Section 2.2.4.2.

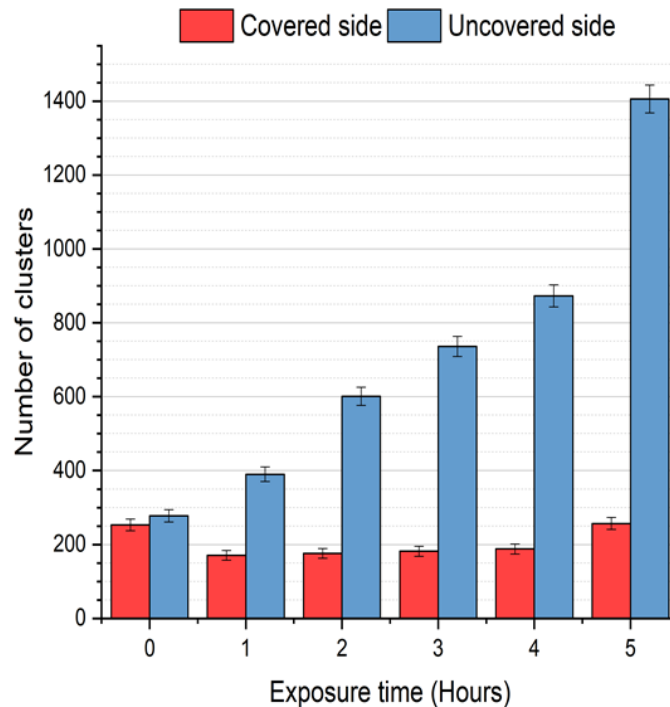


Figure 5.11 The number of bright pixels in a 30-s background measurement for equivalent sized sections on the covered and uncovered side of the CCD after each additional exposure to a ^{210}Po source. Reproduced from Figure 4.25 for clarity.

An increase in background signals is not seen with the ^{137}Cs β^-/γ source, as indicated in Figure 4.27. As the α source created a more significant increase in background noise, this is consistent with displacement damage from the heavier particles causing the traps which lead to an increase in noise. In contrast, damage caused by ionisation which would be seen with both sources has a much smaller effect which would only become a concern with very long exposures of several hours for the activity of sources used in these experiments. Both types of damage would be of a more significant concern with source activities several orders of magnitudes larger, but for these only very short exposures would be needed, minimising the opportunity for damage to build up.

5.3.3 Mitigation of radiation damage effects

5.3.3.1 Annealing

By annealing the CCDs at 100°C for 24 hours, an obvious reduction of noise can be seen in the images produced, as in Figure 4.29. The noise can vary between exposures of the same length of time, and so averages before and after the anneal were compared to give a reduction of $(89 \pm 28)\%$, where the large error is due to the variation in noise for each exposure. This annealing process selected is a compromise between effective damage repair and practicality. A user may choose to anneal for a longer time, allowing for a greater proportion of damage to potentially be repaired, but the device would be unavailable for use for that additional period of time, as well as the time required for the CCD to return to room temperature and stabilise. In addition to this, the user may separate the CCD from the device and anneal at a higher temperature, to repair a greater variety of the traps formed. Although a recommended anneal is given, these possibilities give flexibility depending on the preferences of the user. If the lithium covering is being used for neutron measurements, this should be removed before annealing the CCD.

As the annealing is less effective with each subsequent cycle, eventually the level of noise remaining would still pose a problem. In this situation the CCD could be annealed at a higher temperature or for longer periods of time, or else the CCD has reached its useful lifetime. However, this should only occur after a significant amount of exposure, making the lifetime of the device dependent on the application used. For example, for general monitoring purposes α radiation would not often be detected, giving a very long overall lifetime. However, if the CCD is used regularly in high-activity α radiation environments, as may be possible in decommissioning, annealing will need to occur more regularly and the overall lifetime would be significantly shorter in comparison to the general monitoring use or for use detecting β^- radiation.

5.3.3.2 Cooling

Cooling the CCD during operation does not reduce the rate at which damage is produced, however it does reduce the noise produced by the damage, whilst also reducing the dark current inherent to the CCD. The comparison of cooling methods given in Figure 4.30 has been reproduced here in Figure 5.12 for clarity. It can be seen that if the fan is used to cool the heat pipe, a reduction in noise of greater than 97% can occur. Although cooling the CCD directly with the fan was shown to be the most effective setup, this would not be practical in the final device, and it is not significantly better than the configuration using the heat pipe with the fan. Therefore, it is recommended that the heat pipe ought always to be used, and in situations where a fan is suitable this will be used to cool the heat pipe. There are some situations where a fan may not be able to be used, for example if dust is present, as any movement of the dust caused by the fan could be hazardous. In these situations, if the fan is not used, the heat pipe alone is still effective at reducing the noise produced by more than half.

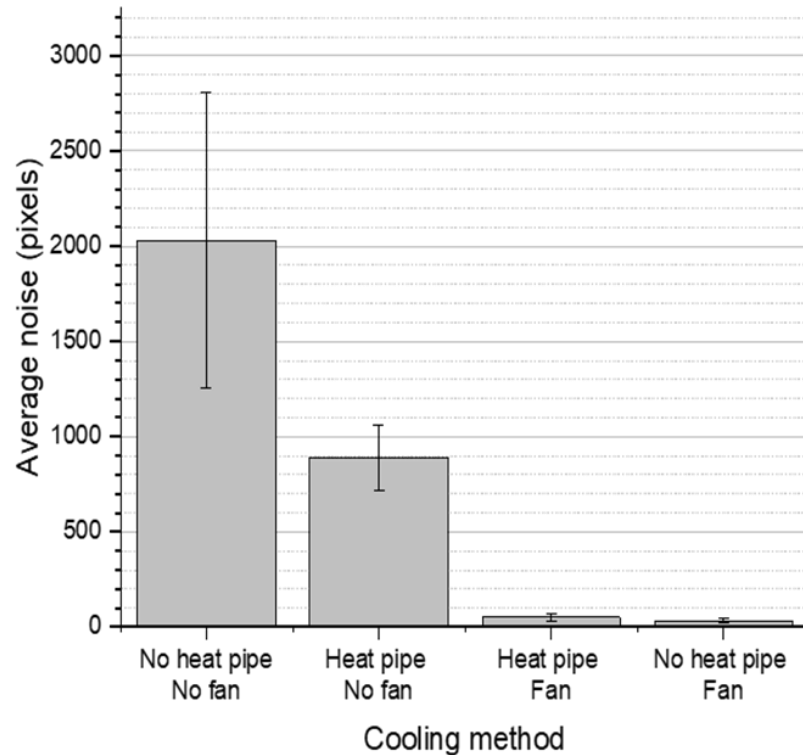


Figure 5.12 Average number of bright pixels (noise) in images produced by the CCD in 5-minute exposures with no source present at four levels of cooling, from warmest to coolest: No cooling, just the heat pipe, both the heat pipe and the fan, and just the fan. Reproduced from Figure 4.30.

The fan and heat pipe used are effective, whilst also being low-cost, small in size, low mass and they can be implemented within the existing device and with the same power supply. More effective methods of cooling could be implemented; however, these would make the device bulkier or require additional power sources. Therefore, the cooling setup used is sufficient at reducing noise without compromising the intended functionality of the device.

Cooling also reduces the time required for the CCD temperature to stabilise as it warms up, meaning measurements can be taken more quickly or for longer without needing additional background images to be taken to account for the increase in dark current with operating temperature.

5.3.3.3 Image processing

Example sections of a ^{210}Po exposure before and after image processing, using a threshold of 100 ADU to remove noise, is shown in Figure 5.13. The gaps in the streaks produced by the α particles have been joined up, and a large portion of the noise has been removed.

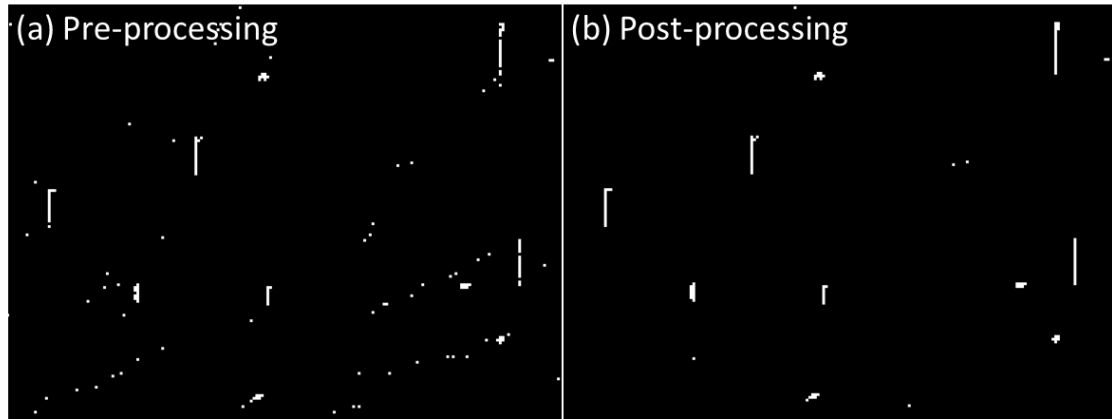


Figure 5.13 Representative 250×150 section of a highlighted CCD image produced under a 30-s exposure to a ^{210}Po source (a) before and (b) after post-processing to remove noise.

Processing images to remove noise using the 100 ADU threshold would also remove less intense clusters produced by β^- particles. As the intensity of clusters produced by β^- radiation is over 70 ADU, the processing can be modified to only remove noise below a 70 ADU threshold if β^- radiation is present. However, this will not be as accurate as the removal of noise in an α -particle exposure, as 25% of the noise clusters will remain. Any further analyses performed will need to be done with this consideration in mind. Therefore, some discretion should be used when using image processing to remove noise, to account for the type of radiation being observed or in an unknown environment where multiple radiation types might be present. The unprocessed images should be reviewed to identify the types of radiation present before the noise is removed.

5.3.3.4 Overall process

The final process for mitigating the effects of the radiation damage is as follows:

1. Cool the CCD during operation to minimise noise produced by damage, with a heat pipe and, if appropriate, a fan.
2. Identify the type of radiation seen in the exposure to determine a noise-removal threshold.
3. Process the images accordingly to remove any unwanted noise.
4. Once the noise has built to a level to be causing analysis difficulties, the CCD can be annealed to repair some of the damage.

This process greatly extends the lifetime of the device and improves the accuracy of both α -particle and β^- -particle detection. However, there will be more limitations on the latter as there will be some remaining noise signals which will be more difficult to distinguish from β^- -particle clusters.

5.4 Comparison with existing technologies

The CCD device studied in this research has shown great potential for use as an *in-situ* detector of a variety of radiation types, with the ability to distinguish between α and β^- radiation, and also providing the potential of detecting neutrons if ^6Li -enriched crystals are used. This improves upon existing technologies used for detecting α radiation such as ionisation chambers, which are described in Section 2.1.5.3. These are effective, readily-available devices for identifying the presence and activity of radiation, but do not provide the ability to discriminate between different types of radiation [17] without modification of the fill gas used, etc.

Other detector types such as proportional counters or scintillators have this capability, but these are typically larger in size and require operation at higher, very stable, voltages; for

α and β^- particles they can have the added constraints of requiring a thin and therefore delicate window as otherwise the detector container is too thick for them to penetrate [17], [18]. Similarly, silicon detectors are commonly used in laboratory α -particle detection and can provide relatively-precise spectroscopic information. However, they are usually not portable and hence are not suitable for *in-situ* use, and the samples have to be prepared and installed under vacuum. In contrast, the CCD is powered directly through the USB cable used to connect the CCD to a computer with the relevant software. This gives it greater portability and flexibility for use as a hand-held detector.

A common problem with α detectors is the proximity required. This problem has not been resolved with the CCD, but its small size and low mass provide more potential flexibility for use in a wider range of environments. The CCDs need to be in near-contact with both α and β^- sources to obtain accurate information, making them less suitable for high-activity environments where it may be dangerous for a user to be in close proximity to any potential radioactive sources. However, it may still be possible to use these devices in these or other hazardous environments by mounting them to robots. Their small size and low power requirements make this feasible. Other detectors are used for detecting α radiation at a distance, but as discussed in Section 2.1.5.4, these usually require high activities and complete darkness to obtain good data [19]–[21]. The CCD is particularly useful at low-activity measurements when considering α radiation and can be used in the light, providing different applications for these different devices.

In situations where quick and accurate detection and spectroscopy of β^- and γ radiation are required, the CCDs are not the most appropriate detector which could be used due to the processing required to obtain spectroscopic information and their insensitivity to γ radiation. However, in situations with α radiation or a mixed field environment where fast identification is required *in-situ*, the CCDs provide an excellent solution at a relatively

low cost which can also provide additional information when the produced images are further analysed.

5.5 References

- [1] B. E. Burke, R. D. Petrasso, C. K. Li, and T. C. Hotaling, “Use of charge-coupled device imagers for charged-particle spectroscopy,” *Rev. Sci. Instrum.*, vol. 68, no. 1 pt 2, pp. 599–602, 1997.
- [2] X. Shou-long, Z. Shu-liang, and H. You-jun, “ γ -ray Detection Using Commercial Off-The-Shelf CMOS and CCD Image Sensors,” *IEEE Sens. J.*, pp. 1–1, 2017.
- [3] A. Aguilar-Arevalo *et al.*, “Measurement of radioactive contamination in the CCD’s of the DAMIC experiment,” *J. Phys. Conf. Ser.*, vol. 718, p. 042057, May 2016.
- [4] M. Bé, V. Chisté, C. Dulieu, V. Chechev, N. Kuzmenko, and M. Galán, “Table of Radionuclides (Vol. 4 – A = 133 to 252),” vol. 5, 2010.
- [5] J. S. Lilley, *Nuclear Physics: Principles and Applications*. John Wiley & Sons, 2001.
- [6] E. L. Crow and K. Shimizu, *Lognormal Distributions: Theory and Applications*. 1988.
- [7] M. J. Tarr, “Visual pattern recognition,” *Am. Psychol. Assoc.*, 1998.
- [8] M.-M. Bé *et al.*, “Table of Radionuclides (Vol. 3 - A = 3 to 244),” vol. 3, 2006.
- [9] E. Savvides, M. Zamani, and S. Charalambous, “An Approach to Fast and Thermal Neutron Spectroscopy Based on ${}^6\text{Li}(n,\alpha){}^3\text{H}$ Reaction,” *Nucl. Tracks Radiat. Meas.*, vol. 15, pp. 495–498, 1988.

- [10] T. Saad Saoud, S. Moindjie, D. Munteanu, and J. L. Autran, “Natural radiation events in CCD imagers at ground level,” *Microelectron. Reliab.*, vol. 64, pp. 68–72, 2016.
- [11] O. Hainaut, “CCD Artifacts,” 1996. [Online]. Available: https://www.eso.org/~ohainaut/ccd/CCD_artifacts.html. [Accessed: 03-Nov-2019].
- [12] J. Estrada, J. Molina, J. J. Blostein, and G. Fernández, “Plasma effect in silicon charge coupled devices (CCDs),” *Nucl. Instruments Methods Phys. Res. Sect. A Accel. Spectrometers, Detect. Assoc. Equip.*, vol. 665, pp. 90–93, 2011.
- [13] T. S. Lomheim *et al.*, “Imaging charge-coupled device (ccd) transient response,” pp. 1876–1885, 1990.
- [14] J. Schott, “Charge coupled devices (CCDs) — A detector system for particles with time resolution and local assignment with particle trajectories,” *Int. J. Radiat. Appl. Instrumentation. Part D. Nucl. Tracks Radiat. Meas.*, vol. 15, no. 1–4, pp. 81–89, Jan. 1988.
- [15] G. R. Hopkinson and A. Mohammadzadeh, “CCD Radiation Testing at Low Temperatures Using a Laboratory Alpha Particle Source,” *IEEE Trans. Nucl. Sci.*, vol. 53, no. 6, pp. 3758–3763, Dec. 2006.
- [16] J. R. Janesick, *Scientific Charge-coupled Devices*. SPIE Press, 2001.
- [17] G. F. Knoll, *Radiation Detection and Measurement*. John Wiley & Sons, 1989.
- [18] J. R. Cooper, K. Randle, and R. S. Sokhi, *Radioactive Releases in the Environment: Impact and Assessment*. John Wiley & Sons, 2003.

- [19] A. J. Crompton, K. A. A. Gamage, A. Jenkins, and C. J. Taylor, “Alpha particle detection using alpha-induced air radioluminescence: A review and future prospects for preliminary radiological characterisation for nuclear facilities decommissioning,” *Sensors (Switzerland)*, vol. 18, no. 4, 2018.
- [20] J. Sand *et al.*, “Imaging of alpha emitters in a field environment,” *Nucl. Instruments Methods Phys. Res. Sect. A Accel. Spectrometers, Detect. Assoc. Equip.*, vol. 782, pp. 13–19, May 2015.
- [21] S. Yamamoto, M. Komori, S. Koyama, and T. Toshito, “Luminescence imaging of water during alpha particle irradiation,” *Nucl. Instruments Methods Phys. Res. Sect. A Accel. Spectrometers, Detect. Assoc. Equip.*, vol. 819, pp. 6–13, May 2016.

6 Conclusion

6 CONCLUSION.....	154
6.1 CCDs for α radiation detection and spectroscopy.....	154
6.2 CCDs for detecting β^- and neutron radiation	155
6.3 Recommendations for future work.....	156
6.4 Final conclusion	156

6.1 CCDs for α radiation detection and spectroscopy

The research described in this thesis has demonstrated that commercially-available charge-coupled devices can be used to identify the presence of α radiation quickly and easily, even in a mixed field of several different types of radiation. A qualitative estimate of the energy can be made on the basis of: the size of the clusters produced; whether any streaks are present; the ratio of streaks to clusters; and the streak lengths. All of this information may later be analysed in more detail to give a more accurate estimate about the energy of the incident α radiation. SRIM simulations indicate that it should be possible to detect α particles with energies between 2.2 and 8.7 MeV with these devices, with incomplete data collection likely at the extremes of these values. This suggests that a broad variety of α radiation sources might be detected.

The CCDs used in this research are small and easily powered, allowing them to be used in a wide variety of situations. Prominent examples include use as a handheld

contamination monitor, in decommissioning, and for use mounted on robots. As each individual α -particle interaction can be identified in the images produced, they are potentially particularly effective for the identification of very low activity contamination, though short exposures can be used to allow for detection of higher activities.

Although α radiation can cause damage to these devices, methods have been found in this research to minimise the effect of this, thus with the potential to extend the lifetime of the device used, hypothetically, on a commercial basis. These methods of cooling, annealing and image processing have all been chosen as a compromise between effectiveness, convenience to the user, and to maintain the approximate cost and small size of the device.

6.2 CCDs for detecting β^- and neutron radiation

The capability of these devices for detecting β^- radiation has also been demonstrated in this work, based on the characteristic shape of the associated trails, also exhibiting some spectroscopic potential based on the sizes of the clusters produced. Further, the CCDs have been shown to be relatively insensitive to γ radiation, allowing clusters from β^- radiation to be identified more confidently. Using a variety of properties such as cluster size, intensity of the brightest pixel in the cluster, and whether streaks are observed or not, has demonstrated the potential for accurate discrimination between β^- and α radiation.

The ability of CCDs to detect α particles and, similarly, tritons has allowed this device to be used for the detection of neutrons with the assistance of ^6Li -enriched crystals. The ^6Li -enriched crystals might be applied as a removable cap, suggesting the potential for

the user to quickly switch between detection modes. This increases the number of potential applications and hence the utility of the device.

The noise produced by the CCD has also been analysed has been observed to possess unique properties to allow for separation of signals of interest and those produced by undesirable noise.

6.3 Recommendations for future work

There are a number of areas where this research would benefit from further investigation and development. The potential of this device for performing spectroscopy of α and β^- radiation has been assessed through simulations in this thesis, but would benefit from further research to determine the extent and accuracy of this potential.

The device itself requires some additional development. Primarily, housing for the device containing the cooling apparatus needs to be designed and implemented. A system for the removable lithium covering also needs to be realised.

Finally, there is scope for improvement in the image processing techniques developed in this research and described in this thesis. These would benefit from a graphical user interface for ease of use, and could be designed to output the relevant graphs directly, in addition to the data which were then analysed separately in this research.

6.4 Final conclusion

In conclusion, commercially-available CCDs have been shown in this research to be capable at detecting α , β^- , and neutron radiation, with α and β^- discrimination being possible in a mixed-radiation environment. This fulfils the requirement of a device to quickly and efficiently detect α contamination in-situ, as a handheld, low-cost device. This fills a gap in the prior art associated with detection technologies which are suitable

for hand-held use but poor at discrimination, or devices which have excellent spectroscopic capabilities but which are best used in a laboratory environment and not suited to *in-situ* deployment.

The devices studied in this research have shown potential for spectroscopy of α and β^- radiation, though further research should be done to determine the full scope and accuracy of this. An estimate of whether the source of α or β^- radiation is high- or low-energy can be made by the user *in-situ* by simply making a judgement based on the shapes of the clusters produced, with more accurate information made possible with image processing. The relative activity of sources can also be readily identified based on the rate at which clusters are produced during the exposures.

Appendix A

APPENDIX A	158
A.1 Fill gaps in streaks.....	158
A.2 Remove noise	159
A.3 Highlight images	161
A.4 Cluster analysis	162
A.5 Streak analysis.....	163
A.6 Intensity analysis	164

This appendix consists of the python™ 3.6 code used for processing the images generated by the CCD.

A.1 Fill gaps in streaks

```

1. """
2. Created on Tue Jun  5 13:18:01 2018
3.
4. @author: Rosie
5.
6. Join_Streaks
7.
8. Take CCD images and fill in any single-pixel gaps in vertical streaks. It
9. identifies a single-pixel gap between three vertically surrounding pixels (2
10. one direction, one the other), and fills the gap in. The gap is assigned the
11. intensity threshold of the CCD software. The edited images are then saved as
12. separate .bmp files with names in the format
13. "[Name input as function argument][Image Number.].bmp".
14.
15. """
16.
17. import matplotlib.image
18. import scipy
19. from scipy import ndimage

```

```

20. import numpy
21. import glob
22.
23. output_name = None
24.
25. def join_streaks(output_name):
26.
27.     # Take the list of bmp image names from the current directory
28.     ImageNames = glob.glob('*.bmp')
29.
30.     # Return a message if no images are identified
31.     if ImageNames == []:
32.         print ('There are no images' )
33.         return None
34.
35.     # Loop through the different .bmp images
36.     for k in range(0, len(ImageNames)):
37.
38.         # Read in the images
39.         imagedata = matplotlib.image.imread(ImageNames[k])
40.         # If 3D, make 2D
41.         if imagedata.ndim == 3:
42.             imagedata = imagedata[:, :, 0]
43.
44.         # Make the data able to be re-written
45.         imagedata.setflags(write=1)
46.
47.         # Calculate the size of the image. Reduce the max row size to account
48.
49.         # for needing to check above and below each pixel
50.         row_max = numpy.shape(imagedata)[0]-3
51.         col_max = numpy.shape(imagedata)[1]-1
52.
53.         # loop over whole image array
54.         for col_num in range (0, col_max):
55.             for row_num in range (2, row_max):
56.                 # If the current pixel is black and at least 2+1 pixels above
57.
58.                 # and below have an intensity greater than 0, make the
59.                 # current pixel white have the intensity of the software
60.                 # threshold
61.                 if (imagedata[row_num, col_num] == 0 and
62.                    imagedata[row_num-1, col_num] > 0 and
63.                    imagedata[row_num+1, col_num] > 0 and
64.                    ( imagedata[row_num-2, col_num] > 0 or
65.                     imagedata[row_num+2, col_num] > 0)):
66.
67.                     # Edit the image data
68.                     imagedata[row_num, col_num] = 49
69.
70.                 # Save each new joined up image with the name specified
71.                 if output_name != None:
72.                     j = k+1
73.                     i = "%.2d" % j
74.                     scipy.misc.imsave('{}{}.bmp'.format(output_name, i), imagedata)
75.
76.             return ImageNames
77.
78. join_streaks(output_name)

```

A.2 Remove noise

```

1. """
2. Created on Wed Jun 20 15:24:31 2018
3.
4. @author: Rosie

```

```

5.
6. Remove clusters from CCD images identified to be noise. A threshold value for
7. determining noise can be input. The edited images are then saved as
8. separate .bmp files with names in the format
9. "[Name input as function argument][Image Number.].bmp".
10.
11. """
12.
13. import matplotlib.image
14. import scipy
15. from scipy import ndimage
16. import numpy
17. from numpy import histogram
18. import glob
19. from skimage.measure import regionprops
20.
21. removed_name = None
22. threshold = None
23.
24. def remove_noise(threshold, removed_name):
25.
26.     # Take the list of bmp image names from the current directory
27.     ImageNames = glob.glob('*.bmp')
28.     # Create a list for storing the number of clusters removed from each image
29.
30.     removed_clusters = []
31.     if ImageNames == []:
32.         print ('There are no images' )
33.         return
34.
35.     # Loop through the different bmp images
36.     for k in range(0, len(ImageNames)):
37.
38.         # Read in the images
39.         imagedata = matplotlib.image.imread(ImageNames[k])
40.         # If 3D, make 2D
41.         if imagedata.ndim == 3:
42.             imagedata = imagedata[:, :, 0]
43.         # Make the data able to be re-written
44.         imagedata.setflags(write=1)
45.
46.         # Identify clusters as any pixels connected horizontally, vertically
47.         # or diagonally
48.         diagonals = scipy.ndimage.generate_binary_structure(2,2)
49.         clusters, n = ndimage.label(imagedata, structure = diagonals)
50.
51.         # Get information about the clusters
52.         cluster_info = regionprops(clusters)
53.
54.         # Initialise a count of the number of clusters removed from this image
55.
56.         removed_count = 0;
57.
58.         # Iterate through the clusters
59.         for i in range(1, len(cluster_info)):
60.             # Identify the coordinates of the pixels in the cluster
61.             coords = cluster_info[i].coords
62.
63.             # Set the noise flag to be true
64.             noise = True
65.
66.             # Iterate through each of the pixels in the cluster
67.             for i in range(0, len(coords)):
68.                 # Find the pixel intensity
69.                 value = imagedata[coords[i,0], coords[i,1]]
70.                 # If the pixel is above the chosen threshold, set the noise

```

```

70.         # flag to false. This identifies this cluster as not being
71.         # noise and will keep all pixels in the cluster
72.         if value > threshold:
73.             noise = False
74.
75.         # If the cluster is identified as noise, remove it
76.         if noise == True:
77.
78.             for i in range(0, len(coords)):
79.                 imagedata[coords[i,0], coords[i,1]] = 0
80.
81.             # Increment the count for removed clusters
82.             removed_count += 1
83.
84.         # Add the total count of removed clusters for this image to the list
85.
86.         removed_clusters.append(removed_count)
87.
88.         # Save the new data with the name
89.         if removed_name != None:
90.             m = k+1
91.             n = "%.2d" % m
92.             scipy.misc.imsave('{}{}.bmp'.format(removed_name, n), imagedata)
93.
94.         # Return a list of the number of clusters removed in each image
95.         return removed_clusters
96. remove_noise(threshold, removed_name)

```

A.3 Highlight images

```

1.  """
2.  Created on Wed Jun 20 15:24:31 2018
3.
4.  @author: Rosie
5.
6.  Highlight all clusters to have the maximum intensity of 255. The edited images
7.
8.  are then saved as separate .bmp files with names in the format
9.  "[Name input as function argument][Image Number.].bmp"
10. """
11. import matplotlib.image
12. import scipy
13. from scipy import ndimage
14. import numpy
15. from numpy import histogram
16. import glob
17. from skimage.measure import regionprops
18.
19. highlight_name = None
20.
21. def highlight(highlight_name):
22.
23.     # Take the list of bmp image names from the current directory
24.     ImageNames = glob.glob('*.bmp')
25.
26.     if ImageNames == []:
27.         print ('There are no images' )
28.         return
29.
30.     # Loop through the different bmp images
31.     for k in range(0, len(ImageNames)):
32.
33.         # Read in the images
34.         imagedata = matplotlib.image.imread(ImageNames[k])

```

```

35.     # If 3D, make 2D
36.     if imagedata.ndim == 3:
37.         imagedata = imagedata[:, :, 0]
38.     # Count the number of connected clusters
39.     imagedata.setflags(write=1)
40.
41.     # Work out the dimensions of the image
42.     dim = numpy.shape(imagedata)
43.
44.     # For each pixel, check if a pixel has a value. If so, set to max valu
e
45.     for p in range(0, dim[0]):
46.         for q in range(0, dim[1]):
47.             if imagedata[p, q] > 0:
48.                 imagedata[p, q] = 255
49.
50.     # Save a new file for each of the highlighted images
51.     if highlight_name != None:
52.         j = k+1
53.         l = "%.2d" % j
54.         scipy.misc.imsave('{}{}.bmp'.format(highlight_name, l), imagedata)
55.
56.     return
57.
58. highlight(highlight_name)

```

A.4 Cluster analysis

```

1.  """
2.  Created on Thu May 31 10:26:45 2018
3.  Rosie Newton
4.
5.  Count the total number of clusters in the CCD images, and create histogram dat
a for
6.  the sizes of the clusters.
7.
8.  """
9.  import matplotlib.image
10. import scipy
11. from scipy import ndimage
12. import numpy
13. from numpy import histogram
14. import glob
15. from skimage.measure import regionprops
16. from scipy.ndimage import morphology
17.
18.
19. def cluster_count():
20.
21.     total_clusters = []
22.     cluster_values = []
23.
24.     # Take the list of bmp image names from the current directory
25.     ImageNames = glob.glob('*.bmp')
26.
27.     if ImageNames == []:
28.         print ('There are no images' )
29.         return None, None, None
30.
31.     # Loop through the different bmp images
32.     for k in range(0, len(ImageNames)):
33.
34.         # Read in the images
35.         imagedata = matplotlib.image.imread(ImageNames[k])
36.         # If 3D, make 2D

```

```

37.     if imagedata.ndim == 3:
38.         imagedata = imagedata[:, :, 0]
39.         # Prepare to count clusters including those connected diagonally
40.         diagonals = scipy.ndimage.morphology.generate_binary_structure(2,2)
41.         # Count the number of connected clusters
42.         clusters, n = ndimage.label(imagedata, structure = diagonals)
43.
44.         # Work out the size of each cluster
45.         cluster_size, num = histogram(clusters[:, n])
46.         # Change the array to a list (so pop can be used)
47.         cluster_size = list(cluster_size)
48.         # Remove the first value (number of black pixels)
49.         cluster_size.pop(0)
50.
51.         if len(cluster_size) > 0:
52.             # Prepare bins to have integer values up to the largest cluster size
53.
54.             bins = list(range(0, max(cluster_size)+1))
55.             # Get the data for the histogram
56.             num_clusters, binnumber = histogram(cluster_size, bins)
57.         else:
58.             num_clusters = 0
59.
60.         # Add the value to the array of cluster sizes
61.         total_clusters.append(n)
62.         cluster_values.append(num_clusters)
63.
64.     return total_clusters, cluster_values, ImageNames
65.
66. cluster_count()

```

A.5 Streak analysis

```

1. """
2. Created on Fri Jun 1 11:16:47 2018
3. @author: Rosie
4.
5. Streak analysis
6.
7. Analyses a group of bmp images to work out the connected pixel clusters, count
8. them and count their lengths. Use this info to create histogram of the lengths
9.
10. Note: For the bounding box:
11.     0: min_row
12.     1: min_col
13.     2: max_row
14.     3: max_col
15.
16. """
17.
18. import matplotlib.image
19. import scipy
20. from scipy import ndimage
21. import numpy
22. from numpy import histogram
23. import glob
24. from skimage.measure import regionprops
25.
26.
27. def streak_analysis():
28.
29.     total_heights = []
30.     heights_hist = []

```

```

31.
32.     # Take the list of .bmp image names from the current directory
33.     ImageNames = glob.glob('*.bmp')
34.
35.     if ImageNames == []:
36.         print ('There are no images' )
37.         return
38.
39.     # Loop through the different .bmp images
40.     for k in range(0, len(ImageNames)):
41.
42.         # Read in the images
43.         imagedata = matplotlib.image.imread(ImageNames[k])
44.         # If 3D, make 2D
45.         if imagedata.ndim == 3:
46.             imagedata = imagedata[:, :, 0]
47.         # Prepare to count clusters including those connected diagonally
48.         diagonals = scipy.ndimage.morphology.generate_binary_structure(2,2)
49.         # Count the number of connected clusters
50.         clusters, n = ndimage.label(imagedata, structure = diagonals)
51.
52.         # Get properties of the clusters
53.         cluster_info = regionprops(clusters)
54.
55.         # Re-initialise the height array for each image
56.         height = []
57.
58.         # Cycle through each cluster, and calculate the length
59.         for j in range(0, len(cluster_info)):
60.             # Add the length to the array for each image
61.             height.append(cluster_info[j].bbox[2]-cluster_info[j].bbox[0])
62.             # Add length to the list for all images
63.             total_heights.append(cluster_info[j].bbox[2]-
cluster_info[j].bbox[0])
64.
65.         # Create a histogram for the heights from each image
66.         h_bins = list(range(0, max(height)+1))
67.         num_heights, height_bins = histogram(height, h_bins)
68.         # Add these to an array to store all the histogram data
69.         heights_hist.append(num_heights)
70.
71.     # Create a histogram for the summed height data
72.     total_bins = list(range(0, max(total_heights)+1))
73.     num_total_heights, total_heights_bins = histogram(total_heights, bins)
74.
75.     # Return the height histogram, the summed histogram
76.     return heights_hist, num_total_heights, ImageNames

```

A.6 Intensity analysis

```

1.  """
2.  Created on Wed Sep 12 09:51:33 2018
3.
4.  @author: Rosie
5.
6.  Collect the values of the pixels with the highest intensity in each pixel
7.  cluster and output the data as histograms for each individual image and all of
8.  them summed
9.  """
10.
11. import matplotlib.image
12. import scipy
13. from scipy import ndimage
14. import numpy
15. from numpy import histogram

```

```

16. import glob
17. from skimage.measure import regionprops
18.
19. def intensities():
20.
21.     # Initialiase some arrays for the histograms later
22.
23.     total_max = []
24.     max_hist = []
25.
26.     # Take the list of bmp image names from the current directory
27.     ImageNames = glob.glob('*.bmp')
28.
29.     if ImageNames == []:
30.         print ('There are no images' )
31.         return
32.
33.     # Loop through the different bmp images
34.     for k in range(0, len(ImageNames)):
35.
36.         # Read in the images
37.         imagedata = matplotlib.image.imread(ImageNames[k])
38.         # If 3D, make 2D
39.         if imagedata.ndim == 3:
40.             imagedata = imagedata[:, :, 0]
41.
42.         # Prepare to count clusters including those connected diagonally
43.         diagonals = scipy.ndimage.morphology.generate_binary_structure(2,2)
44.         # Count the number of connected clusters
45.         clusters, n = ndimage.label(imagedata, structure = diagonals)
46.
47.         if n == 0:
48.             print (ImageNames[k] + ' has no clusters' )
49.         if n == 1:
50.             print (ImageNames[k] + ' has one cluster' )
51.
52.         # Get properties of the clusters
53.         cluster_info = regionprops(clusters, intensity_image=imagedata)
54.
55.         # Initialise the array of max values for each image
56.         max_ints = []
57.
58.         # Cycle through each cluster
59.         for j in range(0, len(cluster_info)):
60.
61.             # Get the maximum intensity for the cluster
62.             max_int = cluster_info[j].max_intensity
63.
64.             # Add the highest intesity for every cluster to a temporary array
65.
66.             # for this image
67.             max_ints.append(max_int)
68.
69.             # Add the highest intensity for every cluster to an array for
70.             # all the images
71.             total_max.append(max_int)
72.
73.             # Create a histogram for the max intensities from each image
74.             # Add these to an array to store all the histogram data
75.             h_bins = list(range(0, max(max_ints)+1))
76.             num_max, max_bins = histogram(max_ints, h_bins)
77.             max_hist.append(num_max)
78.
79.             # Create a histogram for the summed intensity data
80.             total_bins = list(range(0, max(total_max)+1))
81.             num_total_max, total_max_bins = histogram(total_max, total_bins)
82.
83.             # Return the data for the histograms for each image and the total data

```

```
83.     return max_hist, num_total_max
```